ISSN 1997-308X (Print), 2412-8767 (Online)

IZVESTIYA VUZOV POROSHKOVAYA METALLURGIYA I FUNKTSIONAL'NYE POKRYTIYA

POWDER METALLURGY AND FUNCTIONAL COATINGS

Scientific and Technical Journal
Founded in 2007
4 numbers per year

Vol. 16 - № 3 - 2022

Journal is included into the list of the scientific journals recommended by the Highest Attestation Commission of the Ministry of Education and Science of the Russian Federation for publishing the results of doctoral and candidate dissertations.

Abstracting/Indexing: Scopus, RSCI (Russian Science Citation Index) to Web of Science platform, Ulrich's Periodicals Directory, VINITI Database (Abstract Journal).

Founder

National University of Science and Technology «MISIS»

Address: NUST «MISIS», Leninskiy pr. 4, Moscow, 119049 Russia

Internet address: http://www.misis.ru

Publisher

LLC «Kalvis»

Actual address: off. 405, Leninskiy pr. 4g, Moscow, 119049 Russia

Address for correspondence: p/o box 28, LLC «Kalvis», Moscow, 119049 Russia

Internet address: http://www.kalvis.ru

Editorial Staff

Editorial office address: off. 203, NUST «MISIS», Leninskiy pr. 4g, Moscow, 119049 Russia

Address for correspondence: «Izvestiya vuzov. Poroshkovaya metallurgiya i funktsional'nye pokrytiya» (box 164), NUST «MISIS», Leninskiy pr., 4, Moscow, 119049 Russia

Phone: (495) 638-45-35

E-mail: izv.vuz@misis.ru

Internet address: http://powder.misis.ru

Leading editor: Sosnina O.V.

Executive editor: Kudinova A.A.

Layout designer: Legkaya E.A.

Subscription

Ural-Press Agency

Online version: http://powder.misis.ru
http:// www.kalvis.ru

Format 60×88 1/8. Quires 11

Signed print 13.09.2022

Certificate of registration No. FS77-27955 (12.04.2007)

Re-registration PI No. FS77-79230 (25.09.2020)

ISSN 1997-308X (Print), 2412-8767 (Online)

ИЗВЕСТИЯ ВУЗОВ ПОРОШКОВАЯ МЕТАЛЛУРГИЯ И ФУНКЦИОНАЛЬНЫЕ ПОКРЫТИЯ

POWDER METALLURGY AND FUNCTIONAL COATINGS

Научно-технический журнал
Основан в 2007 г. Выходит 4 раза в год

Том 16 - № 3 - 2022

Журнал включен в перечень научных журналов, рекомендованных ВАК Минобрнауки РФ для публикации результатов диссертаций на соискание ученых степеней.

Журнал индексируется в международной базе данных Scopus, Russian Science Citation Index (RSCI) на платформе Web of Science, Ulrich's Periodicals Directory, РИНЦ, а также входит в базу данных (реферативный журнал) ВИНИТИ.

Учредитель

ФГАОУ ВО «Национальный исследовательский технологический университет "МИСиС"»

Адрес: 119049, Москва, Ленинский пр-т, 4
http://www.misis.ru

Издатель

ООО «Калвис»

Фактический адрес: 119049, Москва, Ленинский пр-т, 4 (корп. 4г, оф. 405)

Почтовый адрес: 119049, Москва, а/я 28 для ООО «Калвис»
http://www.kalvis.ru

Редакция журнала

Фактический адрес: 119049, Москва, В-49, Ленинский пр-т, 4, НИТУ «МИСиС» (корп. 4г, оф. 203)

Почтовый адрес: 119049, Москва, В-49, Ленинский пр-т, 4, НИТУ «МИСиС», редакция журнала «Известия вузов. Порошковая металлургия и функциональные покрытия» (яч. 164)

Тел.: (495) 638-45-35

E-mail: izv.vuz@misis.ru

Интернет: http://powder.misis.ru

Ведущий редактор: Соснина О.В.

Выпускающий редактор: Кудинова А.А.

Дизайн и верстка: Легкая Е.А.

Подписка

Агентство «Урал-пресс»

Электронные версии отдельных статей или журнала в целом доступны на сайтах: http://powder.misis.ru
http:// www.kalvis.ru

Формат 60×88 1/8. Печ. л. 11

Подписано в печать 13.09.2022 г.

Свидетельство о регистрации № ФС77-27955 от 12.04.2007 г.

Перерегистрация 25.09.2020 г. ПИ № ФС77-79230

Contents

Self-Propagating High-Temperature Synthesis

Refractory, Ceramic and Composite Materials

Materials and Coatings Fabricated Using the Additive Manufacturing Technologies

Application of Powder Materials and Functional Coatings

Содержание

Самораспространяющийся высокотемпературный синтез

Тугоплавкие, керамические и композиционные материалы

Материалы и покрытия, получаемые методами аддитивных технологий

Применение порошковых материалов и функциональных покрытий

UDC 669.245.018.44 : 091.3-977
DOI dx.doi.org/10.17073/1997-308X-2022-3-4-23

Oxidation kinetics and mechanism of nickel alloys

© 2022 г. **M.I. Aheiev, V.V. Sanin, N.V. Shvindina, Yu.Yu. Kaplanskii, E.A. Levashov**

National University of Science and Technology (NUST) «MISIS», Moscow, Russia

Received 16.03.2022, revised 21.03.2022, accepted for publication 01.04.2022

Abstract: The study covers the effect of alloying elements on the kinetics and mechanism of oxidation at 1150 °C for 30 hours of heat-resistant nickel alloys obtained using such technologies as centrifugal SHS metallurgy (SHS(M)), vacuum induction melting (VIM), elemental synthesis (ES), hot isostatic pressing (HIP). A comparative analysis was carried out for alloys based on nickel monoaluminide and standard AZhK and EP741NP alloys. It was found that kinetic dependences are described mainly by parabolic approximation. The logarithmic law of oxidation with the rapid (within 3–4 hours) formation of the primary protective layer is typical for alloys doped with molybdenum and hafnium. In the case of AZhK and EP741NP, oxidation proceeds according to a parabolic law at the initial stage (2–3 hours), and then according to a linear mechanism with the voloxidation and complete destruction of samples. Oxygen and nitrogen diffusion proceeds predominantly along the nickel aluminide grain boundaries and it is limited by the Al_2O_3 + Cr_2O_3 + X_nO_m protective film formation. SHS(M) alloys feature by a positive effect of zirconium and tantalum added as dopants on heat resistance. The Ta_2O_5 phase is formed in the intergranular space, which reduces the rate and depth of oxidation. The zirconium-containing top layer Al_2O_3 + $Zr_5Al_3O_{0.5}$ blocks the external diffusion of oxygen and nitrogen, thereby improving heat resistance. Doping with hafnium also has a positive effect on oxidation resistance and leads to the formation of submicron and nanosized HfO_2 inclusions that suppress the grain boundary diffusion of oxygen. MoO_3, Mo_3O_4, $CoMoO_4$ volatile oxides are formed in alloys with a high content of molybdenum and compromise the protective layer integrity. A comparative analysis of the oxidation kinetics and mechanism for samples consisting of the base β-alloy with Cr + Co + Hf additives showed a significant effect on the heat resistance of the sample preparation method. As the proportion of impurity nitrogen decreases and the Cr_2O_3 sublayer is formed, the oxidation mechanism also changes.

Keywords: nickel alloys, heat resistance, oxidized layer, centrifugal SHS metallurgy, elemental synthesis.

Aheiev M.I. – Junior research scientist, Scientific-Educational Center of SHS, National University of Science and Technology (NUST) «MISIS» (119049, Russia, Moscow, Leninskiy pr., 4).
E-mail: aheievmi@gmail.com.

Sanin V.V. – Cand. Sci. (Eng.), Junior research scientist, Scientific-Educational Center of SHS, MISIS–ISMAN.
E-mail: sanin@misis.ru.

Shvindina N.V. – Scientific project engineer 1st category, Scientific-Educational Center of SHS, MISIS–ISMAN.
E-mail: natali19-03@list.ru.

Kaplanskii Yu.Yu. – Cand. Sci. (Eng.), Research scientist, Scientific-Educational Center of SHS, MISIS–ISMAN.
E-mail: ykaplanscky@mail.ru.

Levashov E.A. – Dr. Sci. (Eng.), Prof., Acad. of Russian Academy of Natural Science, Head of Scientific-Educational Center of SHS, MISIS–ISMAN; Head of the Department of powder metallurgy and functional coating, NUST «MISIS».
E-mail: levashov@shs.misis.ru.

For citation: *Aheiev M.I., Sanin V.V., Shvindina N.V., Kaplanskii Yu.Yu., Levashov E.A.* Oxidation kinetics and mechanism of nickel alloys. *Izvestiya Vuzov. Poroshkovaya Metallurgiya i Funktsional'nye Pokrytiya (Powder Metallurgy and Functional Coatings)*. 2022. Vol. 16. No. 3. P. 4–23 (In Russ.). DOI: dx.doi.org/10.17073/1997-308X-2022-3-4-23.

Кинетика и механизм окисления никелевых сплавов

М.И. Агеев, В.В. Санин, Н.В. Швындина, Ю.Ю. Капланский, Е.А. Левашов

Национальный исследовательский технологический университет (НИТУ) «МИСиС», г. Москва, Россия

Статья поступила в редакцию 16.03.2022 г., доработана 21.03.2022 г., подписана в печать 01.04.2022 г.

Аннотация: Исследовано влияние легирующих элементов на кинетику и механизм окисления при температуре 1150 °С в течение 30 ч жаропрочных никелевых сплавов, полученных по технологиям центробежной СВС-металлургии (СВС-М),

вакуумного индукционного переплава (ВИП), элементного синтеза (ЭС) и горячего изостатического прессования (ГИП). Проведен сравнительный анализ сплавов на основе моноалюминида никеля и стандартных сплавов марок АЖК и ЭП741НП. Выявлено, что кинетические зависимости описываются преимущественно параболической аппроксимацией. Логарифмический закон окисления с быстрым (в течение 3–4 ч) формированием первичного защитного слоя характерен для сплавов, легированных молибденом и гафнием. В случае АЖК и ЭП741НП на начальной стадии (2–3 ч) окисление происходит по параболическому закону, а в дальнейшем – по линейному механизму с объемным окислением и полным разрушением образцов. Диффузия кислорода и азота протекает преимущественно по границам зерен алюминида никеля и лимитируется образованием защитной пленки состава $Al_2O_3 + Cr_2O_3 + X_nO_m$. Для сплавов, полученных методом СВС-М, характерным является положительное влияние на жаростойкость легирующих добавок циркония и тантала. В межзеренном пространстве образуется фаза Ta_2O_5, которая снижает скорость и глубину окисления. Цирконийсодержащий верхний слой $Al_2O_3 + Zr_5Al_3O_{0,5}$ блокирует внешнюю диффузию кислорода и азота, тем самым повышая жаростойкость. Легирование гафнием также положительно сказывается на окислительной стойкости сплавов и приводит к образованию субмикронных и наноразмерных включений HfO_2, которые подавляют зернограничную диффузию кислорода. В образцах с повышенным содержанием молибдена формируются летучие оксиды MoO_3, Mo_3O_4, $CoMoO_4$, которые разрушают целостность защитного слоя. Сравнительный анализ кинетики и механизма окисления образцов из базового β-сплава с добавками Cr + Co + Hf показал существенное влияние на жаростойкость способа получения образцов. При снижении доли примесного азота и образования подслоя Cr_2O_3 меняется и механизм окисления.

Ключевые слова: никелевые сплавы, жаростойкость, окисленный слой, центробежная СВС-металлургия, элементный синтез.

Агеев М.И. – мл. науч. сотрудник Научно-учебного центра (НУЦ) СВС, МИСиС–ИСМАН, НИТУ «МИСиС» (119049, г. Москва, Ленинский пр-т, 4). E-mail: aheievmi@gmail.com.

Санин В.В. – канд. техн. наук, мл. науч. сотрудник НУЦ СВС, МИСиС–ИСМАН. E-mail: sanin@misis.ru.

Швындина Н.В. – инженер научного проекта 1-й категории, НУЦ СВС, МИСиС–ИСМАН. E-mail: natali19-03@list.ru.

Капланский Ю.Ю. – канд. техн. наук, науч. сотрудник НУЦ СВС, МИСиС–ИСМАН. E-mail: ykaplanscky@mail.ru.

Левашов Е.А. – докт. техн. наук, акад. РАЕН, проф., директор НУЦ СВС, МИСиС–ИСМАН; зав. кафедрой порошковой металлургии и функциональных покрытий, НИТУ «МИСиС». E-mail: levashov@shs.misis.ru.

Для цитирования: *Агеев М.И., Санин В.В., Швындина Н.В., Капланский Ю.Ю., Левашов Е.А.* Кинетика и механизм окисления никелевых сплавов. *Известия вузов. Порошковая металлургия и функциональные покрытия.* 2022. Т. 16. No. 3. С. 4–23. DOI: dx.doi.org/10.17073/1997-308X-2022-3-4-23.

Introduction

Alloys based on monoaluminide nickel are promising for using in components of gas-turbine engines. At the same time, they have low strength properties at room temperature, resulting in the high risk of fracture and insufficient processability due to difficult machining [1—5]. Plasticizing additives of chromium, molybdenum, and rare-earth elements are introduced into such materials, in order to increase fracture toughness [3—7]. In the case of hot-path alloys the key parameter is oxidation resistance at increased temperatures, fatigue and thermo-cycle impacts, as well as the degree of alloying and the surface state determine their heat resistance [8]. High-temperature oxidation as a type of chemical corrosion leads to an emergence of additional stress concentrators and reduction of mechanical properties due to softening of grain interfaces [8—14].

A comparison of thermodynamic calculations and experimental data regarding the oxidation process for coarse-grained nickel monoaluminide alloyed with chromium and molybdenum showed that oxides Cr_2O_3 and Al_2O_3 form a protective layer at the interfaces preventing oxygen diffusion. Molybdenum promotes formation of volatile suboxides which leave pores in the sample upon evaporation [15]. The formation of oxidized layers near the surface is selective in nature and depends on the composition of introduction elements in the β-phase, the temperature, and the oxidation environment [16].

Hierarchically structured β-alloys doped with chromium, cobalt and other elements with high heat resistance and creep resistance are known. Studies [17—25] show the possibility of obtaining spherical powders for

selective laser melting (SLM) by two process flowcharts: (1) centrifugal SHS casting (SHS-M), vacuum induction remelting (VIR), and plasma rotating electrode process; (2) elementary synthesis of powders (ES) and their plasma spheroidization. Authors [26] investigated the effect of an alloying element (X) on the resistance to elastic, plastic deformation and the creep activation energy (Q). Alloying enabled modification of the structure near the grain boundaries and binding of introduction elements in additional compounds. For example: molybdenum provided an increase in strength, thermal stability, creep resistance and resistance to sulfide corrosion. Zirconium reduced the size of structural components and increased the heat resistance. Introduction of tantalum marked an increase in creep resistance and fatigue strength of the alloy. Micro additions of rhenium during combined alloying with molybdenum in combination with heat treatment significantly increased the yield strength (σ_{ys}), ultimate compressive strength (σ_{ucs}) and the degree of plastic deformation (ε) [26]. Moreover, introduction of up to 15 % Mo and 1.5 % Re by the set of properties provided the greatest increase in mechanical properties of cast alloys [26].

When inheriting a 3-level structure of β-alloy doped with chromium, cobalt and hafnium, the evolution of its structure at all stages of production was noted: ES, hot isostatic pressing (HIP), SLM, SLM + HIP + heat treatment (HT) [27]. Precipitation tests of alloys in the temperature range of 600—1100 °C confirmed the necessity of after-treatment (HIP and HT) [27]. The simultaneous release of strengthening nanoparticles of the Laves phase (Cr_2Nb, Co_2Nb), Heusler phase (Ni_2AlHf) and carbides (Hf_xNb_y)C noticeably improved the mechanical properties of the alloy with niobium and hafnium. Alloying with chromium, cobalt and hafnium in the SLM + HIP +HT state at room temperature enabled the following level of properties to be obtained: σ_{ucs} = 2850 MPa, σ_{ys} = 1170 MPa, ε = 16 %, and at t = 900 °C — σ_{ucs} = 378 MPa, σ_{ys} = 300 MPa, Q = 380 kJ/mol. The alloy with 0.9 % Hf surpassed the alloy with Cr, Co and 0.25 % Hf in terms of high-temperature strength and creep resistance at t = 900 °C: σ_{ucs} = 640 MPa, σ_{ys} = 495 MPa, Q = 775 kJ/mol. It possessed close values of σ_{ucs} = 2720 MPa, σ_{ys} = 1220 MPa, and ε = 12 % at room temperature [27].

At the same time the question of the influence of the composition and method of production of nickel alloys on the oxidation resistance at high temperatures remains open. Therefore, the objective of the study was to compare the kinetics and mechanism of oxidation at t = = 1150 °C for 30 h of nickel β-alloys, AZhK, EP741NP in the SHS-M, VIR, ES, HIP and HT states.

Research materials and methods

In order to study heat resistance, samples were manufactured according to two process flowcharts (see the table): (1) centrifugal SHS casting by the method [18—20, 26], vacuum-induction remelting; (2) elementary synthesis of powder + hot isostatic pressing [28].

A well-known alloy [18, 25] with additions of chromium, cobalt and element (X) according to the table was chosen as the basis. For the base alloy represented by samples *8*, *9* and *12*, the dependences of heat resistance on the method of their production were plotted. The SHS-M alloys produced by centrifugal SHS casting were ingots with a diameter of 80 mm and height of 25—30 mm. They were obtained at an optimum centrifugal acceleration of $a = 150 \pm 5$ m/s^2 [26]. The features of synthesis are described in detail in [17, 18].

The ES method in the layer-by-layer burning mode was used to obtain sintered masses of 5 compositions (see the table). They were ground to a fraction of not less than 100 μm, after which the powder was consolidated by HIP on a gasostat HIRP10/26-200 (ABRA AG, Switzerland) according to [27]. The ES + HIP method is described in [22—25].

Samples 8 mm in diameter and 4 mm high were cut on an EDM machine GX-320L (CHMER EDM, China) and ground to a roughness of R_z = 5. Oxidative annealing was carried out in air at 1150 °C for 30 h with periodic weighing of the samples. The change in their mass, reduced to a unit surface area, over a certain period of time was evaluated. Based on the experimental data, oxidation curves were plotted and approximation equations were derived.

The phase composition of oxidation products was determined using X-ray diffraction phase analysis (XRD) on a diffractometer D2 PHASER (Bruker AXS GmbH, Germany) using CuK_α-radiation in the range of angles of $2\theta = 10° \div 140°$.

The surface morphology and the interface of oxidized samples were studied using a scanning electron

Content of alloying elements (X) and approximation equations for the oxidation function of the investigated β alloys

Содержание легирующих элементов (X) и уравнения аппроксимации функции окисления исследуемых β-сплавов

Sample No.	Method of production	Alloy element (X)	X, % wt./at.		Oxidation equation
1	SHS-M	La	La	0.0831 / 0.03	$y = -0.0502x^2 + 3.1978x + 2.6451$
2		Mo	Mo	2.44 / 1.18	$y = -0.0538x^2 + 3.2244x + 4.2907$
3		Zr	Zr	0.48 / 0.24	$y = -0.0204x^2 + 1.2605x + 1.7022$
4		Ta	Ta	2.11 / 1.07	$y = -0.028x^2 + 1.8015x + 2.9724$
5		Re	Re	1.48 / 0.75	$y = -0.0469x^2 + 2.7109x + 4.0148$
6		Mo	Mo	15.20 / 7.84	$y = 21.4\ln(x) + 31.7$
7		Mo, Re	Mo	15.40 / 8.0	$y = 11.5\ln(x) + 41.7$
			Re	1.40 / 0.40	
8		Hf	Hf	0.98 / 0.25	$y = -0.048x^2 + 3.0074x + 4.213$
9	SHS-M + VIR	Hf	Hf	0.97 / 0.25	$y = 4.87\ln(x) + 3.78$
10	ES + HIP	Nb, Hf	Nb	2.01 / 1.00	$y = 8.89\ln(x) + 9.24$
			Hf	3.47 / 0.90	
11		Mo, Nb, Hf	Mo	4.06 / 2.00	$y = 8.27\ln(x) + 11.11$
			Nb	1.96 / 1.00	
			Hf	3.39 / 0.90	
12		Hf	Hf	0.96 / 0.22	$y = 5.33\ln(x) + 4.75$
13		Mo, Nb, Hf	Mo	7.93 / 4.00	$y = -0.2621x^2 + 16.896x + 29.971$
			Nb	1.92 / 1.00	
			Hf	3.32 / 0.90	
14		Mo, Nb, Hf	Mo	11.64 / 6.00	$y = -0.6548x^2 + 44.62x + 17.681$
			Nb	1.88 / 1.00	
			Hf	3.25 / 0.90	
15	HIP + HT	EP741NP			$y = -2.7111x^2 + 92.107x - 30.405$ $y = 29.95x + 234.17$
16		AZhK			$y = 8.2829x^2 - 12.77x + 13.403$ $y = 34.27x + 31.89$

microscope (SEM) S-3400N (Hitachi, Japan) with an energy dispersive spectrometer NORAN System 7 *X*-ray Microanalysis System (ThermoScientific, USA), and also on a transmission electron microscope (HRTEM) JEM-2100 (Jeol, Japan) using a Gatan 650 Single Tilt Rotation Analytical Specimen Holder (Gatan, Inc., USA). Samples (lamellae) were produced from pre-prepared foils using the focused ion beam (FIB) method on a Quanta 200 3D FIB instrument (FEI Company, USA). HRTEM foils were obtained by ion etching on the PIPS II System instrument (Gatan Inc., USA).

Results and discussion

Analysis of kinetic curves and the composition of oxidation products described the influence of alloying additives on the solubility of oxygen, the course of polymorphic transformations and the formation of volatile

suboxides. In contrast to simple metals, the interfaces of oxidized multicomponent intermetallic alloys are more complex. This is due to different chemical affinity to oxygen of alloying elements, the formation of multiple oxide phases and solid solutions, as well as different mobility of atoms in the oxide phase and the alloy.

Figure 1 shows the oxidation curves of the samples studied, and the above table provides their corresponding equations of approximation. The character of the curves corresponds to the parabolic law of oxidation for samples *1—5*, *8*, *13—14*; to the logarithmic law for samples *6*, *7*, *9—12*; and to the mixed law for samples *15*, *16*. In the latter case, at the initial stage (3—4 h) a parabolic dependence was observed, and after violation of the sample integrity (Figure 2) the oxidation nature obeys a linear law and is controlled by the rate of the chemical reaction.

For samples *1—5*, *8*, *13* and *14*, the highest oxidation rate is observed during the first 7—10 h. After the formation of a protective oxide layer, its values decrease and approach zero. Thus, the controlling oxidation process in this case is diffusion in a solid phase.

The oxidation process of samples *6* and *7* differs substantially from the others and is characterized by the action of additional factors associated presumably with the destruction of the external oxide layer due to

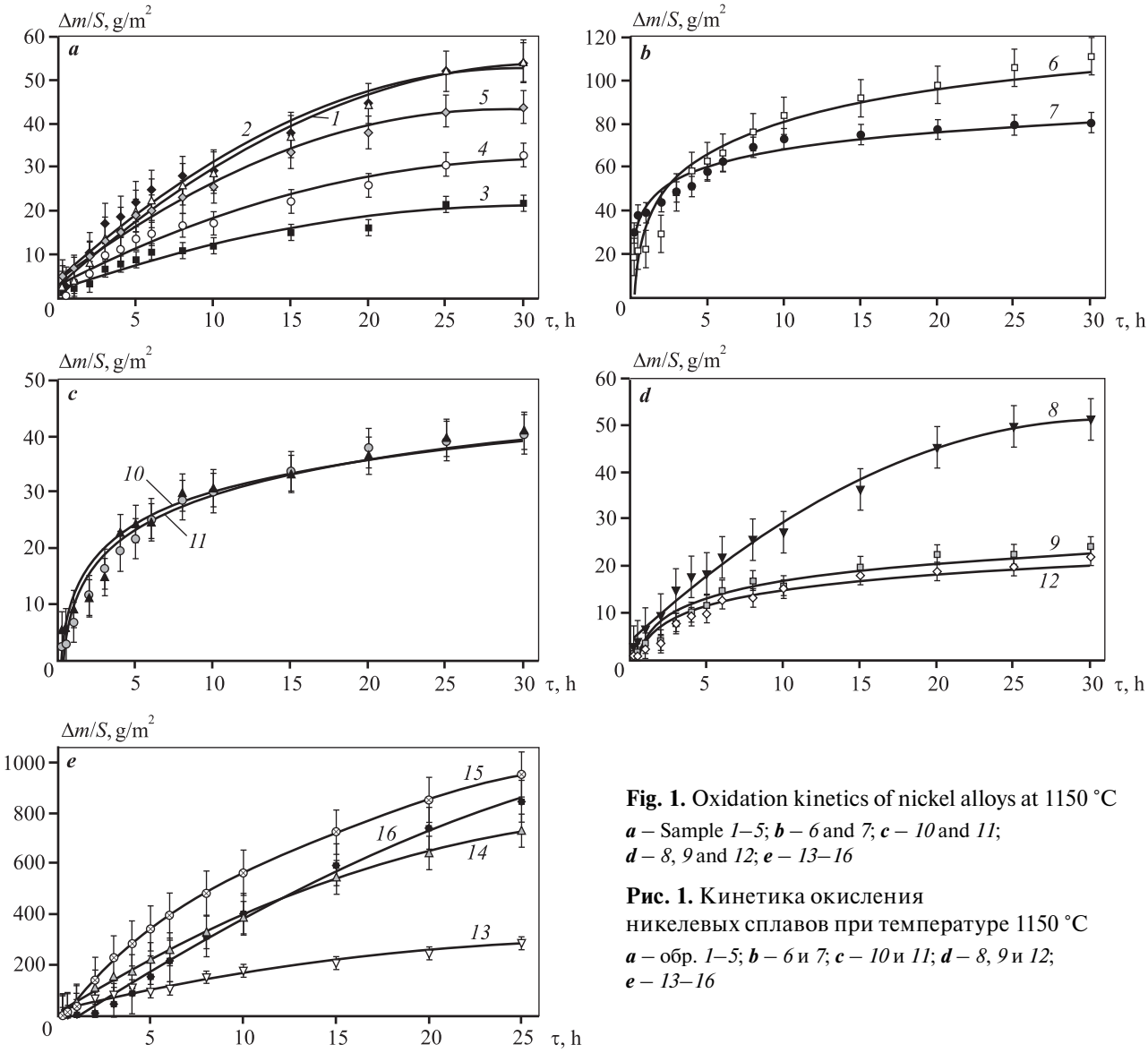

Fig. 1. Oxidation kinetics of nickel alloys at 1150 °C
a – Sample *1–5*; ***b*** – *6* and *7*; ***c*** – *10* and *11*; ***d*** – *8*, *9* and *12*; ***e*** – *13–16*

Рис. 1. Кинетика окисления никелевых сплавов при температуре 1150 °C
a – обр. *1–5*; ***b*** – *6* и *7*; ***c*** – *10* и *11*; ***d*** – *8*, *9* и *12*; ***e*** – *13–16*

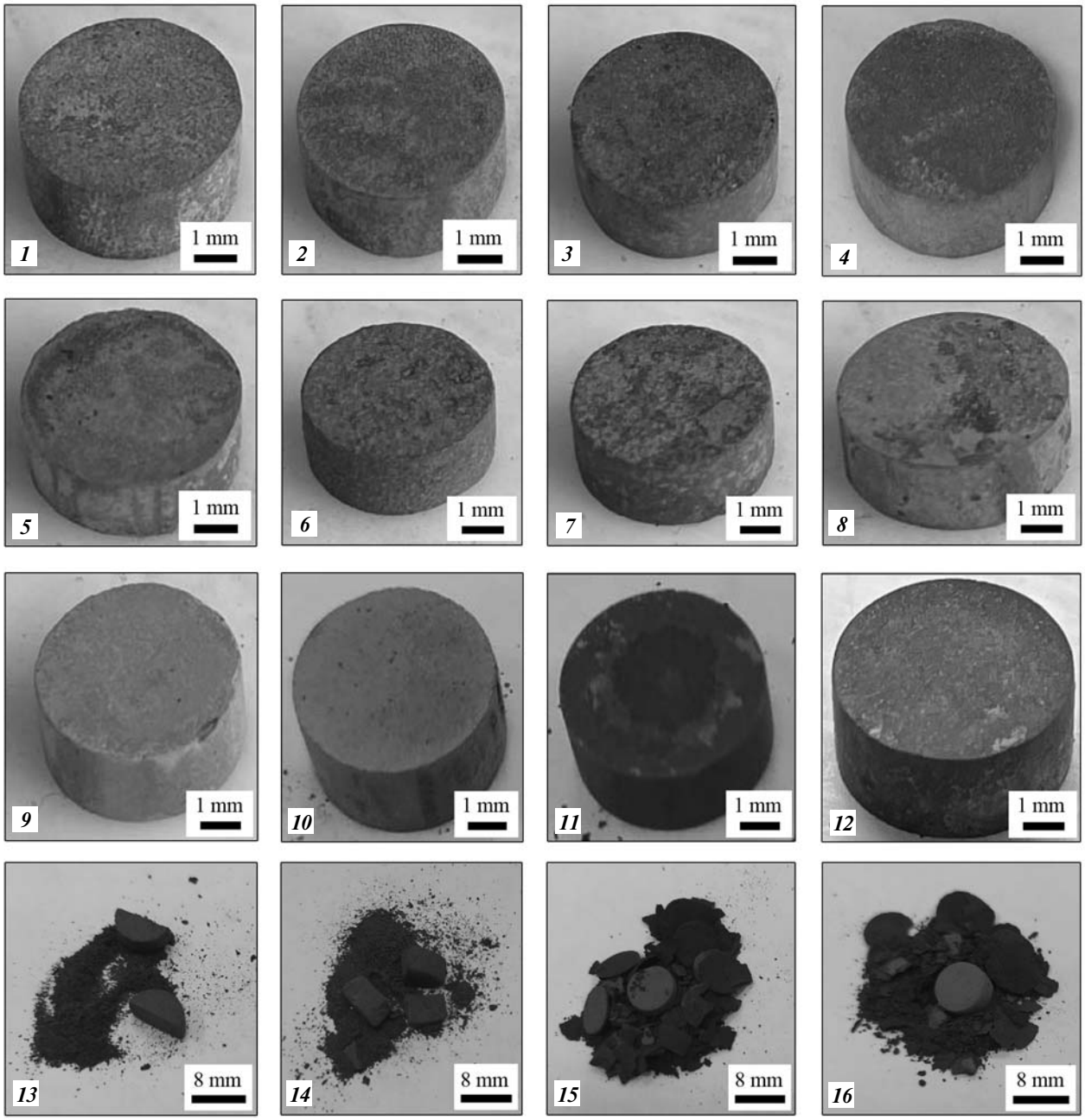

Fig. 2. Appearance of β alloys, EP741NP, AZhK samples after heat resistance tests at $t = 1150$ °C for 30 hours

Рис. 2. Внешний вид образцов из β-сплавов, ЭП741НП, АЖК после испытаний на жаростойкость при $t = 1150$ °C в течение 30 ч

internal stresses. This is confirmed by the change in their color and a friable surface, as seen in Figure 2. The oxidation kinetics of samples *9—12* depends on the content of molybdenum, niobium, hafnium and the size of the β-phase grains. The HfO_2 particles located at grain interfaces block the surface diffusion of aluminum and oxygen.

On the surface of oxidized samples, a layer with a certain relief and shade (see Figure 2) is visible. Visual analysis of samples *1—12* shows the absence of physical destruction. Samples *13* and *14* fractured in full due to the release of volatile molybdenum suboxides. At a lower content of Mo in the alloy (sample *11*) the samples did not fracture.

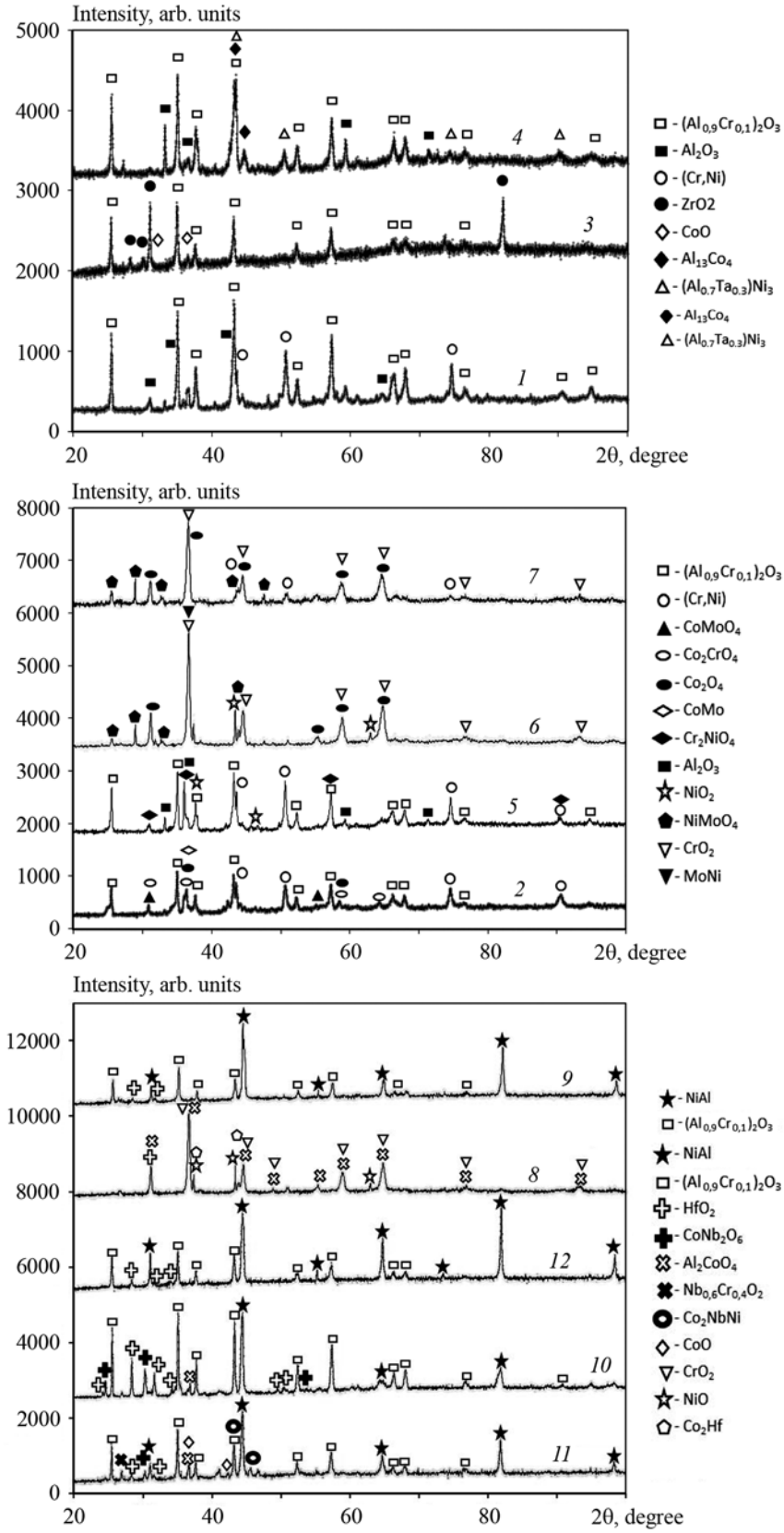

Fig. 3. XRD spectra of the oxidized surface of samples

Рис. 3. Дифракционные спектры окисленной поверхности образцов

Samples *15* and *16* from alloys EP741NP and AZhK also fractured completely. As a result of diffusion there is a high concentration of excess vacancies under the oxide layer. When critical thickness is reached, there is gradual cracking of the film with transformation into a loose oxide. The operating temperatures of parts made of these alloys are limited to the interval of 750—800 °C [28], which is noticeably lower than the test temperature of 1150 °C. However, our work was aimed at a comparative analysis of the oxidation kinetics of a group of alloys under the same conditions.

The diffraction spectra of the surface of β-alloys, oxidized at t = 1150 °C for 30 h, are shown in Figure 3. The main peaks correspond to the nickel monoaluminide (NiAl) phase as the alloying additives pass into a solid solution. The main oxidation prod-

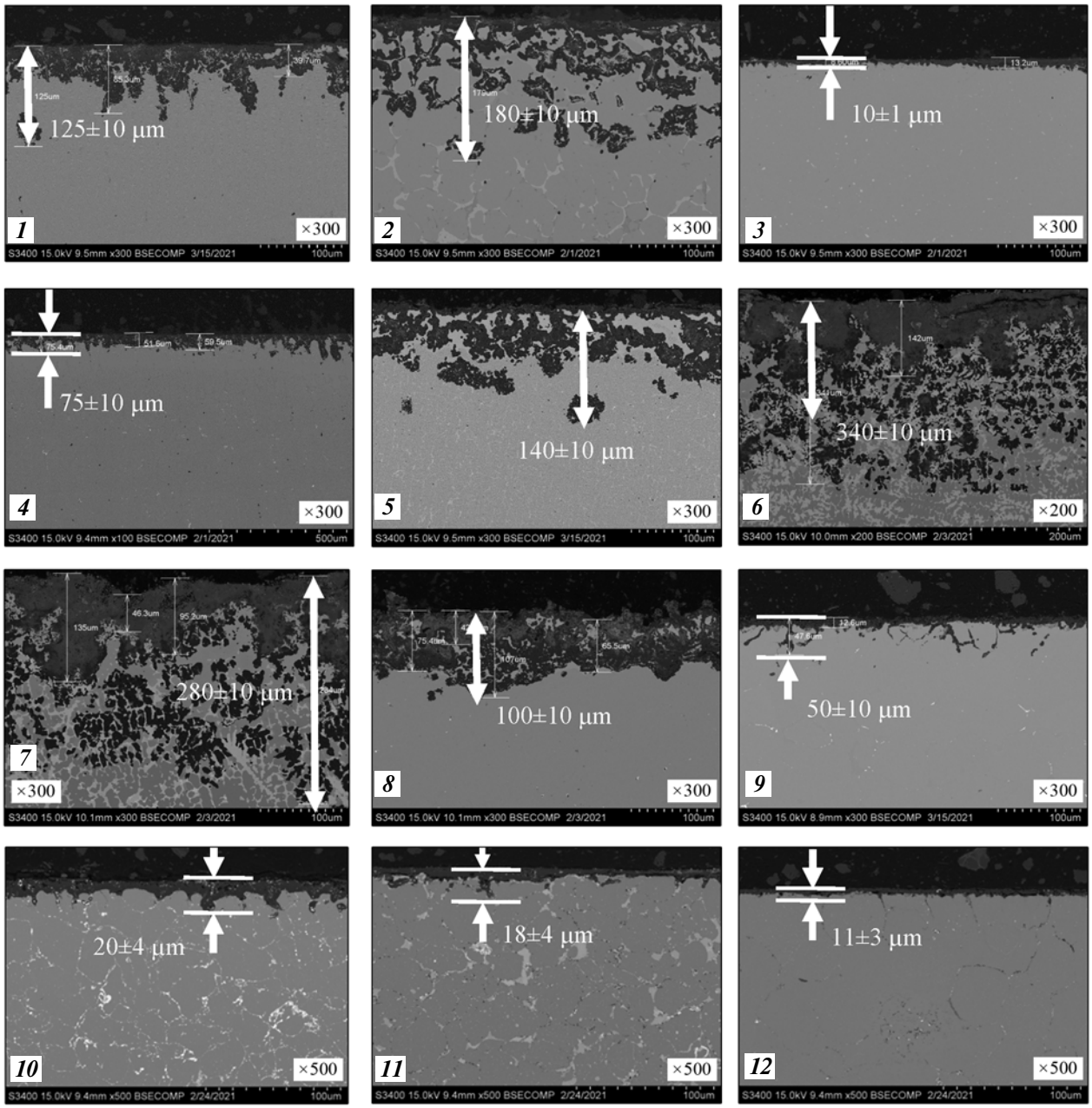

Fig. 4. Microstructures of alloys indicating the oxidized layer thickness

Рис. 4. Микроструктуры сплавов с указанием толщины окисленного слоя

uct is γ-Al_2O_3, and some accompanying oxides are present.

Figure 4 shows the microstructures of oxidized and transition layers of the study samples with the indication of typical thicknesses. A feature of the alloys under study with different alloying systems is the formation of a continuous, tightly adhering oxide film at the initial oxidation stage. This inhibits the diffusion penetration of oxygen and nitrogen to the metal. The analysis of the MeO—Me transition layer indicates diffusion of oxygen and nitrogen. The data presented in Figure 4 shows the influence of alloying elements, the molybdenum (2.5—15.0 at.%) and hafnium content (0.25—0.9 at.%), as well as the alloy production method (SHS-M, VIR, ES, HIP) on the oxidation depth and thickness of the transition Me—MeO layer. A more detailed analysis for each composition is presented in Figures 5—17.

Sample *1* has a considerably lower (in comparison with calculation) content of lanthanum. This is due to

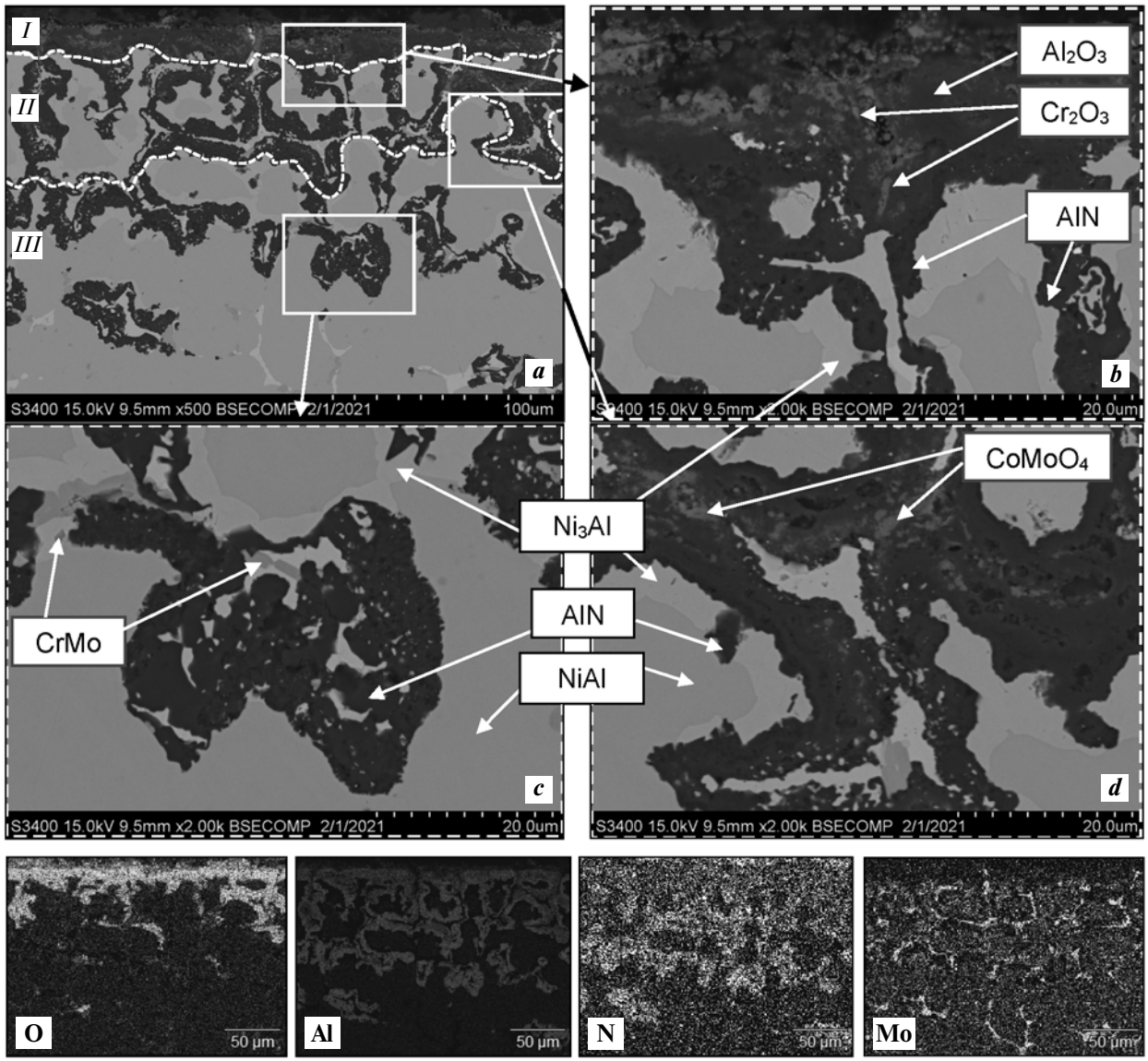

Fig. 5. Microstructure (***a***), marked analysis areas (***b***–***d***) and map of oxidized layer element distribution in Sample *2* (see table)

Рис. 5. Микроструктура (***a***), выделенные области анализа (***b***–***d***) и карта распределения элементов окисленного слоя в обр. *2* (см. таблицу)

its high affinity to oxygen, participation in the reduction metallothermic reaction during synthesis and partial transition into a slag phase [26]. Therefore, the alloy with low lanthanum content was excluded from further studies.

Figure 5 shows microstructures of the oxidized layer of sample *2* with molybdenum. Diffusion of oxygen and nitrogen occurs predominantly at grain interfaces and intergranular interlayers of phases containing Cr—Mo. At the NiAl—MeO interfaces, the Ni_3Al phase can be observed as a result of Al_2O_3 formation and aluminum depletion of the NiAl phase.

Analysis of samples after 30 h of testing shows the Me—MeO transitional layer. At the initial stage there is reactive diffusion of oxygen along the grain interfaces of the β-phase solid solution with the formation of a solid Al_2O_3 and Cr_2O film. At the same time, nitrogen also diffuses deep into the sample, reacting with aluminum to form AlN, and depleting NiAl to Ni_3Al (light gray areas). In the molybdenum-doped alloy, maximum thick-

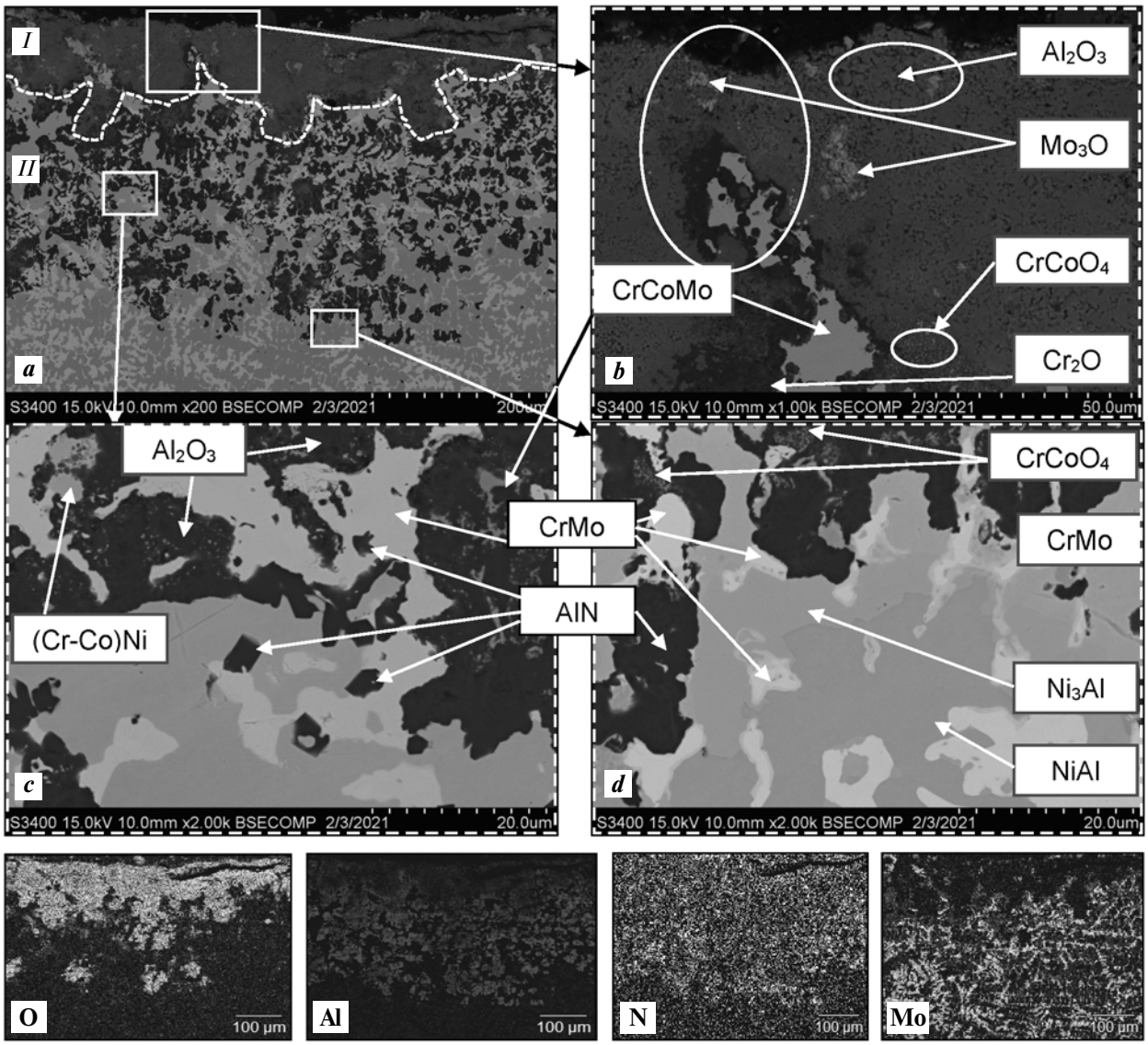

Fig. 6. Microstructure (***a***), marked analysis areas (***b–d***) and map of oxidized layer element distribution in Sample *6*

Рис. 6. Микроструктура (***a***), выделенные области анализа (***b–d***) и карта распределения элементов окисленного слоя в обр. *6*

ness of the transition layer can be observed (see Figure 4). Molybdenum in oxidation forms oxides MoO_3, Mo_3O_4 and $CoMoO_4$, which sublimate and lead to periodic destruction of the integrity of the protective layer. This then contributes to the diffusion of new portions of active nitrogen and oxygen ions.

Thus, this cyclic mechanism is used to move the oxidation front deep into the sample, as confirmed by the studies of sample *6* with an increased content of molybdenum, the results of which are shown in Figures 4 and 6.

A characteristic difference of sample *6* is penetration of oxygen and nitrogen to the depth of up to 340±10 μm (see Figure 4). In Figure 6, we can identify the appearance of more areas of oxide and nitride components. In addition, the burning out of molybdenum in the form of suboxides affects the thickness of the surface oxide layer: 20±5 μm for sample *2*; and 130±5 μm for sample *6*. A distinctive feature of the oxidation kinetics of the latter is the more intense inhibition of the film growth over time according to the logarithmic law. Oxidation starts at a high rate, but its value quickly decreases and is further controlled by the process of electron transfer through the oxide film.

Figure 7 shows the characteristic microstructures of the MeO—Me transition layer in sample *4* with tantalum. The analysis of the kinetic curves of high-temperature oxidation revealed that the modification with tantalum makes a positive result, slowing down the oxidation rate (see Figure 1, *a*).

Distribution of oxygen and nitrogen in the oxidized layer can be conventionally divided into three sublayers: *I* — solid oxide film of Al_2O_3 with Ta_2O_5, Cr_2O_3 inclusions and a small amount of AlN; *II* — oxides with predominantly AlN content; *III* — metallic layer with nitride inclusions and without oxides.

Tantalum located in the intergranular space is oxidized to Ta_2O_5. Compared to the Mo-containing system, the β-phase depletion to Ni_3Al does not occur. A detailed study of the structure of the Ta-containing alloy [26] established the concentration shift of chromium dissolved in the β-phase solid solution to the grain

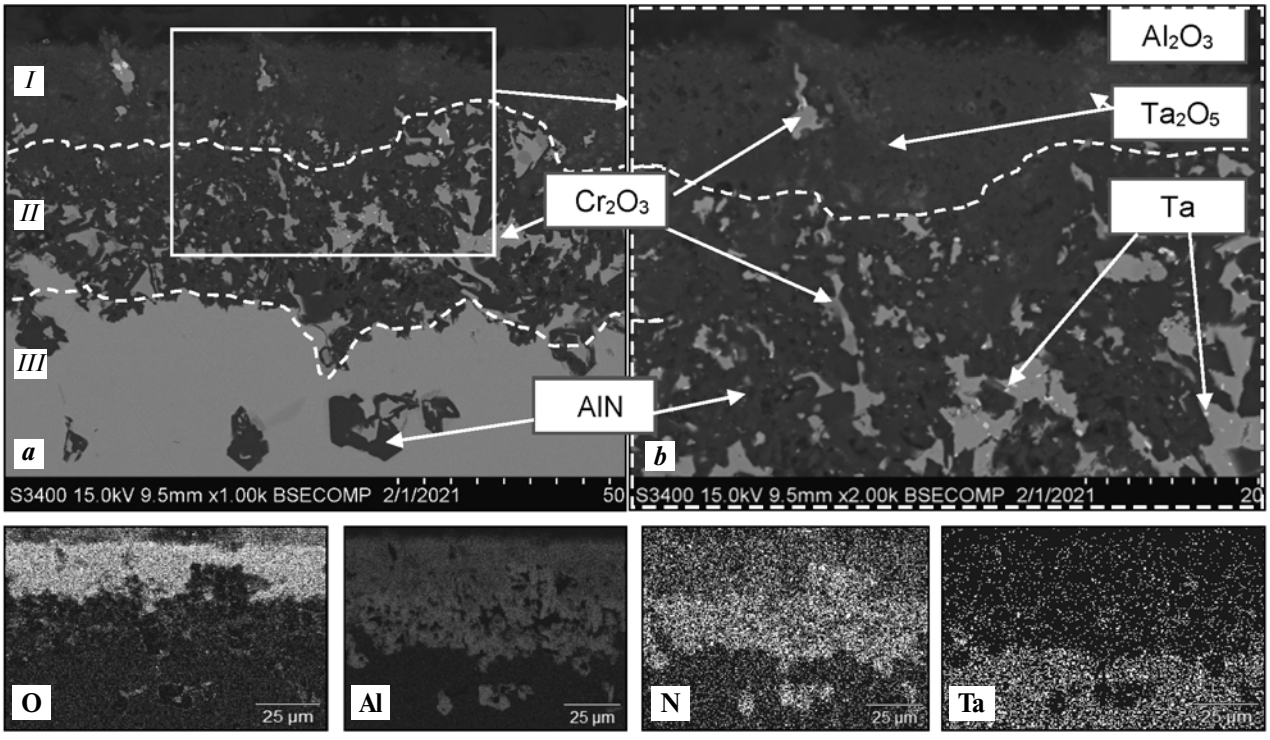

Fig. 7. Microstructure (***a***), marked analysis area (***b***) and map of oxidized layer element distribution in Sample *4*

Рис. 7. Микроструктура (***a***), выделенная область анализа (***b***) и карта распределения элементов окисленного слоя в обр. *4*

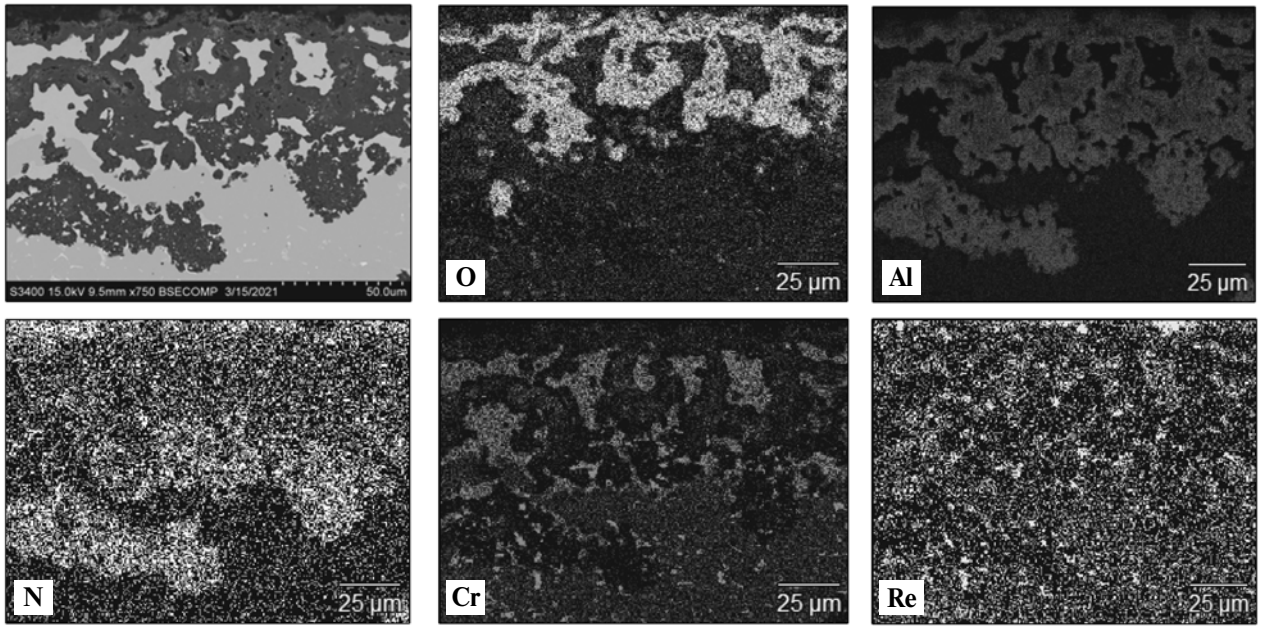

Fig. 8. Microstructure and map of oxidized layer element distribution in Sample *5*

Рис. 8. Микроструктура и карта распределения элементов окисленного слоя в обр. *5*

interfaces. Thus, in the first place, chromium interacts with oxygen to form a volatile oxide. It is due to these two distinctive features that the oxidation rate is reduced.

In the comparative analysis of sample *3* with the basic composition, a slight slowdown of oxidation processes can be observed (see Figure 1, *a*, *d*). The reason for the decrease in the oxidation rate can be traced from microstructures and the elements distribution map of the MeO—Me transition layer presented in Figure 7. As shown above, in the parabolic dependence, diffusion along the interfacial boundaries is the controlling process.

The total depth of the oxidized layer decreases as the size of the structural components decreases, the grain interfaces branch and the diffusion path increase. This is confirmed in the case of rhenium-modified alloy (see Figure 1, *a*). Figure 1, *b* shows the comparison of kinetic oxidation curves for samples *6* and *7*. This also confirms a decrease in the dynamics of oxidation processes with additional alloying with rhenium. The oxidation of alloys with rhenium does not form a dense layer of Al_2O_3 on the surface, which has a negative effect on the heat resistance. The main recommendation in this case is to use combined alloying, in order to introduce, along with rhenium, an element that inhibits oxidation processes, such as zirconium.

Figure 9 shows microstructures of the oxidized layer of sample *3* with zirconium. This alloying system showed the best result in a series of experiments (see Figure 1, *a*). The SEM images of the cross section of oxidized sample *3* are shown in Figures 9 and 10. The thickness of the oxidized layer was 10±5 μm, which is an order of magnitude smaller than in the other samples. In Figure 9, we can identify the Al_2O_3 layer with inclusions of chromium-cobalt oxide phases characteristic of all samples. The white light dots distributed throughout the oxidized layer correspond to the ZrO_2 phase. Nanosized ZrO_2 formations are present in the main Al_2O_3-based layer (see Figures 9, *c* and 10).

Analysis of Figure 10 shows that under the Al_2O_3 + + ZrO_2 layer there is a thin continuous film of Cr_2O_3, which is typical for this alloying system. The upper oxide layer of Al_2O_3 + ZrO_2 presumably inhibits the external diffusion of oxygen and nitrogen, and also blocks the sublimation of volatile chromium oxide Cr_2O_3. Thus, it gradually forms a dense layer across the Me—MeO transition surface, forming a second continuous barrier oxide layer.

The oxide layer of sample *3* with zirconium after heat-resistance tests was chosen for the analysis by HRTEM and electron beam diffraction on a JEM-2100 microscope (Jeol, Japan). Figure 11 shows an image of the alloy structure and the oxide layer formed, as well

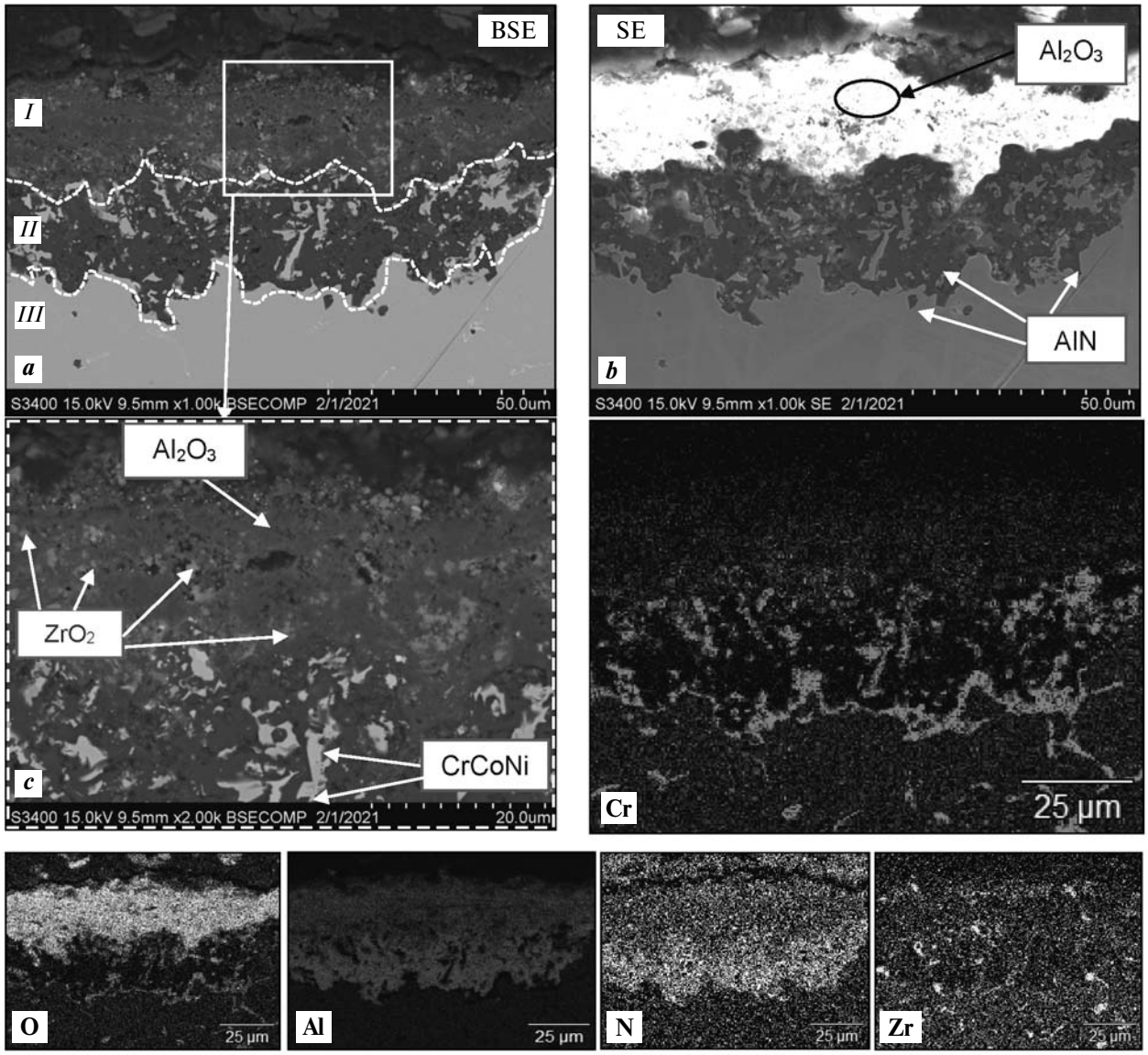

Fig. 9. Microstructure (***a***), marked analysis areas (***b***, ***c***) and map of oxidized layer element distribution in Sample *3*

Рис. 9. Микроструктура (***a***), выделенные области анализа (***b***, ***c***) и карта распределения элементов окисленного слоя в обр. *3*

as a map of distribution of the main elements therein. Between the NiAl matrix layer and the outer oxide layer there is a layer of the Ni_3Al phase with evenly distributed inclusions of Co, Cr, and Cr_2O_3. The upper oxide layer consists of Al_2O_3 with inclusions of ZrO_2 (dark gray areas), confirming the results of the EDX analysis (Figure 12, spectra *1*, *3*, *4*). Based on the quantitative ratio of the main components in spectral region *2* (Figure 12), the phase was investigated by HR TEM and electron beam diffraction, thus establishing the phase of complex oxide $Zr_5Al_3O_{0.5}$ (Figure 13).

The $Zr_5Al_3O_{0.5}$ phase has a hexagonal crystal lattice (space group $P6_3mc$). The lattice periods of the $Zr_5Al_3O_{0.5}$ phase, calculated on the basis of the electron diffraction pattern, with regard to the Miller indices are: $a = 14.153$ Å, $c = 5.671$ Å.

Thus, high-temperature oxidation produces a complex oxide in the form of nano-sized crystallites $Zr_5Al_3O_{0,5}$ impregnated into the Al_2O_3 layer. This combination reduces the catalytic activity and positively affects the oxidation resistance of the alloy at $t = 1150$ °C.

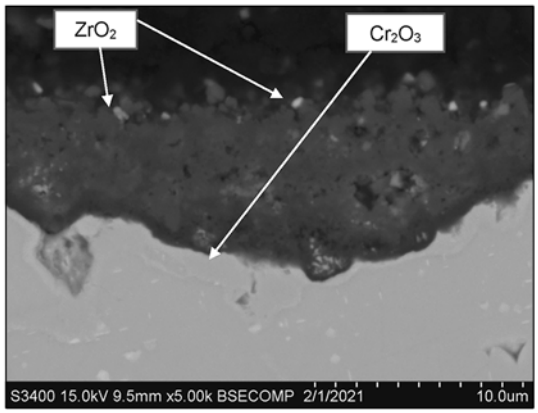

Fig. 10. Microstructure and map of MeO–Me layer element distribution in Sample *3*

Рис. 10. Микроструктура и карта распределения элементов слоя MeO–Me в обр. *3*

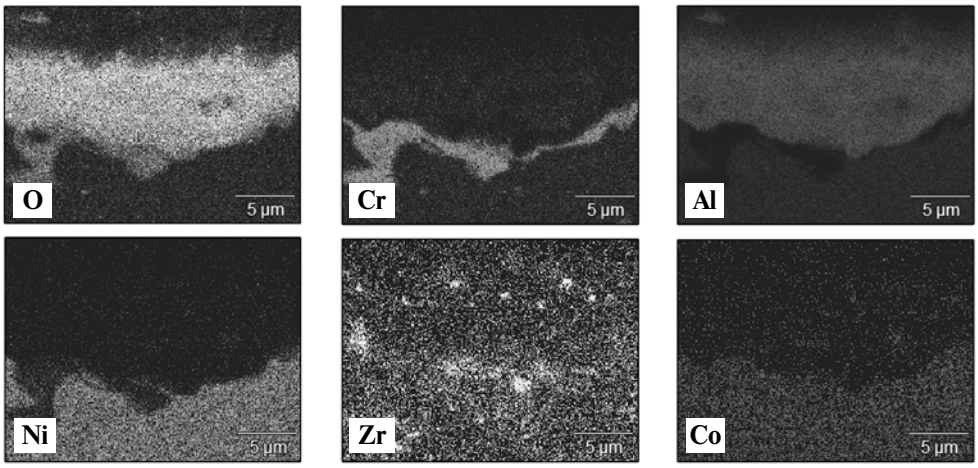

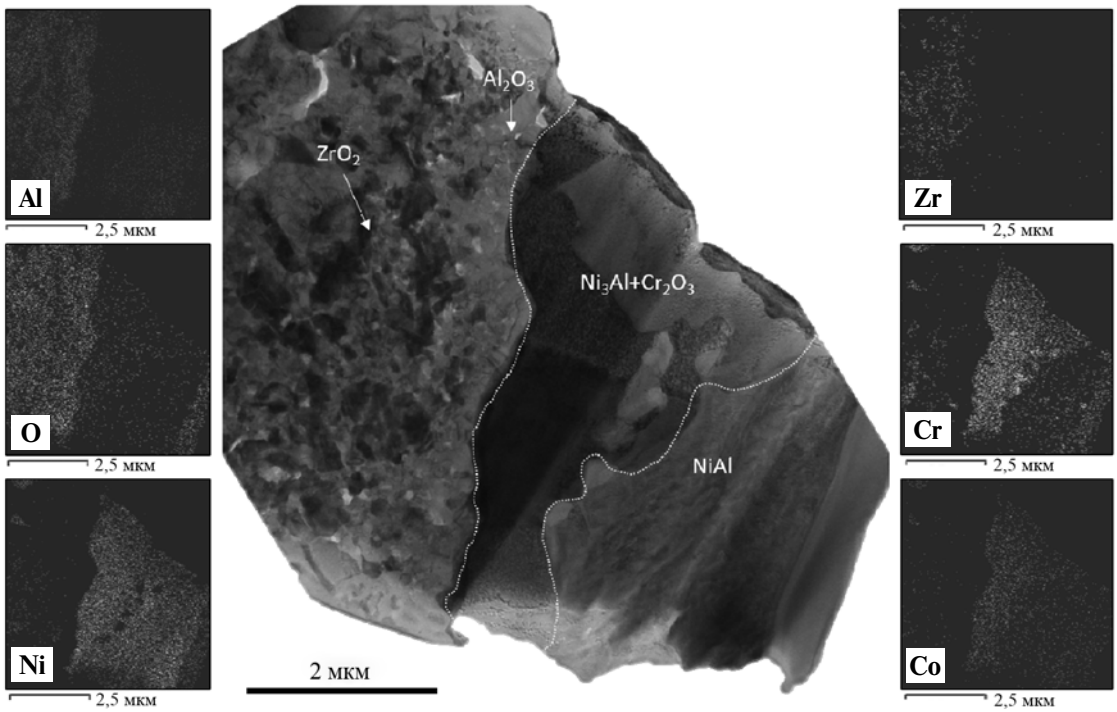

Fig. 11. TEM image of Sample *3* structure, oxide layer formed and map of main element distribution

Рис. 11. ПЭМ-изображение структуры обр. *3* и образовавшегося оксидного слоя, а также карта распределения основных элементов

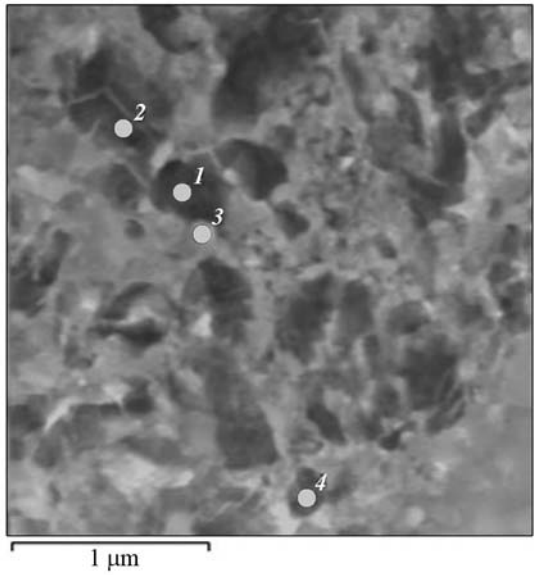

Spectrum	O	Al	Cr	Co	Ni	Zr
1	54.65	3.93	–	–	–	41.42
2	45.28	23.69	–	–	–	31.04
3	56.35	37.55	3.91	0.46	0.78	0.95
4	58.27	3.22	–	–	–	38.51

Fig. 12. Chemical composition (at.%) of boundary oxide layer regions

Рис. 12. Химический состав (ат.%) областей пограничного оксидного слоя

Comparative analysis of oxidation curves (see Figure 1, *d*), as well as the composition and microstructure of oxidized samples (Figures 14, 15) from the basic β-alloy, obtained by different process flowcharts: SHS-M [18] (Figure 8), SHS-M + VIR [18, 19] (Figure 9), ES with subsequent spheroidization of the powder and HIP [20] (sample 12), showed that the technology used has an effect on their heat resistance. Figure 1, *d* shows the difference in the oxidation kinetics of sample *8* (SHS-M) from samples *9* and *12* subjected to additional after-treatment.

Analysis of the microstructure (see Figures 4, 14) of the transition layer of samples *8* (SHS-M) and *9* (SHS-M + VIR) demonstrates a 2-fold difference in the thickness of the oxide and transition layers: 100±10 and 50±10 μm, respectively. In sample *9* (SHS-M + VIR), the AlN phase is not formed in the MeO—Me transition layer, indicating that the metal is refined during VIR [19]. The impurity nitrogen content in samples *8* and *9* is [N] = 0.0044 and 0.00083 wt.%, respectively. Its reduction leads to a different oxidation mechanism similar to that of sample *3*. Here a dense protective Cr_2O_3 sublayer is formed under a loose Al_2O_3 + Cr_2O_3 layer. In this oxidation mechanism, diffusion occurs only at phase interfaces and penetrates deep into the sample in the form of «wedges» (see Figure 14, *b*).

The VIR process is a useful way of refining alloys from detrimental impurities. However, it also has some

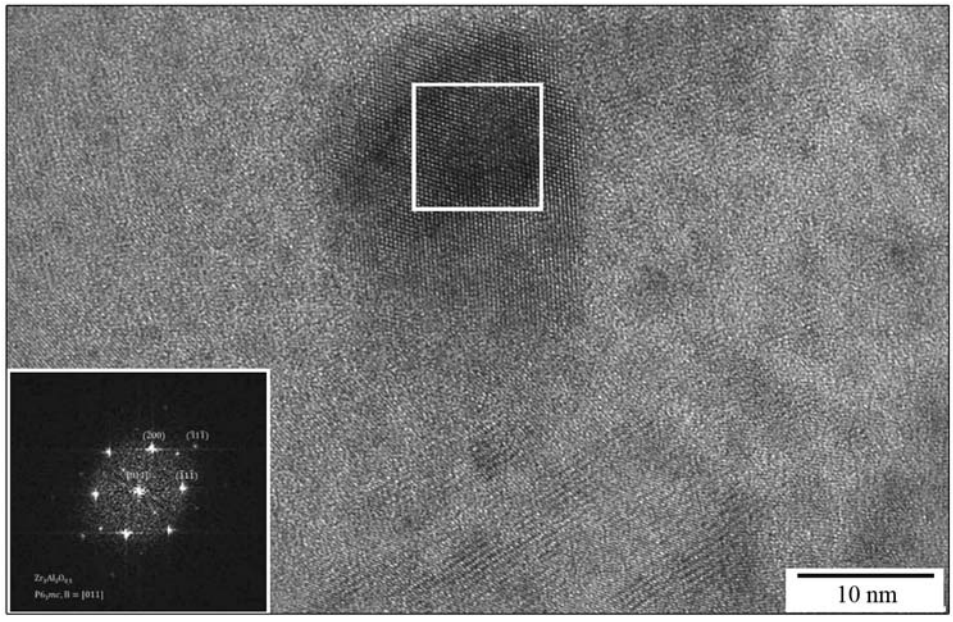

Fig. 13. TEM image of the $Zr_5Al_3O_{0.5}$ phase with an electron diffraction pattern along the zone [011] axis

Рис. 13. ПЭМ-изображение фазы $Zr_5Al_3O_{0,5}$ с электронограммой вдоль оси зоны [011]

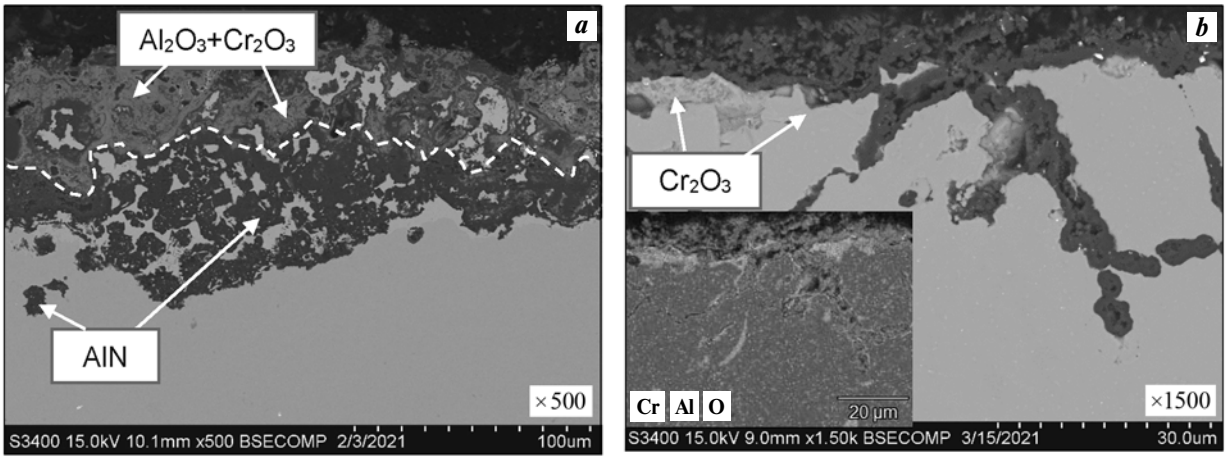

Fig. 14. Microstructure of the oxidized layer of Sample *8* (SHS-M) (***а***) and Sample *9* (SHS-M + VIR) (***б***)

Рис. 14. Микроструктура окисленного слоя образцов *8* (СВС-М) (***а***) и *9* (СВС-М + ВИП) (***б***)

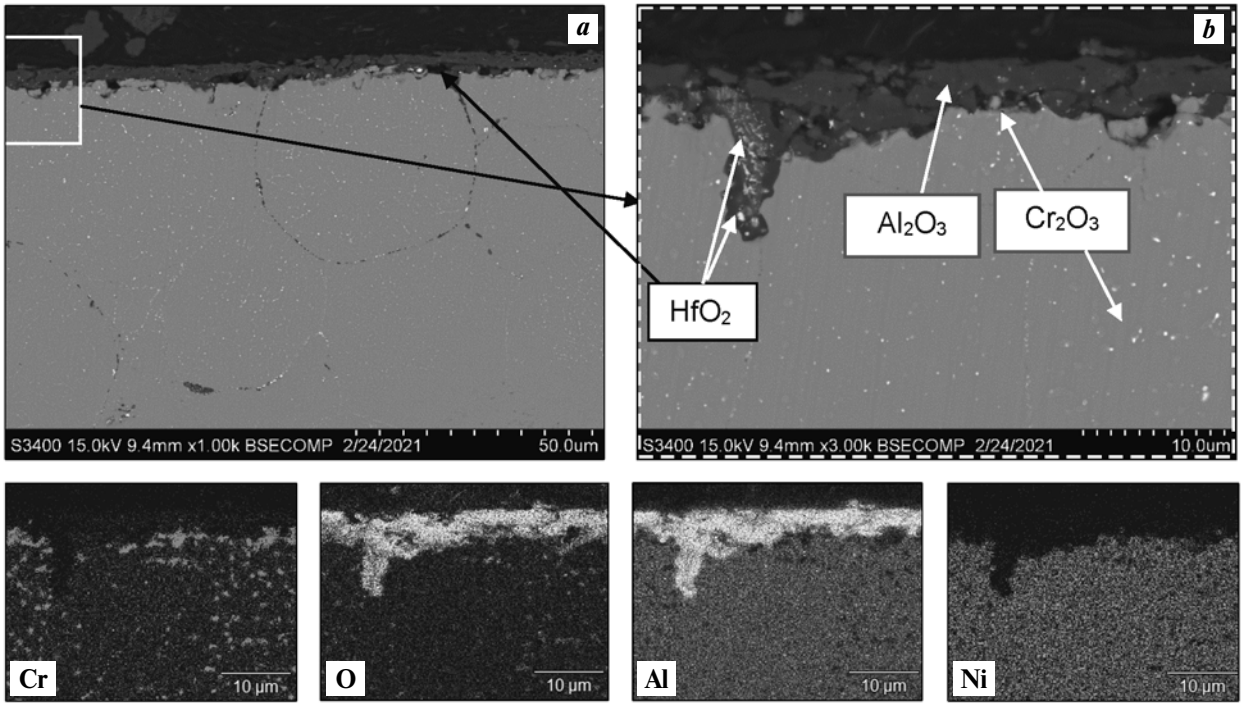

Fig. 15. Microstructure (***а***, ***б***) and map of oxidized layer element distribution in Sample *12* (ES + HIP)

Рис. 15. Микроструктура (***а***, ***б***) и карта распределения элементов в окисленном слое обр. *12* (ЭС + ГИП)

drawbacks described in [18—20]. A more efficient and less energy-consuming method for refining cast SHS alloys is vacuum annealing at $t = 0.7$tm, which removes up to 70 % of impurity nitrogen and hydrogen. The reduction of residual oxygen content is possible only during full metallurgical processing (VIR). Sample 12 (ES + HIP) has similar kinetics to sample *9* (see Figure 1, *d*), while the mechanisms of counteracting the diffusive penetration of oxygen and nitrogen are different.

The impurity oxygen content in these systems is [O] ≤ 0.12 wt.%. [20]. The oxidation process in the alloy begins at the interfaces of the consolidated powders. The element distribution map demonstrates the distribution areas of Al_2O_3 and Cr_2O_3 oxides, contributing to the destruction of samples, along with

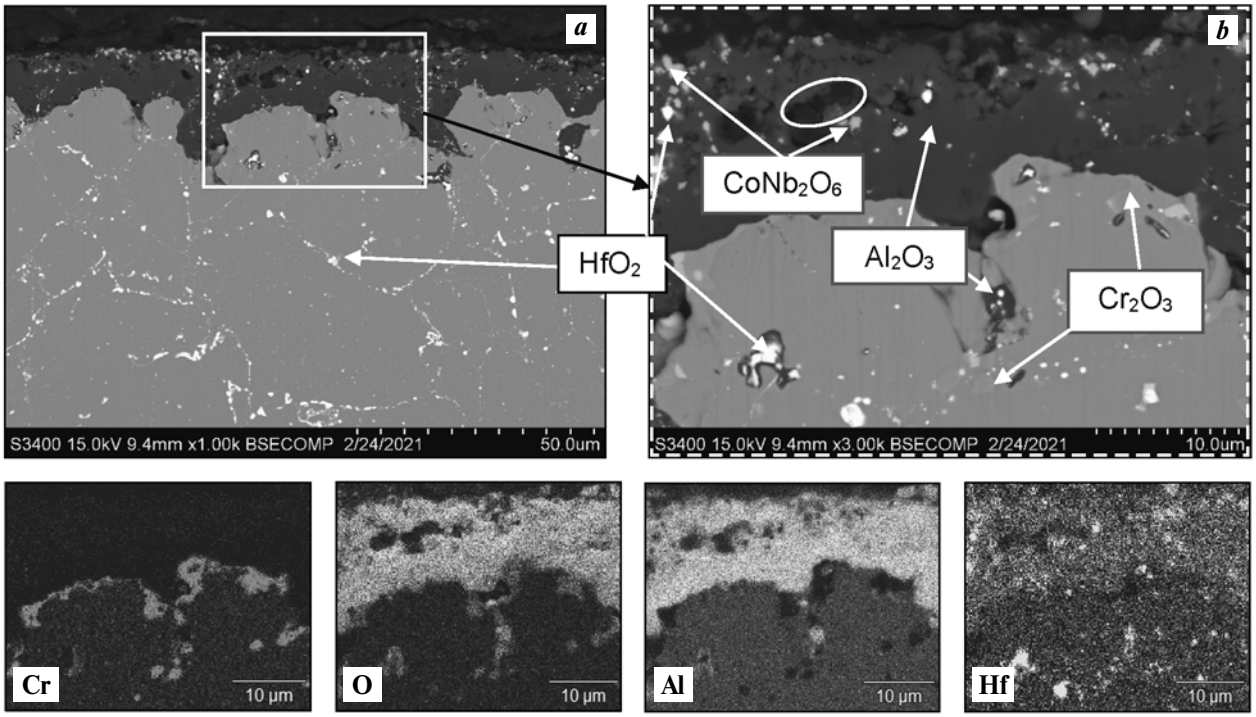

Fig. 16. Microstructure (***а***, ***б***) and map of oxidized layer element distribution in Sample *10* (ES)

Рис. 16. Микроструктура (***а***, ***б***) и карта распределения элементов окисленного слоя в обр. *10* (ЭС)

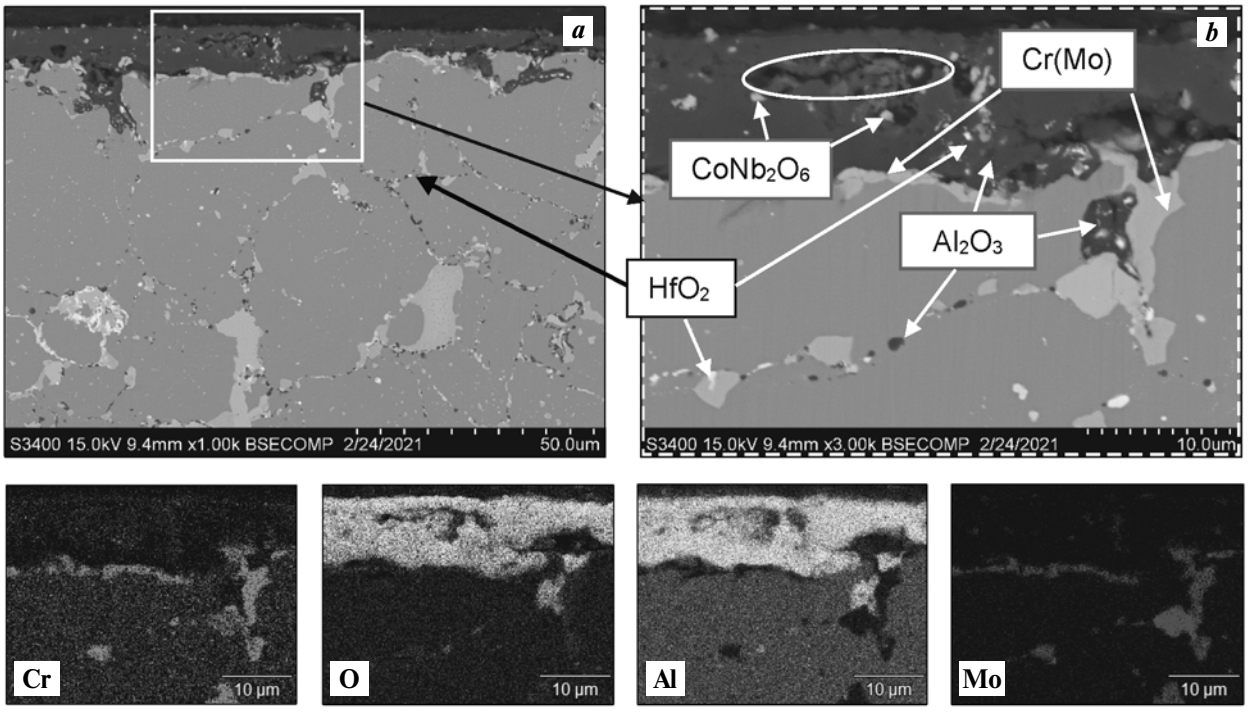

Fig. 17. Microstructure (***а***, ***б***) and map of oxidized layer element distribution in Sample *11* (ES)

Рис. 17. Микроструктура (***а***, ***б***) и карта распределения элементов окисленного слоя в обр. *11* (ЭС)

the action of volatile molybdenum oxides (samples *13* and *14*).

The mechanisms of protection against external diffusion of oxygen and nitrogen in sample *12* (ES + HIP) and *9* (SHS + VIR) are similar and depend on the formation of a thin protective film of Cr_2O_3. When the nitrogen content in the sample is less than 0.0017 wt.%, the AlN phase is not formed during oxidation [25]. In fine-grained samples (ES + HIP) [25], the limiting factor for oxygen penetration deep into the sample is a branched system of grain interfaces.

Figures 16 and 17 show the microstructures of the oxidized layer of samples *10* and *11* obtained by the ES method [27]. Comparing the kinetic functions of their oxidation to the SHS-M samples, similar patterns can be noted. However, analysis of the microstructures showed that their oxidation mechanisms are somewhat different. The primary layer consists of Al_2O_3 with inclusions of HfO_2, $CoNb_2O_6$, but in the oxide layer the pores noted in Figures 16 and 17 are formed by evaporation of volatile niobium and molybdenum suboxides. The latter destroy the primary Al_2O_3 layer, leading to intense oxidation at the initial stage (see Figure 1, *c*). Larger niobium inclusions in the oxide layer of the alloy form the $CoNb_2O_6$ phase. Hafnium oxide HfO_2 is uniformly distributed as submicron and nanoscale inclusions along the grain interfaces, thereby suppressing oxygen diffusion inside nickel aluminide [29]. In sample *10*, a thin protective layer of Cr_2O_3 is observed under the Al_2O_3 layer.

In alloy *11* the Cr(Mo) solid solution phase is also located at the grain interfaces along with HfO_2 inclusions. The initial oxidation period is similar to that of sample *10*. However, due to the molybdenum there is more active oxygen diffusion deep into the sample at the grain interfaces with the formation of Al_2O_3 and volatile MoO_3, which are sublimated and do not impede further oxygen penetration.

Conclusion

1. Kinetic curves were constructed and equations corresponding to them were established for approximation of the oxidation process at t = 1150 °C for 30 h of various heat resistant nickel alloys based on nickel monoaluminide obtained by centrifugal SHS metallurgy (SHS-M), vacuum induction remelting (VIR), elementary synthesis (ES) and hot isostatic pressing (HIP). Depending on the alloy composition and the method of its production, the nature of the curves corresponds to parabolic, logarithmic or mixed oxidation laws.

In the case of alloys AZhK and EP741NP, at the initial stage (3—4 h) a parabolic dependence is observed, and after violation of the sample integrity the oxidation character obeys a linear law and is controlled by the rate of the chemical reaction.

2. Alloying interstitial elements contribute to the growth of oxidation resistance of β-alloys. This is due to the formation of additional phases. In the sample (SHS-M) alloyed with tantalum, the Ta_2O_5 phase is formed in the intergranular space, which reduces the oxidation rate and depth.

A zirconium-doped sample (SHS-M) showed the best result: the degree of oxidation for 30 h was 21 g/m^2. The zirconium-containing top layer of Al_2O_3 + + $Zr_5Al_3O_{0.5}$ blocks the external diffusion of oxygen and nitrogen, thereby increasing the heat resistance.

Hafnium alloying causes the formation of submicron and nanoscale inclusions of HfO_2 at the grain interfaces, suppressing the grain interface diffusion of oxygen, and a thin protective Cr_2O_3 layer is formed under the Al_2O_3 layer.

In alloys with molybdenum volatile oxides of MoO_3, Mo_3O_4, and $CoMoO_4$ are formed which destroy the integrity of the protective layer. As the concentration of molybdenum increases, the depth of oxygen and nitrogen penetration increases, too.

3. Comparative analysis of the kinetics and mechanism of oxidation of basic β-alloy samples with chromium, cobalt and hafnium additions showed a significant effect on the heat resistance of the method of obtaining samples. The oxidation mechanism also changes with the reduction of the percentage of impurity nitrogen and formation of the Cr_2O_3 sublayer.

Acknowledgments: *The research was funded by the Ministry of Science and Higher Education of the Russian Federation (Government Task Project No. 0718-2020-0034).*

Работа выполнена при финансовой поддержке Министерства науки и высшего образования Российской Федерации (проект государственного задания № 0718-2020-0034).

References

1. *Логунов А.В.* Жаропрочные никелевые сплавы для лопаток и дисков газовых турбин. М.: ИД «Газотурбинные технологии», 2017.

Logunov A.V. Heat-resistant nickel alloys for blades and disks of gas turbines. Moscow: «Gazoturbinnye tekhnologii», 2017 (In Russ.).

2. *Hu L., Zhang G., Hu W., Gottstein G., Bogner S., Bührig-Polaczek A.* Tensile creep of directionally solidified NiAl—9Mo in situ composites. *Acta Mater.* 2013. Vol. 61. P. 7155—7165. DOI: 10.1016/j.actamat.2013.08.017.
3. *Seemüller C., Heilmaier M., Haenschke T., Bei H., Dlouhy A., George E.P.* Influence of fiber alignment on creep in directionally solidified NiAl—10Mo in-situ composites. *Intermetallics.* 2013. Vol. 35. P. 110—115. DOI: 10.1016/j.intermet.2012.12.007.
4. *Bei H., George E.P.* Microstructures and mechanical properties of a directionally solidified NiAl—Mo eutectic alloy. *Acta Mater.* 2005. Vol. 53. P. 69—77. DOI: 10.1016/j.actamat.2004.09.003
5. *Shang Z., Shen J., Wang L., Du Y., Xiong Y., Fu H.* Investigations on the microstructure and room temperature fracture toughness of directionally solidified NiAl—Cr(Mo) eutectic alloy. *Intermetallics.* 2015. Vol. 57. P. 25—33. DOI: 10.1016/j.intermet.2014.09.012.
6. *Walter J.L., Cline H.E.* The effect of solidification rate on structure and high-temperature strength of the eutectic NiAl—Cr. *Metal. Mater. Trans. B.* 1970. Vol. 1. P. 1221—1229. DOI: 10.1007/bf02900234.
7. *Cui C.Y., Chen Y.X., Guo J.T., Li D.X., Ye H.Q.* Preliminary investigation of directionally solidified NiAl—28Cr—5.5Mo—0.5Hf composite. *Mater. Lett.* 2000. Vol. 43. P. 303—308. DOI: 10.1016/S0167-577X(99)00278-5.
8. *Войтович Р.Ф., Головко Э.И.* Высокотемпературное окисление металлов и сплавов. Киев: Наукова думка, 1980.
   Voitovich R.F., Golovko E.I. High temperature oxidation of metals and alloys. Kiev: Naukova dumka, 1980.
9. *Klumpes R., Maree C.H.M., Schramm E., de Wit J.H.W.* The influence of chromiumon the oxidation of β-NiAl at 1000 °C. *Mater. Corros.* 1996. Vol. 47. P. 619—624.
10. *Johnson D.R., Chen X.F., Oliver B.F.* Processing and mechanical properties of in-situ composites from the NiAlCr and the NiAl(Cr,Mo) eutectic systems. *Intermetallics.* 1995. Vol. 3. P. 99—113. DOI: 10.1016/0966-9795(95)92674-O.
11. *Yang J.C., Schumann E., Levin I., Rühle M.* Transient oxidation of NiAl. *Acta Mater.* 1998. Vol. 46. P. 2195—2201.
12. *Grabke H.* Oxidation of NiAl and FeAl. *Intermetallics.* 1999. Vol. 7. No. 10. P. 1153—1158. DOI: 10.1016/S0966-9795(99)00037-0.
13. *Gao W., Li Z., Wu Z., Li S., He Y.* Oxidation behavior of Ni_3Al and FeAl intermetallics under low oxygen partial pressures. *Intermetallics.* 2002. Vol. 10. No. 3. P. 263—270. DOI:10.1016/S0966-9795(01)00132-7.
14. *Bo L., Fei L., Cong L., Yimin G., Congmin F., Xiaohu H.* Effect of Cr element on the microstructure and oxidation resistance of novel NiAl-based high temperature lubricating composites. *Corrosion Sci.* 2021. Vol. 188. Art. 109554. DOI: 10.1016/j.corsci.2021.109554.
15. *Geramifard G., Gombola C., Franke P., Seifert H.J.* Oxidation behaviour of NiAl intermetallics with embedded Cr and Mo. *Corrosion Sci.* 2020. Vol. 177. Art. 108956. DOI: 10.1016/j.corsci.2020.108956.
16. *Hea Y., Luo L., Sushko M., Liu C, Baer D., Schreiber D., Rosso K., Wang Ch.* Vacancy ordering during selective oxidation of β-NiAl. *Materialia.* 2020. Vol. 12. Art. 100783. DOI: 10.1016/j.mtla.2020.100783.
17. *Санин В.В., Филонов М.Р., Юхвид В.И., Аникин Ю.А., Михайлов А.М.* Исследование влияния температуры переплава на структурную наследственность сплавов, полученных методом центробежной СВС-металлургии. *Известия вузов. Цветная металлургия.* 2016. No. 1. С. 63—71. DOI: 10.17073/0021-3438- 2016-1-63-71.
   Sanin V.V., Filonov M.R., Yukhvid V.I., Anikin Y.A., Mikhailov A.M. Investigation into the influence of the remelting temperature on the structural heredity of alloys fabricated by centrifugal SHS metallurgy. *Russ. J. Non-Ferr. Met.* 2016. Vol. 57. No. 2. P. 124—130. DOI: 10.3103/S1067821216020097.
18. *Zaitsev A.A., Sentyurina Zh.A., Levashov E.A., Pogozhev Yu.S., Sanin V.N., Loginov P.A., Petrzhik M.I.* Structure and properties of NiAl—Cr(Co,Hf) alloys prepared by centrifugal SHS casting. Part 1 — Room temperature investigations. *Mater. Sci. Eng. A.* 2017. Vol. 690 P. 463—472. DOI: 10.1016/j.msea.2016.09.075.
19. *Zaitsev A.A., Sentyurina Zh.A., Levashov E.A., Pogozhev Yu.S., Sanin V.N., Sidorenko D.A.* Structure and properties of NiAl—Cr(Co,Hf) alloys prepared by centrifugal SHS casting followed by vacuum induction remelting. Part 2 — Evolution of the structure and mechanical behavior at high temperature. *Mater. Sci. Eng. A.* 2017. Vol. 690. P. 473—481. DOI: 10.1016/j.msea.2017.02.089.
20. *Kaplanskii Yu.Yu., Zaitsev A.A., Levashov E.A., Pogozhev Yu.S., Loginov P.A., Sentyurina Zh.A., Logacheva A.I.* The structure and properties of pre-alloyed NiAl—

Cr(Co,Hf) spherical powders produced by plasma rotating electrode processing for additive manufacturing. *J. Mater. Res. Technol.* 2018. Vol. 7. No. 4. P. 461—468. DOI: 10.1016/j.jmrt.2018.01.003.

21. *Kaplanskii Yu.Yu., Zaitsev A.A., Levashov E.A., Loginov P.A., Sentyurina Zh.A.* NiAl based alloy produced by HIP and SLM of pre-alloyed spherical powders. Evolution of the structure and mechanical behavior at high temperatures. *Mater. Sci. Eng. A*. 2018. Vol. 717. P. 48—59. DOI: 10.1016/j.msea.2018.01.057.
22. *Kurbatkina V.V.* Nickel aluminides. In: *Concise Encycl. Self-Propagating High-Temperature Synth*. Elsevier, 2017. P. 212—213. DOI: 10.1016/B978-0-12-804173-4.00099-5.
23. *Kurbatkina V.V., Patsera E.I., Levashov E.A., Kaplanskii Y.Y., Samokhin A.V.* Fabrication of narrow-fraction micropowders of nial-based refractory alloy compoNiAl—M5-3. *Int. J. SHS*. 2018. Vol. 27. P. 236—244. DOI: 10.3103/S1061386218040027.
24. *Tsvetkov Yu.V., Samokhin A.V., Alekseev N.V., Fadeev A.A., Sinaiskii M.A., Levashov E.A., Kaplanskii Yu.Yu.* Plasma spheroidization of micropowders of a heat-resistant alloy based on nickel monoaluminide. *Doklady Chemistry*. 2018. Vol. 483. Pt. 2. P. 312—317. DOI: 10.1134/S0012500818120030.
25. *Kaplansky Yu.Yu., Levashov E.A., Korotitskiy A.V., Loginov P.A., Sentyurina Zh.A., Mazalov A.B.* Influence of aging and HIP treatment on the structure and properties of NiAl-based turbine blades manufactured by laser powder bed fusion. *Additive Manufacturing*. 2020. Vol. 31. Art. 100999. DOI: 10.1016/j.addma.2019.100999.
26. *Sanin V.V., Kaplansky Y.Y., Aheiev M.I., Levashov E.A., Petrzhik M.I., Bychkova M.Y., Samokhin A.V., Fadeev A.A., Sanin V.N.* Structure and properties of heat-resistant alloys NiAl—Cr—Co—X (X = La, Mo, Zr, Ta, Re) and fabrication of powders for additive manufacturing. *Materials*. 2021. Vol. 14. No. 12. Art. 3144. DOI: 10.3390/ma14123144.
27. *Kaplanskii Y.Y., Levashov E.A., Bashkirov E.A., Korotitskiy A.V.* Effect of molybdenum on structural evolution and thermomechanical behavior of a heat-resistant nickel aluminide-based alloy. *J. Alloys Compd*. 2022, Vol. 892. Art. 162247. DOI: 10.1016/j.jallcom.2021.162247.
28. *Baskov F.A., Sentyurina Zh.A., Kaplanskii Yu.Yu., Logachev I.A., Semerich A.S., Levashov E.A.* The influence of post heat treatments on the evolution of microstructure and mechanical properties of EP741NP nickel alloy produced by laser powder bed fusion. *Mater. Sci. Eng. A*. 2021. Vol. 817. Art. 141340. DOI: 10.1016/j.msea.2021.141340.
29. *Zhang W.L., Li S.M., Fu L.B., Li W., Sun J., Wang T.G., Jiang S.M., Gong J., Sun C.* Preparation and cyclic oxidation resistance of Hf-doped NiAl coating. *Corrosion Sci*. 2022. Vol. 195. Art. 110014. DOI: 10.1016/j.corsci.2021.110014.

UDC 666.79
DOI dx.doi.org/10.17073/1997-308X-2022-3-24-36

Investigation of possibility of fabrication of long-length samples of Ti_3AlC_2–Al MAX-cermet by the SHS method with spontaneous infiltration by aluminum melt

© 2022 г. **A.P. Amosov, E.I. Latukhin, E.R. Umerov, D.M. Davydov**

Samara State Technical University (SSTU), Samara, Russia

Received 28.02.2022, revised 18.07.2022, accepted for publication 21.07.2022

Abstract: The article discusses the features of combining the self-propagating high-temperature synthesis (SHS) of the Ti_3AlC_2 MAX phase porous skeleton with infiltration by aluminum melt in a spontaneous mode in order to obtain enlarged samples of Ti_3AlC_2–Al ceramic-metal composite (MAX cermet) in an air atmosphere. A new scheme was developed for obtaining long-length SHS cermet samples from a bulk density charge with spontaneous infiltration by melt in the same direction with the combustion wave movement, which makes it possible to regulate the time gap between the end of the Ti_3AlC_2 synthesis and the beginning of the spontaneous pore filling with aluminum melt. This technology was used to obtain a Ti_3AlC_2 SHS skeleton with a total length of 250 mm and a diameter of 22–24 mm where the depth of infiltration with pure aluminum was about 110 mm, and impregnation with the Al–12%Si alloy was 130 mm. The paper provides comparative data on density, microstructure, and phase composition at different areas along the length of MAX cermet samples obtained. It was found that infiltration with pure aluminum destroys the Ti_3AlC_2 MAX phase to transform it into a mixture of TiC + $TiAl_3$ phases in the SHS cermet, and 12 % Si added to the Al melt promote Ti_3AlC_2 preservation in the cermet to a some extent. Instead of MAX cermet samples with the target composition of Ti_3AlC_2–Al and Ti_3AlC_2–(Al–12%Si), long-length samples of SHS cermets with a different actual phase composition were obtained: TiC–$TiAl_3$–Al and TiC–Ti_3AlC_2–$TiAl_3$–(Al–12%Si), respectively, where the Ti_3AlC_2 MAX phase either practically absent or present in small quantities. The average hardness values of TiC–$TiAl_3$–Al and TiC–Ti_3AlC_2–$TiAl_3$–(Al–12%Si) SHS cermets were *HB* = 640 and 740 MPa, density ρ = 2.88÷3.16 g/cm^3 and 3.03÷3.13 g/cm^3, and residual porosity *П* = 17.0÷24.6 % and 17.6÷20.3 %, respectively.

Keywords: self-propagating high-temperature synthesis (SHS), MAX phase, Ti_3AlC_2, spontaneous infiltration, MAX cermet, Ti_3AlC_2–Al, microstructure, phase composition, physical and mechanical properties.

Amosov A.P. – Dr. Sci. (Phys.-Math.), Prof., Head of the Department of physical metallurgy, powder metallurgy, nanomaterials (MPMN), Samara State Technical University (SSTU) (443100, Russia, Samara, Molodogvardeyskaya str., 244). E-mail: egundor@yandex.ru.

Latukhin E.I. – Cand. Sci. (Eng.), Associate prof., Department of MPMN, SSTU. E-mail: evgelat@yandex.ru.

Umerov E.R. – Postgraduate, Department of MPMN, SSTU. E-mail: umeroff2017@yandex.ru.

Davydov D.M. – Postgraduate, Department of MPMN, SSTU. E-mail: davidovd77@mail.ru.

For citation: *Amosov A.P., Latukhin E.I., Umerov E.R., Davydov D.M.* Investigation of possibility of fabrication of long-length samples of Ti_3AlC_2–Al MAX-cermet by the SHS method with spontaneous infiltration by aluminum melt. *Izvestiya Vuzov. Poroshkovaya Metallurgiya i Funktsional'nye Pokrytiya (Powder Metallurgy and Functional Coatings)*. 2022. Vol. 16. No. 3. P. 24–36 (In Russ.). DOI: dx.doi.org/10.17073/1997-308X-2022-3-24-36.

Исследование возможности получения длинномерных образцов MAX-кермета Ti_3AlC_2–Al методом СВС с самопроизвольной инфильтрацией расплавом алюминия

А.П. Амосов, Е.И. Латухин, Э.Р. Умеров, Д.М. Давыдов

Самарский государственный технический университет (СамГТУ)

Статья поступила в редакцию 28.02.2022 г., доработана 18.07.2022 г., подписана в печать 21.07.2022 г.

Аннотация: Рассмотрены особенности совмещения процесса самораспространяющегося высокотемпературного синтеза (СВС) пористого каркаса MAX-фазы Ti_3AlC_2 с инфильтрацией расплавом алюминия в самопроизвольном режиме с целью

получения образцов керамико-металлического композита (MAX-кермета) Ti_3AlC_2–Al увеличенных размеров в воздушной атмосфере. Разработана новая схема изготовления длинномерных образцов СВС-керметов из шихты насыпной плотности с самопроизвольной инфильтрацией расплавом в спутном направлении с движением волны горения, при которой можно регулировать временну́ю паузу между моментом окончания синтеза Ti_3AlC_2 и началом процесса самопроизвольного заполнения пор расплавом алюминия. По данной технологии был синтезирован СВС-каркас Ti_3AlC_2 общей длиной 250 мм и диаметром 22–24 мм, в котором глубина инфильтрации чистым алюминием составила около 110 мм, а пропитка сплавом Al–12%Si – 130 мм. Приведены сравнительные данные по плотности, микроструктуре и фазовому составу на разных участках по длине образцов полученных СВС-керметов. Установлено, что инфильтрация чистым алюминием разрушает MAX-фазу Ti_3AlC_2, превращая ее в смесь фаз TiC + $TiAl_3$ в СВС-кермете, а добавка 12 % Si к Al-расплаву способствует некоторому сохранению Ti_3AlC_2 в кермете. Вместо образцов MAX-керметов с целевым составом Ti_3AlC_2–Al и Ti_3AlC_2–(Al–12%Si) получены длинномерные образцы СВС-керметов с другим реальным фазовым составом: TiC–$TiAl_3$–Al и TiC–Ti_3AlC_2–$TiAl_3$–(Al–12%Si) соответственно, в которых MAX-фаза Ti_3AlC_2 или практически отсутствует, или имеется в небольших количествах. Средние значения твердости СВС-керметов TiC–$TiAl_3$–Al и TiC–Ti_3AlC_2–$TiAl_3$–(Al–12%Si) составили *HB* = 640 и 740 МПа, плотность ρ = 2,88÷3,16 и 3,03÷3,13 г/см^3, а остаточная пористость *П* = 17,0÷24,6 и 17,6÷20,3 % соответственно.

Ключевые слова: самораспространяющийся высокотемпературный синтез (СВС), MAX-фаза, Ti_3AlC_2, самопроизвольная инфильтрация, MAX-кермет, Ti_3AlC_2–Al, микроструктура, фазовый состав, физико-механические свойства.

Амосов А.П. – докт. физ.-мат. наук, проф., зав. кафедрой металловедения, порошковой металлургии, наноматериалов (МПМН), СамГТУ (443100, г. Самара, ул. Молодогвардейская, 244). E-mail: egundor@yandex.ru.

Латухин Е.И. – канд. техн. наук, доцент кафедры МПМН, СамГТУ. E-mail: evgelat@yandex.ru.

Умеров Э.Р. – аспирант кафедры МПМН, СамГТУ. E-mail: umeroff2017@yandex.ru.

Давыдов Д.М. – аспирант кафедры МПМН, СамГТУ. E-mail: davidovd77@mail.ru.

Для цитирования: *Амосов А.П., Латухин Е.И., Умеров Э.Р., Давыдов Д.М.* Исследование возможности получения длинномерных образцов MAX-кермета Ti_3AlC_2–Al методом СВС с самопроизвольной инфильтрацией расплавом алюминия. *Известия вузов. Порошковая металлургия и функциональные покрытия*. 2022. Т. 16. No. 3. С. 24–36. DOI: dx.doi.org/10.17073/1997-308X-2022-3-24-36.

Introduction

In the past 25 years MAX phases including titanium aluminum carbide (Ti_3AlC_2) have been attracting much attention. Their unique properties combine the advantages of ceramic and metallic materials as demonstrated in [1, 2]. So far more than 150 different MAX phases have been synthesized and studied. MAX phases have not yet been applied commercially [2], however, despite their large number and attractive properties arising from their unique layered crystal structure, low weight, excellent oxidation resistance up to 1400 °C in aggressive environment, high resistance to mechanical damage, thermal shock and radiation, crack bridging, and good machinability by both cutting and electrical erosion. One notable exception is chromium aluminum carbide (Cr_2AlC), which is used in sliding current collectors instead of carbon current collectors on high-speed trains in China.

The main limiting factor in transferring MAX phases to the market is the absence of suitable methods for producing high-purity MAX phases in large quantities at an acceptable cost [2]. In this respect, one of the most promising methods could be self-propagating high-temperature synthesis (SHS). This is characterized by simplicity, short synthesis time, low energy consumption, flexibility and possibility of increasing the production scale, as well as an acceptable cost of synthesis products [2—4]. The main drawback of this technology is the high content of side phases and impurities (carbides, intermetallic compounds, and residues of unreacted reagents) in the synthesized MAX phases. With this in mind, the further development and improvement of the SHS method as a process foundation for the creation of economically justified facilities, i.e. the commercialization of MAX phases and new ceramic and composite materials and products based on them is of undoubted interest.

This work considers the application of the SHS method for the synthesis of the porous framework of the Ti_3AlC_2 MAX phase followed by spontaneous infiltration with aluminum melt to obtain a ceramic-metal composite (MAX cermet) Ti_3AlC_2—Al of increased

dimensions in air atmosphere. (MAX phase composites with metals are referred to as «MAXMETs» or «MAX-MMCs» in English-language literature [5—7], but in Russian-language sources we propose the name «MAX cermet», given that MAX phases refer to new ceramics [8, 9]). Compound Ti_3AlC_2 is one of the most popular MAX phases and is characterized by low weight, good crack resistance, ductility and oxidation resistance at high temperatures. This makes its use very attractive in composite materials with metals, i.e. in MAX cermets, in aerospace engineering [6, 9, 10]. Metal Al-bonded Ti_2AlC and Ti_3AlC_2 titanium aluminum carbide-based cermets have high values of the yield strength, impact strength and mechanical energy dissipation [11, 12]. They are considered much more effective than aluminum and other metals for the protection of spacecraft against high velocity impacts from micrometeorites and orbital debris.

Both solid-phase powder metallurgy and liquid-phase infiltration methods can be used to manufacture framework MAX cermets [13]. For example, Ti_3AlC_2—Al cermets were fabricated from pure Al powders and 40 vol.% Ti_3AlC_2 by hot isostatic pressing [12]. It was found that nanocrystalline agglomerates of Ti_3AlC_2, distributed evenly in the Al matrix, form a solid continuous framework. Evaluation of the mechanical properties of cermets in the temperature range of 20—500 °C by conducting compression tests at a constant deformation rate showed that the yield strength of cermet was about 2 times higher than that of aluminum matrix in the temperature range under study. New cermet Ti_3AlC_2—Al_3Ti—Al was fabricated by hot pressing of Ti_3AlC_2 and pure Al powders [14]. Strong interfacial bonding occurred due to the formation of the Al_3Ti phase between Ti_3AlC_2 and Al. The bending strength, compressive strength, compressive yield strength and Vickers hardness number of cermet reinforced with 30 vol.% Ti_3AlC_2 were measured. These were 398 MPa, 404 MPa, 359 MPa, and 1.91 GPa, respectively.

Methods of infiltration (impregnation) of a porous ceramic framework with metal melt are one of the most common technologies used in the production of cermets. They allow products of complex shape with low residual porosity and low cost to be obtained, when compared to the methods of powder metallurgy. This is due to the possibility of using relatively inexpensive foundry equipment [13].

Methods using spontaneous infiltration without the application of external pressure are the simplest and therefore most attractive. However, the spontaneous impregnation of a ceramic framework is possible only when the metal melt wets the ceramics, i.e., when the contact angle is $\theta < 90°$. The smaller the value of θ, the easier infiltration takes place.

The wetting angle depends on the nature of the ceramic and metal phases, the temperature and duration of their contact, and the gas environment. MAX phases of titanium Ti_3SiC_2, Ti_3AlC_2 and Ti_2AlC, similar to titanium carbide (TiC), are not wetted by pure liquid aluminum ($\theta > 90°$) at temperatures below 900 °C. This is due to the presence of an oxide film and contamination on the MAX phase surface. However, at higher temperatures and over time, the contact angle decreases to values of $\theta < 90°$, i.e., wetting begins. This is explained by the fact that wetting is determined by chemical reactions at the interface and their influence on the destruction of the oxide film on the surface.

As noted in [15], little information is available at the present time on the use of the infiltration method to produce MAX cermets with an aluminum metal phase. The same work demonstrates that MAX cermet systems of the titanium—aluminum aluminum carbide system, namely Ti_3AlC_2—2024Al with a framework structure, can be produced successfully from porous Ti_3AlC_2 blanks by infiltration without pressure by aluminum alloy melt 2024Al at t = 930 °C [15]. Ti_3AlC_2 blanks with porosity of 48, 41 and 35 % were previously obtained by vacuum sintering at t = 1450 °C from Ti, Al and TiC powders. During infiltration lasting 180 min, the reaction between Ti atoms deintercalated from porous Ti_3AlC_2 and Al atoms from liquid 2024Al in pores formed intermetallic compound Al_3Ti to the amount of 15 to 28 vol.% with a Ti_3AlC_2 framework porosity from 35 to 48 % respectively. At room temperature, cermet formed from the Ti_3AlC_2 framework with a porosity of 41 %, composition, vol.% of 52Ti_3AlC_2—19Al_3Ti—29Al, and relative density of 95.41 %, showed the best set of mechanical properties: flexural strength of 510 MPa, compressive strength of 729 MPa and compressive strain of 5.49 %.

The authors of [10] obtained porous frameworks of the MAX phase of Ti_3AlC_2 by SHS after heating in a microwave oven. Then after cooling they were transferred to a metal mold, heated to 750 °C and impreg-

nated for 1—2 minutes with aluminum cast alloy melt Al—13%S at 720—740 °C by casting under the pressure of 90 MPa. The quantitative *X*-ray Diffraction (XRD) phase analysis showed that SHS produced a ceramic framework of two major phases Ti_2AlC and Ti_3AlC_2, as well as a small amount of TiC, wt.%: Ti_2AlC — 66.54, Ti_3AlC_2 — 30.32, and TiC — 3.14. After infiltration under pressure by the Al—13%Si melt, the MAX cermet was formed with a volume ratio of the ceramic and metal phases of about 50 : 50 and a relative density of at least 95 %. Due to the short duration and low temperature of the infiltration process side intermetallic phase Al_3Ti is not formed. The hardness of the cermet increased by a factor of 4 relative to the soft matrix (Al—13%Si), 588 HV versus 160 HV, and the wear rate was less than half that of the Al—13%Si alloy.

In the above examples using infiltration, the MAX cermets of the Ti_3AlC_2—Al system were produced using 2-stage technologies with long external heating at high temperatures, i.e., at sophisticated equipment and with high energy consumption. Single-stage energy-saving process of force SHS compaction allows the thermal effect of SHS to be used for both the synthesis of the Ti_3AlC_2 MAX phase framework and simultaneous melting of aluminum, and its rapid forced infiltration under the pressing pressure into the synthesized framework in obtaining a compact Ti_2AlC—Al MAX cermet [16].

However, the simplification of this approach by refusing to use sophisticated pressing equipment, while using the SHS process both for the synthesis of the MAX phase framework and for the simultaneous melting of the metal and its spontaneous infiltration into the framework without applying excessive pressure results in a non-uniform composition of MAX cermet with partially filled pores in the framework [17]. This can be explained by the fact that only a small amount of metal can be melted due to the SHS reaction heat. This is insufficient for complete filling of pores in the MAX phase framework by spontaneous infiltration. The SHS heat consumption for heating and melting of aluminum leads to rapid cooling of the SHS framework, making it difficult to wet it with a metal melt and complicating the flow of spontaneous infiltration.

In this regard, the authors of this paper propose a new simple method of obtaining cermets based on the use of the porous ceramic framework SHS process, followed by spontaneous infiltration with a metal melt prepared in advance by heating from an external source. This allows the requisite amount to be used, in order to completely impregnate the ceramic framework of sufficiently large dimensions without applying excess pressure. This was successfully demonstrated by the example of obtaining the TiC—Al cermet [13, 17]. This technology was used to produce MAX cermets Ti_2AlC—Al and Ti_3AlC_2—Al in the form of small samples. They were obtained by air burning of briquettes pressed at 25 MPa (23 mm in diameter and 10 mm high) of the corresponding mixtures of titanium, aluminum and graphite powders with an average delay time of 8 s after completion of burning, and the subsequent immersion of the synthesized hot MAX phase framework into the aluminum melt or its pouring with Al melt for spontaneous infiltration of the SHS framework [18, 19].

The study of the possibility to produce samples of MAX cermets of increased sizes compared to those obtained earlier by the new method is of undoubted interest. This would include long samples whose length is several times greater than the diameter of their cross-section. Long samples of the TiC—Al cermet in the form of cylindrical rods up to 130 mm long were obtained from a composite charge blank of 13 separately pressed charge briquettes (10 mm high and 23 mm in diameter), tightly pressed to each other with ends touching. It is technologically difficult to produce a one-piece pressed charge blank of a significant length with uniform charge density distribution [13].

The purpose of this work was to investigate the possibility of applying a new simpler flowchart to use of the SHS process with spontaneous infiltration with aluminum melt, in order to obtain long Ti_3AlC_2—Al MAX cermet samples from a bulk density charge in air atmosphere, taking into account the features of formation of the Ti_3AlC_2 MAX phase.

Research materials and methods

Previous studies have shown that the structure and fractional composition of initial powder reagents significantly affect the Ti_3AlC_2 content in the SHS framework, as well as its structure after synthesis in air atmosphere [20]. Therefore, in the present work, the grades of titanium TPP-7 (d ~ 300 μm, purity 97.9 %), alumi-

num PA-4 (~50 μm, 99 %) and graphite S-2 (~15 μm, 98.5 %) were selected as the main powder reagents which allow the SHS framework to by synthesized in the air with the highest Ti_3AlC_2 content without significant macrostructural defects, cracks, large pores, etc. Aluminum melt with a temperature of 900 °C for the SHS framework infiltration was prepared from A85 grade aluminum (purity not less than 99.7 %) in a Graficarbo electric furnace (Italy). The Al—12%Si alloy was obtained by dissolving silicon in aluminum melt.

Pre-dried initial powders were mixed in a ball mill for 20 min. The powder charge mixture of 3Ti + Al + + 2C was poured into a cylindrical single-layer paper cup 22 mm in diameter and 250 mm long without additional compaction. The SHS reaction was carried out by burning the charge in bulk inside a paper cup placed horizontally on a sand base. The burning of the charge was initiated with a nichrome electric glow spiral by means of ignition charge of TPP-7 grade titanium and P701 carbon black powders with a mass ratio of 4 : 1.

The ignition charge supplied a thermal impulse to the charge at a distance of 40 mm from the place of contact of the charge blank with the Al melt bath. Initiation of the ignition charge and pouring of the melt into a recess prepared in the sand were carried out simultaneously. SHS reaction startup from the contact of the charge with the hot melt did not occur. Taking into account the experimentally determined velocity of the burning wave (~6 mm/s), this distance (40 mm) enabled a pause of 5—6 s, sufficient for completion of secondary structure formation in the burned SHS framework and synthesis of Ti_3AlC_2.

The burning velocity was determined by video filming (at a frequency of 60 frames per second) of the burning process of a 200 mm long charge blank. The video image was analyzed to determine the length of the burned SHS framework to the time of its burnout ratio. The experiment flowchart is shown in Figure 1. Its data shows that the SHS initiation site can be shifted along the charge blank by adjusting the pause between the passage of the burning wave and the infiltration front. The ability to adjust the pause is necessary to provide a certain time delay for charge mixtures of different compositions and press densities, which can have significantly different burning rates.

The SHS cermet obtained was divided into equal cylinders 20 mm long, in order to study the microstruc-

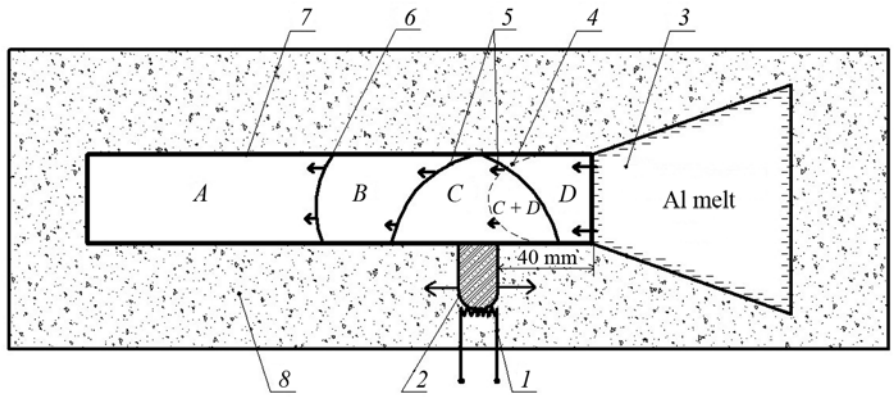

Fig. 1. Ti_3AlC_2–Al SHS cermet production diagram (top view)

1 – filament, ***2*** – igniter, ***3*** – Al melt at t = 900 °C, ***4*** – melt infiltration front, ***5*** – conditional front of Ti_3AlC_2 secondary structure formation, ***6*** – burning front, ***7*** – SHS charge, ***8*** – sand

A – area of 3Ti–1Al–2C initial reagents; ***B*** – area of TiC_x + $TiAl_x$ primary structure formation; ***C*** – area of Ti_3AlC_2 secondary structure formation; ***D*** – area of Al infiltration; (***C*** + ***D***) – Ti_3AlC_2 area containing infiltrated aluminum in pores

Рис. 1. Схема получения СВС-кермета Ti_3AlC_2–Al (вид сверху)

1 – спираль накаливания, ***2*** – запал, ***3*** – Al-расплав с t = 900 °C, ***4*** – фронт инфильтрации расплавом,

5 – условный фронт вторичного структурообразования Ti_3AlC_2, ***6*** – фронт горения, ***7*** – шихта СВС, ***8*** – песок

A – область исходных реагентов 3Ti–1Al–2C; ***B*** – область первичного структурообразования TiC_x + $TiAl_x$;

C – область вторичного структурообразования Ti_3AlC_2; ***D*** – область инфильтрации Al;

(***C*** + ***D***) – область Ti_3AlC_2, содержащая инфильтрированный алюминий в порах

ture and phase composition at a certain distance from the beginning of the sample contacting the molten metal. The microstructure of the samples was studied using a scanning electron microscope (SEM) JSM-6390A (JEOL Ltd., Japan). Phase composition was determined by means of *X*-ray diffractometer ARL X'trA-138 (Thermo Scientific, Switzerland) using CuK_α radiation with continuous scanning in the interval of angles $2\theta = 5°\div80°$ with the speed of 2 deg/min. Sample density was evaluated by hydrostatic weighing in water. Hardness (*HB*) was measured using the Brinell method by indentation of a steel ball (d = 5 mm) with a load of 2,5 kN, since a relatively large ball allows averaging of structural heterogeneities (small pores).

Results and discussion

Preliminary experiments on the use of SHS to produce MAX cermets by initiating burning at the place of contact of the charge with the melt showed the impossibility of preserving the MAX phase in the final composite. The introduction of the cooler metal melt into the hot SHS framework resulted in its rapid cooling and inhibiting high-temperature reactions of formation of titanium aluminum carbide MAX phases. This occurred in the afterburning zone for at least 4—6 s after the burning wave passed [21]. Therefore, conditions for the formation of the MAX phase in the afterburning zone can be ensured by adjusting the time pause between the passage of the burning front and the infiltration front. On the other hand, too long a pause can lead to significant cooling of the framework. This can ultimately make it impossible for it to be wetted and spontaneously infiltrated by the aluminum melt or substantially limits the infiltration depth.

When SHS is initiated at a distance of 40 mm from the melt bath, 2 burning fronts are created simultaneously, moving in opposite directions of the charge blank. The first burning front moves towards the melt bath, and after traveling a distance of 40 mm, reaches the beginning of the charge blank at the point of contact with the melt. The already red-hot SHS framework melted the oxide film on the surface of the melt bath. At a burning wave velocity of 6 mm/sm it took about 6—7 s to overcome this distance (40 mm). At this point, the aluminum melt began to infiltrate into the SHS framework, in which the second burning front continued to move in the opposite direction from the melt bath. Thus, a time pause (6—8 s) between the second (main) burning front and the infiltration front was provided.

The appearance of the SHS cermet obtained based on Ti_3AlC_2 is shown in Figure 2. It can be seen that a part of the burnt fuse remained in the upper part of the sample on the left, which at a distance of ~40 mm from the beginning of the sample initiated the SHS reaction, triggering 2 burning waves in different directions. Zone *1* with a length of about 40 mm on the sample was formed first and performed a process function in this circuit. Given that the pause between the end of burning in this zone *1* and the beginning of infiltration was less than 6 s, the function of this section of the SHS framework was reduced, in order to provide a pause between the second burning wave (moving to the right side of the sample) and the infiltration front. The first section of the 100 mm long sample has a larger diameter of 24 mm. It is silver in color, and has a slightly deformed surface, indicating the presence of aluminum in the framework pores. An increase in diameter of the impregnated part of the framework may be due to the Rehbinder effect, as well as features of the high-temperature chemical interaction of the Al melt/silumin with the 3Ti—Al—2C SHS system. The right section measuring 60—70 mm is distinguished by a white plaque and a smaller diameter (~20 mm).

In order to study the completeness and depth of the aluminum melt infiltration into the SHS framework, the MAX cermet samples obtained were cut into 10 approximately equal cylindrical disks with an average thickness of ~14 mm for the Ti_3AlC_2—Al sample with target composition, with an initial length of 160 mm and ~15 mm for the Ti_3AlC_2—(Al—12Si) sample with l = 170 mm. The loss of 20 mm of the total length was due to material consumption when cutting sample disks with a cutting wheel about 2 mm thick. Thus, 9 cross-sections were obtained in succession along the length of MAX cermet samples. The appearance allows the quality of impregnation to be assessed visually.

Figure 3, *a* shows that the first 4 cross-sections practically have no pores or voids, while possessing a homogeneous metallic luster, indicating good wetting of ceramics by metal in this section up to ~60 mm long. In cross-sections *5*—*8*, an increasing number of dark pores can be noted: from few single pores in cross-section *5*;

to the predominance of dark pores over silver pores in cross-section *8*. The images of cross-sections *8* and *9* are characteristic of an unimpregnated SHS framework of Ti_3AlC_2, so conventionally the distance at which cross-section *7* with obvious signs of impregnation was obtained can be taken as the depth of impregnation, i.e., about 110±10 mm.

Figure 3, *b* shows that starting from the first section, small pores are observed from one to several pieces, clearly distinguishable on the homogeneous silver surface of the cut. Cross-sections *4—7* show pore clusters in specific areas of the cross-section. Cross-sections *8* and *9* have the appearance of an unimpregnated framework, with no obvious traces of the presence of significant amounts of metal. Taking into account the average length of each individual sample disk (15 mm) and loss per cut (2 mm), impregnation in this case was completed on the 8th sample disk, and its depth was about 130±10 mm. Increase of the infiltration depth up to ~130 mm may be explained by increased fluidity of the melt and its wetting of the framework in the presence of silicon in the melt.

Figure 4 shows that the density distribution curves of SHS cermets of Ti_3AlC_2—Al and Ti_3AlC_2—(Al—12Si) target compositions have a similar nature and they decrease smoothly along the length of the samples from 3.0—3.2 to 2.0 g/cm^3. At the same time, the density of Al—12Si-based cermet is slightly higher. This may indicate a more complete impregnation with silumin melt, when compared to pure aluminum.

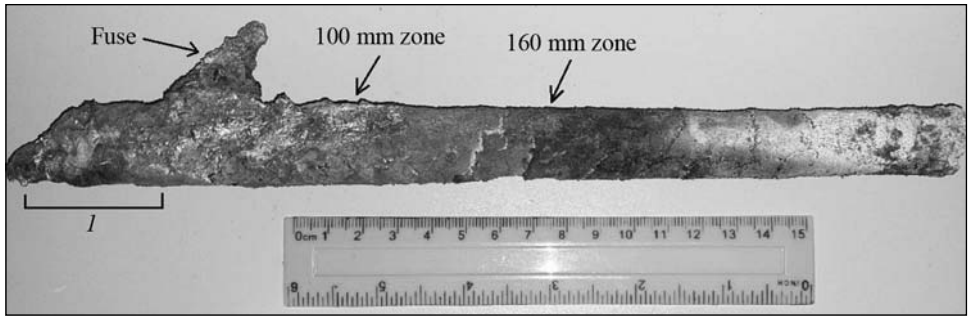

Fig. 2. Cermet sample after SHS

1 – zone from 0 to 40 mm, in which the pause between the SHS process and melt infiltration was less than 6 s

Рис. 2. Образец кермета после СВС

1 – зона от 0 до 40 мм, в которой пауза между процессом СВС и инфильтрацией расплава была менее 6 с

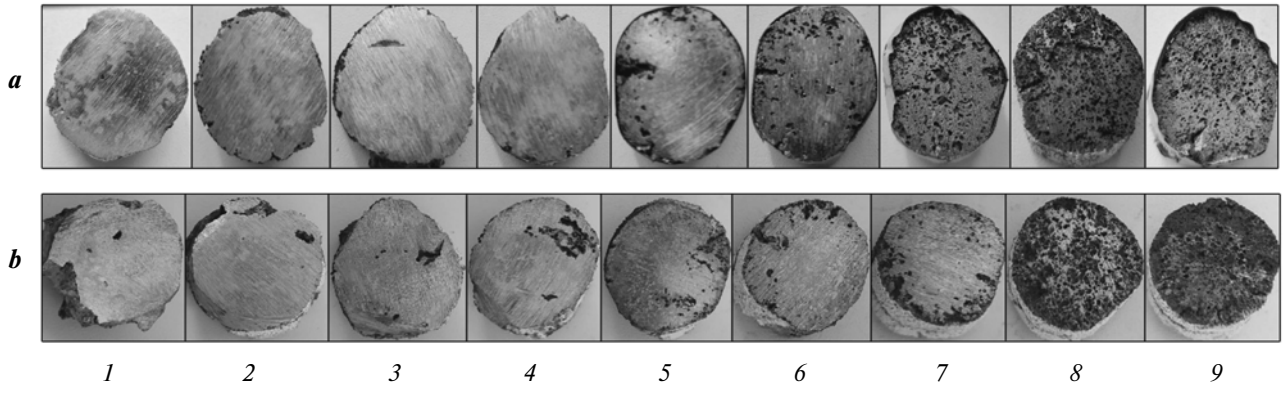

Fig. 3. Successive cross sections of long-length SHS cermets with target compositions Ti_3AlC_2–Al (***a***) and Ti_3AlC_2–(Al–12Si) (***b***)

Рис. 3. Последовательные поперечные сечения длинномерных СВС-керметов целевых составов Ti_3AlC_2–Al (***a***) и Ti_3AlC_2–(Al–12Si) (***b***)

When examining the fracture microstructure, the laminar phase of Ti_3AlC_2 is observed predominantly in the final part of the sample. Traces have not been detected in the cross section obtained in the initial part of the sample at a distance of 40 mm. Photographs of the fracture microstructure at distances of 100 and 160 mm from the beginning of the sample at the point of contact with the melt bath are shown in Figure 5.

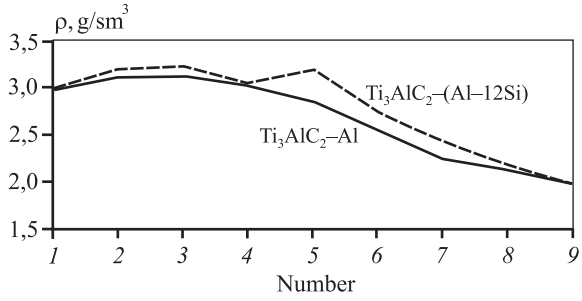

Fig. 4. Density distribution over MAX cermet disk samples

Рис. 4. Распределение плотности по образцам-дискам MAX-керметов

Figure 5, *a* shows equiaxial particles of titanium carbide and a small number of multidirectional plates similar in appearance to Ti_3AlC_2 plates. The latter are predominantly observed in Figure 5, *b* with a small number of rounded TiC particles. It is important to note that at a distance of 160 mm, traces of impregnation are almost absent. The pores in the framework remained unfilled with metal which could lead to a large amount of the observed phase of Ti_3AlC_2. The *X*-ray diffraction patterns of fractures of samples shown in Figure 5 are shown in Figure 6.

According to the height of peaks in Figure 6, *a*, it can be concluded that the main phases in the cermet at a distance of 100 mm are Al and TiC, while Ti_3AlC_2 and $TiAl_3$ are present in a much smaller amount. According to Figure 6, *b*, in a fracture, at a distance of 160 mm, there are no traces of aluminum. Only refractory phases of the TiC and Ti_3AlC_2 framework are observed. According to the results presented, it can be

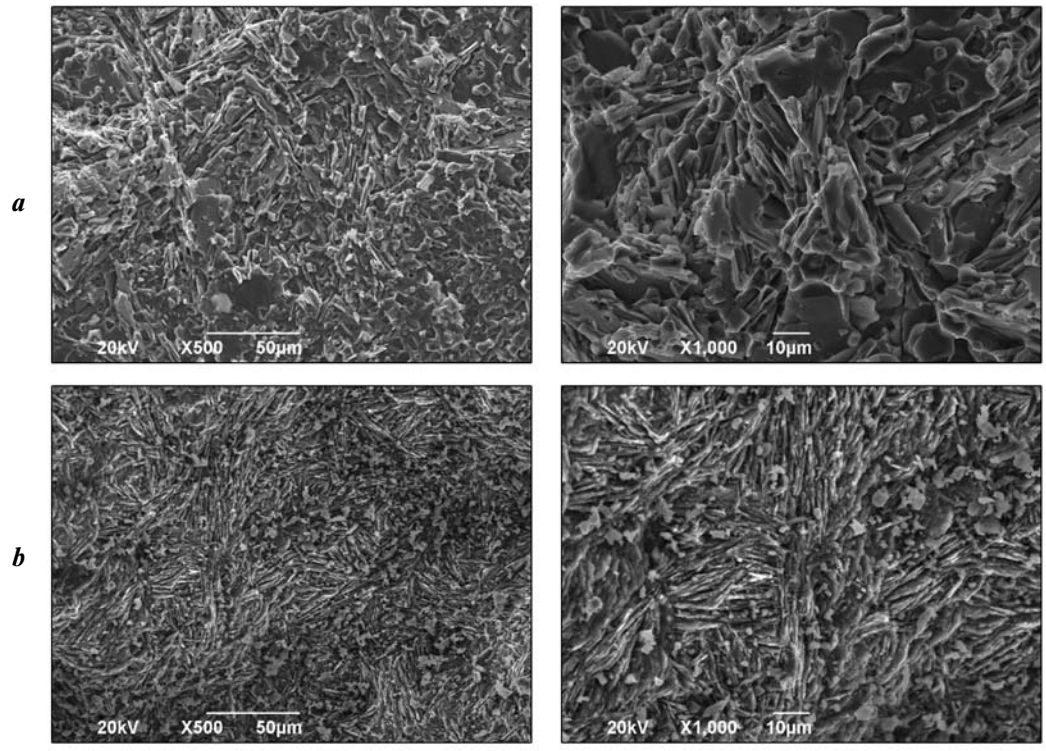

Fig. 5. Fracture microstructure of the sample with target composition Ti_3AlC_2–Al at a distance of 100 mm (***a***) and 160 mm (***b***) from the sample origin

Рис. 5. Микроструктура изломов образца целевого состава Ti_3AlC_2–Al на расстоянии 100 мм (***a***) и 160 мм (***b***) от начала образца

concluded that the aluminum melt impregnating the SHS framework generally destroys the MAX phase of Ti_3AlC_2. This is consistent with the previously obtained data [19]. Therefore, it is not sufficient only to ensure the completion of structure formation of Ti_3AlC_2. The issue of chemical resistance of Ti_3AlC_2 to the incoming aluminum melt superheated during infiltration as a result of heat exchange with the hot SHS framework also needs to be considered.

Study of the microstructure of the MAX cermet sample obtained by infiltration with the Al—12%Si silumin melt was carried out on transverse fractures of the sample at distances of 40, 80, and 120 mm from the melt bath (Figure 7). At all sites a significant number of Ti_3AlC_2 plates is observed. It is important to note that a significant part is in the metal matrix or tightly in contact with it, and the silumin melt has impregnated deeper than pure aluminum.

Fracture diffraction patterns of these sections, shown in Figure 8, revealed the following phase composition: Al, TiC, Ti_3AlC_2, $TiAl_2$, and $TiAl_3$ for sample sections at both 40 mm and 80 mm from the melt bath. Consequently, the addition of 12 % Si to Al contributes to the Ti_3AlC_2 content increase in the impregnated part of the framework. In addition, systematic peaks of $TiAl_3$ and $TiAl_2$ compounds have been detected, and a shift of Al peaks was noted (see Figure 8, *b*). This is due to the presence of silicon in the Al—12%S melt.

Thus, the SHS cermet with the Ti_3AlC_2—Al target composition, obtained by infiltration of pure aluminum, has a different real phase composition: TiC—$TiAl_3$—Al. At the same time, the silumin-based SHS cermet Ti_3AlC_2—(Al—12Si) at the 0—40 mm section, is also another real composition of TiC—$TiAl_3$—(Al—12Si). At the 40—120 mm section, the composition is TiC—Ti_3AlC_2—$TiAl_3$—(Al—12Si). In general, aluminum actively destroys Ti_3AlC_2, and the addition of 12 % Si to it contributes to the preservation of Ti_3AlC_2 in obtaining long-length SHS cermet by spontaneous infiltration of the metal melt. This is probably due to less deinterculation of Al from the MAX phase of Ti_3AlC_2 into the Al—12%Si melt compared to the pure aluminum melt.

The results of hardness studies in cross sections of

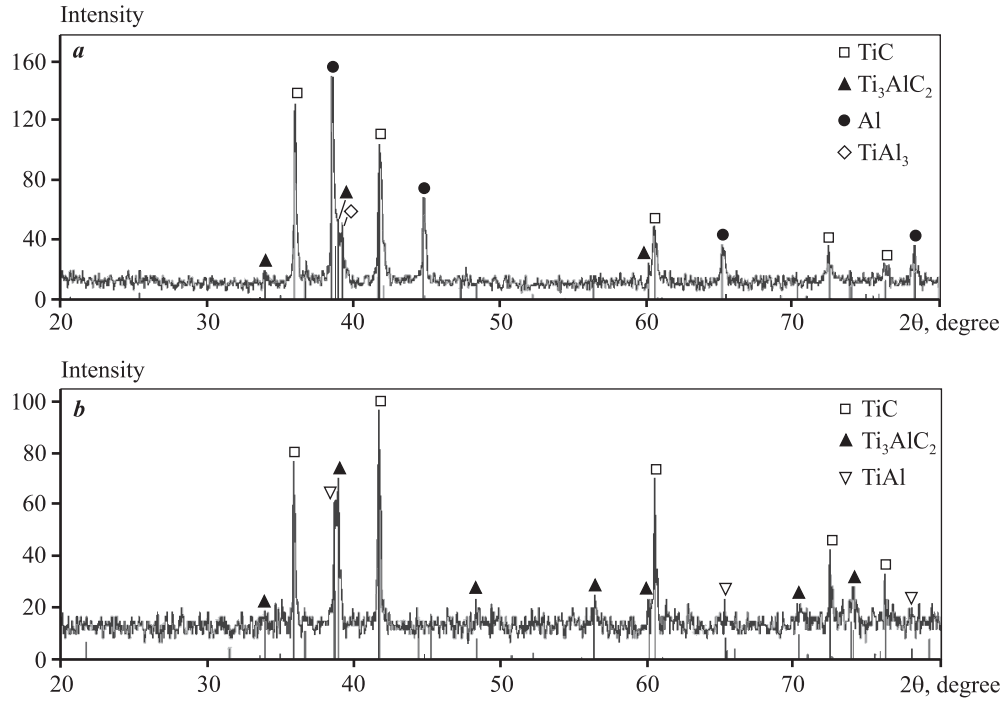

Fig. 6. Fracture XRD patterns of the sample with target composition Ti_3AlC_2–Al at a distance of 100 mm (***a***) and 160 mm (***b***) from the sample origin

Рис. 6. Дифрактограммы изломов образца целевого состава Ti_3AlC_2–Al на расстоянии 100 мм (***a***) и 160 мм (***b***) от начала образца

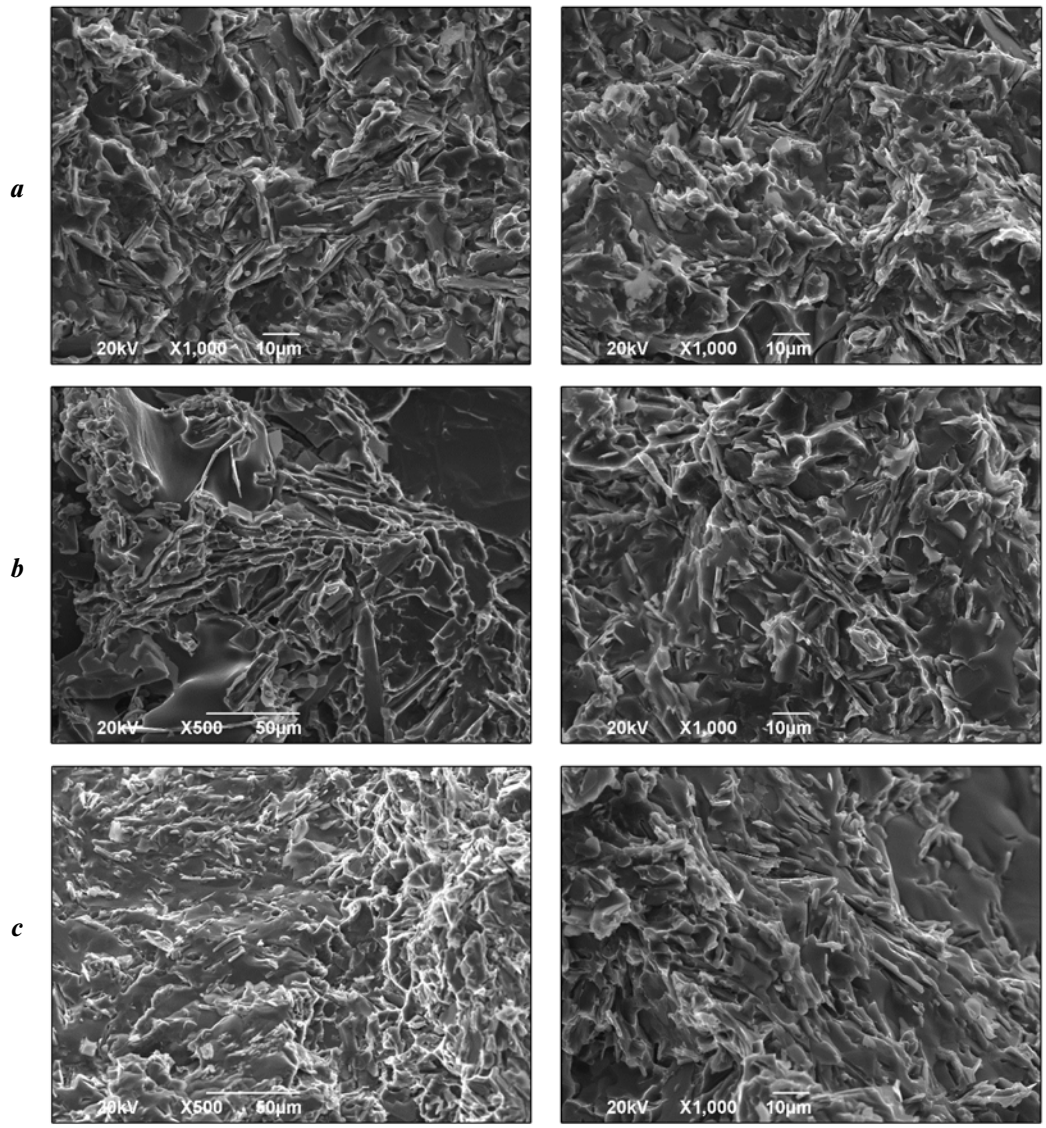

Fig. 7. Fracture microstructure of the sample with target composition Ti_3AlC_2–(Al–12Si) at a distance of 40 mm (***a***), 80 mm (***b***) and 120 mm (***c***) from melt bath

Рис. 7. Микроструктура излома образца целевого состава Ti_3AlC_2–(Al–12Si) на расстоянии 40 мм (***a***), 80 мм (***b***) и 120 мм (***c***) от ванны расплава

the SHS cermets obtained are shown in Figure 9. This shows 3 prints with diameters of 2.63, 2.7 and 2.22 mm after indentation of a steel ball with ∅ 5 mm. After processing the results (prints) of at least 10 tests, the average Brinell hardness value for cermets of the Ti_3AlC_2—Al target composition (in the 100 mm zone) was approximately 640±180 MPa. For Ti_3AlC_2—(Al—12%Si) (in the 80 mm zone) it was 740±310 MPa, which according to the international standard of the hardness value conversion can be estimated conditionally by the values of the strength limit of ~220 and ~250 MPa respectively [22].

The greater hardness of SHS silumin-based cermets can be explained by higher mechanical properties of silumin (about 500 MPa) compared to pure aluminum (200—300 MPa). The significant dispersion of hardness data and relatively low strength of composites can be associated with significant residual porosity, as well as uneven structure across the cross section of the composite as shown in Figure 3. The density of

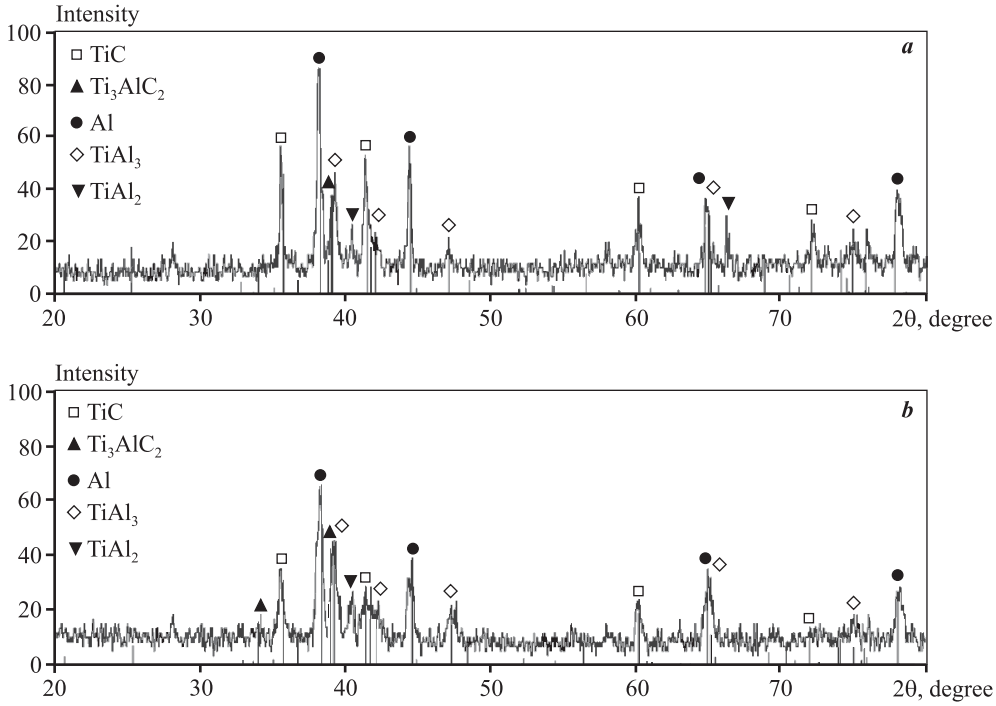

Fig. 8. Fracture XRD patterns of the sample with target composition Ti_3AlC_2–(Al–12Si) at a distance of 40 mm (***a***) and 80 mm (***b***) from melt bath

Рис. 8. Дифрактограммы изломов образца целевого состава Ti_3AlC_2–(Al–12Si) на расстоянии 40 мм (***a***) и 80 мм (***b***) от ванны расплава

Ti_3AlC_2—Al cermets was ρ = 2.88÷3.16 g/cm^3, which, taking into account the phase composition, corresponds to the residual porosity of P = 17.0÷24.6 %. For Ti_3AlC_2—(Al—12%Si) cermets the values are ρ = 3.03÷3.13 g/cm^3 and P = 17.6÷20.3 %. Consequently, the addition of 12 % Si to Al leads to an insignificant decrease in the sample density dispersion and, as a consequence, the residual porosity, contributing to a more uniform distribution of the metal over the SHS framework during infiltration.

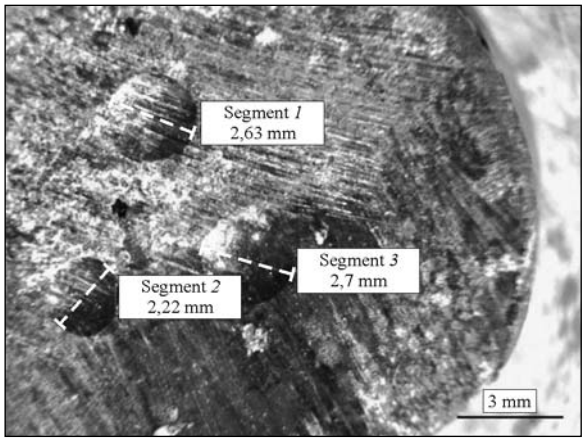

Fig. 9. Indents on the section of SHS cermet with target composition Ti_3AlC_2–(Al–12Si) after hardness test

Рис. 9. Отпечатки индентора на сечении СВС-кермета целевого состава Ti_3AlC_2–(Al–12Si) после испытания на твердость

If we focus on possible applications of MAX phases [2], the developed SHS cermets can be used as light wear-resistant materials. The presence of porosity makes them lighter, and as electrodes for application of wear-resistant coatings. In order to further increase the completeness and depth of infiltration, the temperatures of the SHS framework and aluminum melt need to be increased, while at the same time providing measures to reduce the chemical interaction between them by searching for alloying components.

Conclusion

This study investigated the possibility of applying a new circuit of the previously proposed method, in order

to obtain long-length samples of MAX cermets on an aluminum matrix basis using the SHS process. In this case the synthesis of the Ti_3AlC_2 MAX phase porous framework was carried out by means of the bulk density charge combustion in air atmosphere, followed by spontaneous impregnation with aluminum melt. This provided the pause necessary for the formation of the MAX phase between the passage of the burning and impregnation fronts.

However, instead of MAX samples with the Ti_3AlC_2—Al and Ti_3AlC_2—(Al—12Si), target compositions, the cylindrical samples of SHS cermets with increased dimensions (length up to 110—130 mm and mean diameter of 24 mm) were produced with different real compositions: TiC—$TiAl_3$—Al and TiC—Ti_3AlC_2—$TiAl_3$—(Al—12Si), respectively. In these samples the MAX phase of Ti_3AlC_2 is either practically absent or present in small amounts. This result can be explained by the fact that active destruction occurs during spontaneous infiltration of the Ti_3AlC_2 MAX phase synthesized framework by pure aluminum melt. The addition of 12 % Si to the Al melt promotes an increase in the Ti_3AlC_2 content in the SHS cermet obtained, as well as increasing the total depth of infiltration from ~110 to ~130 mm.

The average hardness value of TiC—$TiAl_3$—Al and TiC—Ti_3AlC_2—$TiAl_3$—(Al—12Si) SHS cermets is *HB* = 640 and 740 MPa, which corresponds conventionally to the ultimate tensile strength of the obtained materials of about ~220 and 250 MPa, respectively. In the case of the TiC—$TiAl_3$—Al sample, the density is 2.88—3.16 g/cm^3, and the residual porosity is 17.0—24.6 %, and for the TiC—Ti_3AlC_2—$TiAl_3$—(Al—12Si) cermet these parameters are equal to $\rho = 3.03 \div 3.13$ g/cm^3, $P = 17.6 \div 20.3$ %.

Acknowledgments: *The reported study was funded by the RFBR as part of Scientific Project № 20-08-00435.*

Исследование выполнено при финансовой поддержке РФФИ в рамках научного проекта № 20-08-00435.

References

1. *Barsoum M.W.* MAX phases: Properties of machinable ternary carbides and nitrides. Weinheim: Wiley-VCH, 2013.
2. *Gonzalez-Julian J.* Processing of MAX phases: From synthesis to applications. *J. Amer. Ceram. Soc*. 2021. Vol. 104. Iss. 2. P. 659—690. DOI: 10.1111/jace.17544.
3. *Рогачев А.С., Мукасьян А.С.* Горение для синтеза материалов. М.: Физматлит, 2012.
   Rogachev A.S., Mukasyan A.S. Combustion for material synthesis. N.Y.: CRC Press, 2014.
4. *Levashov E.A., Mukasyan A.S., Rogachev A.S., Shtansky D.V.* Self-propagating high-temperature synthesis of advanced materials and coatings. *Int. Mater. Rev*. 2016. No. 62 (4). P. 1—37. DOI: 10.1080/09506608.2016.1243291.
5. *Amini S., Barsoum M.W.* «MAXMET»s: A new class of metal matrix composites reinforced with MAX phases. *Metal Matrix Composites.* 2012. No. 1. P. 31—75.
6. *Amini Sh., Strock C.W., Burlatsky S.F., Novikov D., Furrer D.U.* MAXMET composites for turbine engine component tips: Pat. 2014/149097A2 (WO). 2014.
7. *Hu W., Huang Z., Wang Y., Li X., Zhai H., Zhou Y., Chen L.* Layered ternary MAX phases and their MX particulate derivative reinforced metal matrix composite: A review. *J. Alloys Compd*. 2021. Vol. 856. P. 157313. DOI: 10.1016/j.jallcom.2020.157313.
8. *Barsoum M.W., Brodkin D., El-Raghy T.* Layered machinable ceramics for high temperature applications. *Scripta Mater.* 1997. Vol. 35. P. 535—541. DOI: 10.1016/S1359-6462(96000418-6.
9. *Wang X.H., Zhou Y.C.* Layered machinable and electrically conductive Ti_2AlC and Ti_3AlC_2 ceramics: a review. *J. Mater. Sci. Technol.* 2010. Vol. 26. No. 5. P. 385—416. DOI: 10.1016/S1005-0302(10)60064-3.
10. *Dmitruk A., Naplocha K.* Manufacturing of Al alloy matrix composite materials reinforced with MAX phases. *Arch. Foundr. Eng.* 2018. Vol. 18. No. 2. P. 198—202. DOI: 10.24425/122528.
11. *Hanaor D.A.H., Hu L., Kan W.H., Proust G., Foley M., Karaman I., Radovic M.* Compressive performance and crack propagation in Al alloy/Ti_2AlC composites. *Mater. Sci. Eng. A*. 2016. No. 672. P. 247—256. DOI: 10.1016/j.msea.2016.06.073.
12. *Wang W.J., Gauthier-Brunet V., Bei G.P., Laplanche G., Bonneville J., Joulain A., Dubois S.* Powder metallurgy processing and compressive properties of Ti_3AlC_2/Al composites. *Mater. Sci. Eng. A*. 2011. Vol. 530(15). P. 168—173. DOI: 10.1016/j.msea.2011.09.068.
13. *Амосов А.П., Латухин Е.И., Умеров Э.Р.* Применение процессов инфильтрации и самораспространяющегося высокотемпературного синтеза для получения керметов: Обзор. *Известия вузов. Цветная металлургия.* 2021. Т. 27. No. 6. С. 52—75. DOI: 10.17073/0021-3438-2021-6-52-75.

Amosov A.P., Latukhin E.I., Umerov E.R. Applying infiltration and self-propagating high-temperature synthesis processes for manufacturing cermets. A review. *Russ. J. Non-Ferr. Met.* 2022. Vol. 63. No. 1. P. 81—100. DOI: 10.3103/S1067821222010047.

14. *Wang Y., Huang Z., Hu W., Cai L., Lei C., Yu Q., Jiao Y.* Preparation and characteristics of Ti_3AlC_2—Al_3Ti/Al composite materials synthesized from pure Al and Ti_3AlC_2 powders. *Mater. Charact.* 2021. Vol. 178. P. 111298. DOI: 10.1016/j.matchar.2021.111298.
15. *Wang H., Huang Z., Yi J.,Xue Li X., Zhang J., Wang Y., Zhuang W., Yu Q.* Microstructure and high-temperature mechanical properties of co-continuous (Ti_3AlC_2 + +Al_3Ti)/2024Al composite fabricated by pressureless infiltration. *Ceram. Int.* 2022. Vol. 48. Iss. 1. P. 1230—1237. DOI: 10.1016/j.ceramint.2021.09.208.
16. *Федотов А.Ф., Амосов А.П., Латухин Е.И., Новиков В.А.* Получение алюмокерамических каркасных композитов на основе MAX-фазы Ti_2AlC методом СВС-прессования. *Известия вузов. Цветная металлургия.* 2015. No. 6. С. 53—62. DOI: 10.17073/0021-3438-2015-6-53-62.

Fedotov A.F., Amosov A.P., Latukhin E.I., Novikov V.A. Fabrication of aluminum—ceramic skeleton composites based on the Ti_2AlC MAX phase by SHS compaction. *Russ. J. Non-Ferr. Met.* 2016. Vol. 57. No. 1. P. 33—40. DOI:10.3103/S1067821216010053.
17. *Амосов А.П., Латухин Е.И., Умеров Э.Р.* Способ получения керамико-металлических композиционных материалов: Пат. 2733524 (РФ). 2020.

Amosov A.P., Latukhin E.I., Umerov E.R. Method of obtaining ceramic-metal composite materials. Pat. 2733524 (RF). 2020 (In Russ.).
18. *Umerov E.R., Amosov A.P., Latukhin E.I., Kichaev P.E., Novikov V.A.* Fabrication of aluminum-ceramic skeleton composites based on titanium aluminide carbide using SHS process. *Int. Symp. SHS.* 2019. No. XV. P. 489—492. DOI: 10.24411/9999-014A-2019-10180.
19. *Латухин Е.И., Умеров Э.Р., Амосов А.П.* Применение горения для синтеза пористого каркаса Ti_3AlC_2 с последующей самопроизвольной инфильтрацией расплавом алюминия для получения кермета Ti_3AlC_2—Al. В Сб. докл. Междунар. науч.-техн. конф. «*Проблемы и перспективы развития двигателестроения*» (Самара, 23—25 июня 2021 г.). Самар. ун-т, 2021. Т. 2. С. 251—252.

Latukhin E.I., Umerov E.R., Amosov A.P. Combustion application for the synthesis of a porous Ti_3AlC_2 skeleton followed by spontaneous infiltration by aluminum melt to obtain Ti_3AlC_2—Al cermet. In: Sbornik dokladov Mezhdunar. nauchno-tekhn. konf. «*Problemy i perspektivy razvitiya dvigatelestroeniya*» (Samara, June 23—25, 2021). Samara university, 2021. Vol. 2. P. 251—252 (In Russ.).
20. *Давыдов Д.М., Умеров Э.Р., Латухин Е.И., Амосов А.П.* Влияние элементного порошкового сырья на формирование пористого каркаса MAX-фазы Ti_3AlC_2 при получении методом СВС. *Вектор науки Тольяттинского гос. ун-та.* 2021. Vol. 3. P. 37—47. DOI: 10.18323/2073-5073-2021-3-37-47.

Davydov D.M., Umerov E.R., Latukhin E.I., Amosov A.P. The influence of elemental powder raw material on the formation of the porous frame of Ti_3AlC_2 MAX-phase when obtaining by the SHS method. *Vektor nauki Tol'yattinskogo gosudarstvennogo universiteta.* 2021. Vol. 3. P. 37—47 (In Russ.).
21. *Bazhin P.M, Kovalev D.Yu., Luginina M.A. Averichev O.A.* Combustion of Ti—Al—C compacts in air and helium: A TRXD study. *Int. J. SHS.* 2016. Vol. 25. No. 1. P. 30—34. DOI: 10.3103/S1061386216010027.
22. Материалы металлические. Преобразование величин твердости. DIN EN ISO 18265-2014 (дата опубл. 01.02.2014).

Metallic materials. Conversion of hardness values (ISO 18265:2013) DIN EN ISO 18265-2014.

UDC 669.018.25
DOI dx.doi.org/10.17073/1997-308X-2022-3-37-44

Properties of WC–Co hardmetals as a function of their composition and microstructural parameters

© 2022 г. **V.A. Pesin, A.S. Osmakov, S.Yu. Boykov**

«Virial» LTD, Saint-Petersburg, Russia

Received 22.02.2022, revised 14.04.2022, accepted for publication 20.04.2022

Abstract: Research into WC–Co submicron hardmetals involving measurement of hardness, coercivity and microstructural characterization, as well as analysis and comparison of results from recent literature led to the development of a unified constitutive expression for Vickers hardness in a form that separates the effects of the tungsten carbide grain size from those of the cobalt binder volume fraction. With the proposed expression for *HV* one may recalculate and compare hardness values for hardmetals featuring the same average grain size but differing in the binder matrix content. The paper shows that, in contrast to the Lee-Gurland model, the proposed constitutive expression framework treats the hardmetal hardness as a function of the carbide skeleton hardness (H_{WC}) and contiguity (C) described as $HV = CH_{WC}$. The carbide skeleton hardness depends on the WC grain size only, and it is described by the Hall-Petch equation. The results of parallel hardness and coercivity measurements led to an empirical equation relating H_c to the WC grain size and the Co volume fraction. Based on the complete experimental data, the relationship between the coercivity and Vickers hardness was explored, and a simplified relationship between these physical values was proposed to carry out the primary *HV* evaluation based on the measured coercivity values. As noted in the paper, the above equations are valid for relatively narrow WC grain size distributions with a maximum coefficient of variation of 0.5.

Keywords: hardmetal, microstructure, Vickers hardness, coercivity, grain size, binder fraction, carbide skeleton, contiguity.

Pesin V.A. – Lead expert, Testing laboratory № 1, «Virial» LTD (194156, Russia, Saint-Petersburg, Engelsa pr., 27 R, of. 1-N). E-mail: PesinVA@virial.ru.

Osmakov A.S. – Cand. Sci. (Eng.), Head of testing laboratory № 1, «Virial» LTD. E-mail: OsmakovAS@virial.ru.

Boykov S.Yu. – Deputy head of testing laboratory № 1, «Virial» LTD. E-mail: BoykovSY@virial.ru.

For citation: *Pesin V.A., Osmakov A.S., Boykov S.Yu*. Properties of WC-Co hardmetals as a function of their composition and microstructural parameters. *Izvestiya Vuzov. Poroshkovaya Metallurgiya i Funktsional'nye Pokrytiya (Powder Metallurgy and Functional Coatings)*. 2022. Vol. 16. No. 3. P. 37–44 (In Russ.).
DOI: dx.doi.org/10.17073/1997-308X-2022-3-37-44.

Зависимость свойств твердых сплавов WC–Co от их состава и характеристик микроструктуры

В.А. Песин, А.С. Осмаков, С.Ю. Бойков

ООО «Вириал», г. Санкт-Петербург, Россия

Статья поступила в редакцию 22.02.22 г., доработана 14.04.22 г., подписана в печать 20.04.22 г.

Аннотация: В ходе проведенных исследований субмикронных твердых сплавов системы WC–Co, включавших в себя диагностику твердости, коэрцитивной силы и параметров микроструктуры, а также анализ и сопоставление результатов из современных литературных источников, представлена объединенная модель, согласно которой выражение для твердости по Виккерсу можно представить в виде, позволяющем разделить влияние размера зерна карбида вольфрама и объемного содержания кобальтовой связки. Предложенное выражение дает возможность проводить перерасчет и сопоставлять значения *HV* для твердых сплавов с одинаковым средним размером зерна и различным содержанием связки. В работе показано, что в отличие от модели Ли-Герланда в рамках представляемой модели твердость сплава определяется твердостью карбидного каркаса (H_{WC}) и его смежностью (C) и задается соотношением $HV = CH_{WC}$. При этом величина H_{WC} зависит

только от размера зерна карбида вольфрама и описывается уравнением типа Холла–Петча. По результатам параллельных измерений твердости и коэрцитивной силы (H_c) получено эмпирическое уравнение зависимости величины H_c от размера зерна WC и объемного содержания Co. На основании всей совокупности экспериментальных данных исследованы связи коэрцитивной силы и твердости по Виккерсу и предложено упрощенное соотношение между этими физическими показателями, позволяющее проводить первичную экспрессную оценку величины *HV* по измеренным значениям коэрцитивной силы. В работе отмечается, что приведенные соотношения справедливы для относительно узкого распределения зерен WC по размерам с коэффициентом вариации не более 0,5.

Ключевые слова: твердый сплав, микроструктура, твердость по Виккерсу, коэрцитивная сила, размер зерна, содержание связки, карбидный каркас, смежность.

Песин В.А. – вед. специалист испытательной лаборатории № 1, ООО «Вириал» (194156, г. Санкт-Петербург, пр. Энгельса, 27 Р, оф. 1-Н). E-mail: PesinVA@virial.ru.

Осмаков А.С. – канд. техн. наук, начальник лаборатории № 1, ООО «Вириал». E-mail: OsmakovAS@virial.ru.

Бойков С.Ю. – зам. начальника лаборатории № 1, ООО «Вириал». E-mail: BoykovSY@virial.ru.

Для цитирования: *Песин В.А., Осмаков А.С., Бойков С.Ю.* Зависимость свойств твердых сплавов WC–Co от их состава и характеристик микроструктуры. *Известия вузов. Порошковая металлургия и функциональные покрытия*. 2022. Т. 16. No. 3. С. 37–44. DOI: dx.doi.org/10.17073/1997-308X-2022-3-37-44.

Introduction

Many reviews and research papers have investigated the relationship between the microstructure and composition of WC—Co grades and their properties such as hardness (*HV*) and coercivity (H_c) [1—4]. Most studies assume that *HV* and H_c values are functions of the WC grain size (d_{WC}) and the volume fraction of the Co binder (V_{Co}). Empirical *HV* and H_c vs. d_{WC} and V_{Co} relationships are used to build the relevant physical models [5—10]. For most d_{WC} measurements, various versions of a single approach, the linear intercept method, are used. Unfortunately, in the case of grades with close hardness and coercivity values, these works report very different WC grain sizes. Such discrepancies are particularly evident in the submicron grain size range. For example, in the case of grades containing 10 wt.% of Co and the average grain size d_{WC} = 0.5 μm, the reported hardness ranges from 1540 to 1820 HV_{30}, for d_{WC} = 0.6 μm, 1610 to 1798 HV_{30}, and for c d_{WC} = 0.7 μm, 1431 to 1720 HV_{30}. The empirical relationships are also very different and therefore of little use.

Papers [11—13] consider the metrological aspects of WC grain size measurements. The results presented in [3, 6, 10] seem to be highly reliable. We believe that the empirical hardness vs. grain size and binder content relationships from [3, 6] can be used to find the relationships with other hardmetal properties.

The hardness vs. WC grain size relationships in [3] measured by the linear intercept (d_c) are Hall—Petch-type relationships for grades with 6 and 10 wt.% Co, respectively:

$$HV = 970 + 540 d_c^{-1/2}, \quad (1)$$

$$HV = 850 + 485 d_c^{-1/2}. \quad (2)$$

Kresse T. et al. [6] obtained an empirical equation for hardness, and tungsten carbide grain size (where d_F is the max Feret diameter) vs. cobalt volume content from the experimental results for WC—Co grades in a wide range of Co contents (5—25 wt.%):

$$HV = \alpha(V_{Co})[729 + 718(d_F + 0.13)^{-1/2}], \quad (3)$$

wherein the first factor $\alpha(V_{Co}) = 0.5/(V_{Co} + 0.331)$ represents the contribution of the binder, and the second factor, that of the carbide component as a Hall—Petch relationship with the complex argument (d_F + 0.13). It limits the infinite growth of *HV* as d_F approaches zero. Comparing the estimations with equations (1)—(2) and (3) is of considerable interest, but first, we need to find the d_c vs. d_F relationship.

The study objectives are as follows:

— to analyze the WC—Co grades' hardness vs. composition and microstructure relationship;

— to use the measured HV and H_c values for a number of grades, and to identify the coercivity vs. composition and microstructure relationship;

— to prove the existence of a correlation between the HV, H_c, and d_{WC} values for the WC—Co hardmetal under certain conditions.

Test samples and methods

The samples consisted of submicron WC—Co tool hardmetal from Sandvik (Sweden), Konrad Friedrich and Konrad Micro Drill (Germany), Iscar (Israel), Gesac (China), and Virial (Russia). The carbon content is close to the stoichiometric value.

In order to evaluate Vickers hardness, the polished microsections were analyzed using a Falcon 508 hardness tester (Netherlands) at 294 N.

A Koerzimat 1.096 CS measuring system (Germany) was used to measure coercivity. We estimated the microstructural features using the Fiji software (USA) by analyzing the images obtained with a Mira 3 scanning electron microscope (SEM) (Tescan, Czech Republic). The images represented the surfaces of the samples etched and pre-polished with diamond suspensions. The etching process consisted of soaking the samples in the Murakami solution for 60s followed by rinsing and a 10-minute ultrasonic bath cleaning. Five SEM images were used to estimate the grain size. The FOV was 7.22 μm, with 80$^{\times}$ magnification.

Hardness vs. WC grain size and Co binder content

The linear intercept (d_c) method assumes that the single WC grain size is the length of an arbitrary chord. Therefore, the grain size is the «average» chord length. The grade's average grain size estimated with the linear intercept method is double-averaged and does not significantly depend on WC grain shape. If we assume the equivalent circle diameter (d_{eqv}) to be the grain size, its average value does not depend on the WC grain shape, and the d_c to d_{eqv} ratio loosely depends on the grain morphology: $d_{eqv} \approx 1.15\, d_c$ [13].

When the max Feret diameter (the longest chord) is assumed to be the grain size, the average grain size (d_F) strongly depends on the grain isometricity. We can expect that in commercially available grades the degree of grain isometricity varies in a relatively narrow range. Therefore, in order to find the d_c/d_F ratio, we selected 6 grades from different manufacturers. Their average grain size dc was 0.39—0.68 μm. We used the samples to measure d_c and d_F. We obtained $d_c/d_F = 0.70 \pm 0.04$.

Since the variation did not exceed 10 %, we used the result to modify equation (3):

$$HV = [0.5/(V_{Co} + 0.331)] \times \times [729 + 601(d_c + 0.09)^{-1/2}], \quad (3a)$$

For grades with 6 and 10 wt.% Co respectively we obtain:

$$HV = 842 + 694(d_c + 0.09)^{-1/2}, \quad (4)$$

$$HV = 735 + 606(d_c + 0.09)^{-1/2}. \quad (5)$$

These equations are more suitable for comparison of the grade hardness vs. WC grain size relationships presented in [3] and [6].

Fig. 1 shows the hardness vs. grain size relationships for grades with 6 and 10 wt.% Co content obtained from equations (1), (4) and (2), (5), respectively. Our experimental data and the data from the studies [3, 6, 10] are also indicated.

Within the experimental data scattering for the 0.2—5.0 μm grain size range, the approximations presented in [3] and [6] give similar results. In the nanoscale range ($d_c < 0.2$ μm), the plastic deformation mechanisms change, and equations (1) and (2) are no longer valid. Therefore, it is preferable to use modified equation (3a). For example, in the case of grades with 10 wt.% Co and 0.14 μm [14] and 0.061 μm [15] grain sizes, equation (3a) gives 2000 and 2294 HV hardness values, respectively. This is in satisfactory agreement with the experimental values (2036 and 2356 HV).

The model by Kresse T. et al. [6], where the grade's hardness is determined by the hardness of its carbide network while the contribution of the Co content is expressed as a normalizing function. For $d_c > 0.2$ μm the model unifies the Hall—Petch factors for different Co concentrations:

$$HV = [0.5/(V_{Co} + 0.331)](850 + 485 d_c^{-1/2}). \quad (6)$$

For example, for 10 wt.% Co, $\alpha(V_{Co}) \approx 1$, we obtain equation (2). For 6 wt.% Co, $\alpha(V_{Co}) \approx 1.155$,

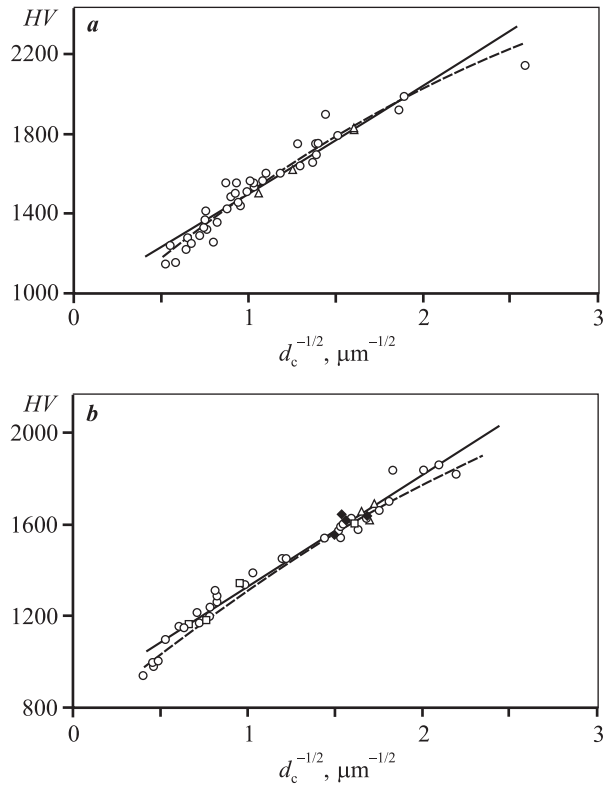

Fig. 1. Hardness of 6 wt.% Co grades (***a***), and 10 wt.% Co grades (***b***) as a function of WC grain size

Solid lines mean calculation as per Equation (1) (***a***) and Equation (2) (***b***) [3], dashed lines mean calculation as per Equation (4) (***a***) and Equation (5) (***b***); symbols mean ○ – experimental data from [3]; △ – experimental data from [6]; □ – experimental data from [10]; ◆ – Virial's own measurements

Рис. 1. Зависимость твердости сплавов с 6 мас.% (***a***) и 10 мас.% Co (***b***) от величины зерна WC

Сплошные линии – расчет на основании уравнений (1) (***a***) и (2) (***b***) [3], штриховые – расчет по уравнениям (4) (***a***) и (5) (***b***); значки – экспериментальные данные [3] (○), [6] (△), [10] (□) и собственные измерения ООО «Вириал» (◆)

then $HV = 982 + 560d_c^{-1/2}$, which is almost identical to (1).

For $V_{Co} = 0$, equation (6) becomes:

$$HV_{WC} = 1284 + 733d_c^{-1/2}, \quad (7)$$

where the factors are similar to the results presented in [16] (1382 and 731) and [17, 18] (1112 and 911). Equations (3a) and (6) enable comparison of the hardness of grades with different binder volume contents (at least for the $0.08 \le V_{Co} \le 0.24$ range), and to estimate the grain sizes.

The physical meaning of $\alpha(V_{Co})$ becomes clear, if we compare it to the carbide network contiguity (connectivity). C. Roebuck B. et al. [12] proposed the following equation for contiguity:

$$C = 1 - 1.27V_{Co}^{0,75}. \quad (8)$$

Fig. 2 shows a comparison of $\alpha(V_{Co})$ and C values for WC—Co grades with the $V_{Co} \le 0.24$ cobalt volume content. It follows that:

$$\alpha(V_{Co}) \approx 1.5C. \quad (9)$$

Then the expression for hardness can be expressed as

$$HV = C(1284 + 733d_c^{-1/2}). \quad (10)$$

HV vs. tungsten carbide grain size and binder content in WC—Co grades is well described using the comprehensible phenomenological model. The grade's hardness depends on the hardness of its carbide network, while the volume content of the binder governs the contiguity of the network.

It should be noted that, as shown in [19], the WC—WC interfaces may or may not contain Co interlayers 3 to 30 nm thick, depending on the carbon content. It is not clear how the presence of such nanosheets affects the mechanical properties of the grade and whether we should adjust the concept of the carbide network and

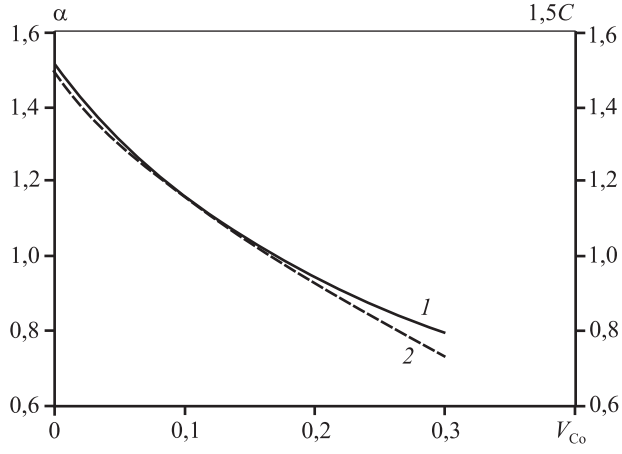

Fig. 2. Ratio between the coefficient $\alpha(V_{Co})$ (***1***) and contiguity C (***2***) depending on Co binder fraction

Рис. 2. Соотношение между коэффициентом $\alpha(V_{Co})$ (***1***) и смежностью C (***2***) в зависимости от содержания Co-связки

its contiguity in grades with nearly stoichiometric carbon content.

Coercivity vs. WC grain size and Co binder content

In order to find the coercivity vs. WC grain size relationship for a number of tool hardmetals from different manufacturers (6, 10, and 12 wt.% Co content), we concurrently measured H_c and HV. Then we applied combined equation (6) to the measured HV values, in order to estimate the grain size (d_p). The solid lines in Fig. 3 show the curves for 6, 10, and 12 wt.% Co alloys. They are well fitted by the following empirical equations:

$$H_c = 54.7 + 102 d_p^{-1}, \quad (12)$$

$$H_c = 50.8 + 83 d_p^{-1}, \quad (13)$$

$$H_c = 53.0 + 76 d_p^{-1}. \quad (14)$$

Within the margin of error, we can assume the free terms in equations (12)—(14) are all equal to 53 Oe,

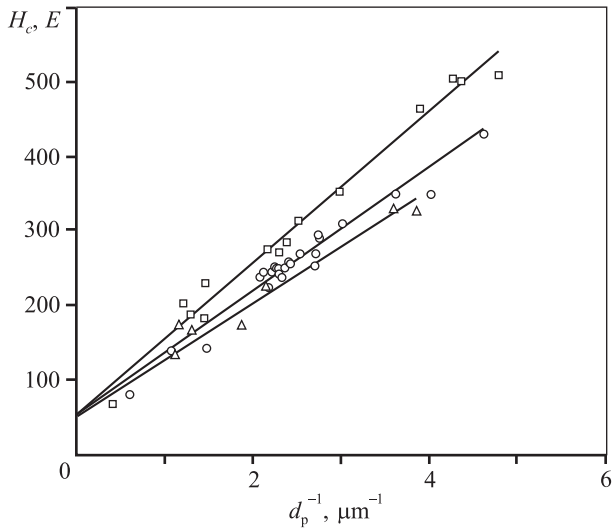

Fig. 3. Coercivity HC as a function of WC grain size in grades with different Co binder content:
□ – grades with 6 wt.% Co; ○ – grades with 10 wt.% Co; △ – grades with 12 wt.% Co

Рис. 3. Зависимость коэрцитивной силы от размера зерна WC в сплавах с различным содержанием Co-связки, мас.%: 6 (□), 10 (○) и 12 (△)

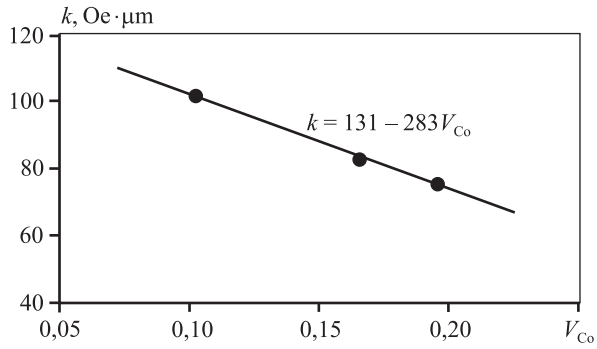

Fig. 4. Coefficient k as a function of cobalt volume fraction

Рис. 4. Зависимость коэффициента k от объемного содержания кобальта

while the k multiplier of d_p^{-1} linearly varies with the binder volume content (Fig. 4) within the 6—12 wt.% Co range. This relationship can be expressed as $k = 131 - 283V_{Co}$.

By substituting the calculated d_p value with d_c in equations (12)—(14), we obtain the following expression for the H_c coercivity vs. grain size and binder content:

$$H_c = 53 + (131 - 283V_{Co}) d_c^{-1}. \quad (15)$$

Since the empirical dependences (12)—(14) and, respectively, (15) were obtained with the grain size (d_p) values estimated by equation (6), they are valid for the 0.2—5.0 μm grain size.

Hardness vs. coercivity relationship

Fig. 5 shows our concurrent H_c and HV measurements for 6, 10, and 12 Co wt.% alloys. The solid lines indicate the estimated coercivity vs. hardness relationships obtained from equations (6) and (15). It follows from the figure that the relationships satisfactorily describe the experimental data. The data variation is due to certain variations of the hardmetal manufacturing process variables. The manufacturers usually specify [20—25] a fairly wide range of acceptable hardness and coercivity values: ±50 HV and ±35 Oe, respectively. Such a variation should be considered when analyzing the relationships for many different grades.

In hardmetal manufacturing, magnetic measurements are one of the first express NDT stages of sintered

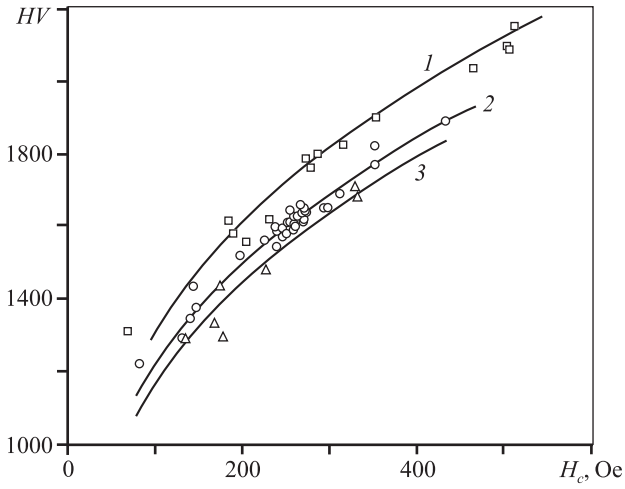

Fig. 5. Relationship between hardness and coercivity in the researched grades

Solid lines mean *HV* and H_c calculated as per Equation (6) and Equation (15), respectively, for grades with 6 wt.% Co (***1***); 10 wt.% Co (***2***); 12 wt.% Co (***3***); symbols mean experimental data: □ – grades with 6 wt.% Co; ○ – grades with 10 wt.% Co; △ – grades with 12 wt.% Co

Рис. 5. Соотношение между твердостью и коэрцитивной силой в исследованных сплавах

Сплошные линии – расчетные данные для *HV* и H_c сплавов с 6 (***1***), 10 (***2***) и 12 мас.% Co (***3***) по уравнениям (6) и (15) соответственно; значки – экспериментальные данные для сплавов с 6 Co (□), 10 Co (○) и 12 мас.% Co (△)

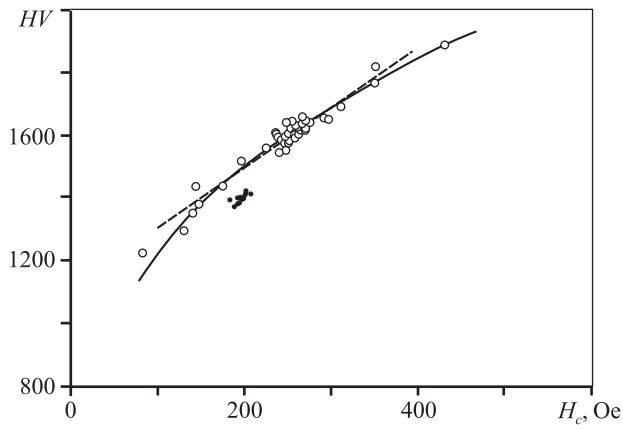

Fig. 6. $HV(H_c)$ ratio for grades with 10 wt.% Co (part of Fig. 5)

Solid line corresponds to theoretical curve *2* in Fig. 5, dashed line corresponds to linear approximation as per Equation (16); • – mean experimental data for VHS11 grade (Virial)

Рис. 6. Соотношение $HV(H_c)$ для сплавов с 10 мас.% Co (фрагмент рис. 5)

Сплошная линия соответствует расчетной кривой ***2*** на рис. 5, штриховая – линейная аппроксимация согласно уравнению (16); • – экспериментальные данные для сплава VHS11(ООО «Вириал»)

products. As Fig. 6 shows, for 10 wt.% Co grades, the following linear approximation

$$HV = 1{,}932H_c + 1112. \quad (16)$$

can be used as an express hardness assessment from coercivity (in the 110—350 Oe range).

It should be noted that the hardness and coercivity of WC—Co grades depend not only on the average grain size and Co binder content, but also on a number of other factors [3]. Therefore, we can expect some deviations from the proposed relationships for grades with wide or bimodal WC grain size distributions [26]. For example, the VHS11 grade, 10 wt.% Co (from Virial) was developed to offer both relatively high hardness (≈1400 HV) and fracture toughness (≥ 13.5 MPa·m$^{1/2}$). It has a wide WC grain size distribution. As shown in Fig. 6, it results in a noticeable change in the *HV* to H_c ratio compared to the grades with a narrower grain size distribution (CV less than 0.5).

Discussion

As we noted earlier, Roebuck B. et al. [3] provided the experimental approach to building the models by describing the hardness vs. WC grain size and binder content relationships. Kresse T. et al. [6] proposed a semi-empirical model in which grade's hardness is determined by the hardness of its carbide network normalized with a binder content factor. The carbide network hardness in their model is a Hall—Petch function of a complex argument. The max Feret diameter is assumed to be the WC grain size. It makes it impossible to directly compare the results since most publications refer to the average grain size determined by the linear intercept method.

We obtained the experimental hardness vs. average WC grain size relationships using the linear intercept method (d_c), the max Feret diameter (d_F), and modified equation (3) to (3a), in which dc is included. Such a modification makes it possible to compare a large number of published experimental datasets with the estimated values. The comparison showed that the hardness vs. average grain size and binder volume content relationship (3) [6] provides a good agreement with ex-

perimental data in a wide range of grain sizes: from the nanoscale to coarse.

In the case of $d_c > 0.2$ μm, we applied the $\alpha(V_{Co})$ normalization factor, in order to produce equation (6) which expresses the grade's hardness as a single Hall—Petch relationship for different Co binder contents. The $\alpha(V_{Co})$ to C ratio for hardmetals which we found makes the unified model clearer: The hardness of a grade with a nearly stoichiometric carbon content is a product of the carbide network hardness and contiguity.

In order to find the coercivity vs. grain size relationship, we used d_p estimated from the hardness values produced by equation (6). The *HV* variation of the same grain sizes can lead to a d_p estimation error. We evaluated the average deviation of the experimental hardness values from the trend curve presented in [3]. It does not exceed 30 HV, which corresponds to a less than 9 % uncertainty of the estimated grain size value. Since hardness values deviations are random, the estimated d_p errors are also random. This will cause more scattering relative to the trend curve, as we analyze the coercivity vs. grain size relationship. If the number of samples is sufficient, it does not affect the trend curve equation. Another confirmation of this is the good agreement between the experimental and estimated *HV* and H_c values as shown in Fig. 5.

Conclusions

1. We analyzed studies [3] and [6] and proposed a combined model to express *HV* as:

$$HV = [0{,}5/(V_{Co} + 0{,}331)](850 + 485 d_c^{-1/2})$$

and to compare the harnesses of grades with the same grain sizes and different binder volume contents in the $0.08 \le V_{Co} \le 0.24$ range for $d_c > 0.2$ μm.

2. As a part of the model, we obtained a simple relationship between the grade's hardness, the carbide framework hardness (HV_{WC}), and contiguity (*C*):

$$HV = C \cdot HV_{WC},$$

$$HV_{WC} = 1284 + 733 d_c^{-1/2}.$$

3. The coercivity vs. grain size and binder content relationship was found for grades with a 6—12 wt.% Co content:

$$H_c = 53 + (131 - 283 V_{Co})\, d_c^{-1}.$$

4. We proposed an equation for the coercivity vs. hardness for grades with a 10 wt.% cobalt binder content:

$$HV = 1{,}932 H_c + 1112.$$

References

1. *Shatov A.V., Ponomarev S.S., Firstov S.A.* Hardness and deformation of hardmetals at room temperature. In: *Comprehensive hard materials* (ed. Vinod K. Sarin). Oxford: Elsevier, 2014. P. 267—299.
2. *Topić I., Sockel H., Göken M.* The influence of microstructure on the magnetic properties of WC/Co hardmetals. *Mater. Sci. Eng. A*. 2006. Vol. 423. Iss. 1-2. P. 306—312. DOI: 10.1016/J.MSEA.2006.02.018.
3. *Roebuck B.* Extrapolating hardness-structure property maps in WC/Co hardmetals. *Int. J. Refract. Met. Hard Mater.* 2006. Vol. 24. Iss. 1. P. 101—108. DOI: 10.1016/j.ijrmhm.2005.04.021.
4. *Love A., Luyckx S., Sacks N.* Quantitative relationships between magnetic properties, microstructure and composition of WC—Co alloys. *J. Alloys Compd*. 2010. Vol. 489. No. 2. P. 465—468. DOI: 10.1016/j.jallcom.2009.09.087.
5. *Engqvist H., Jacobson S., Axén N.* A model for the hardness of cemented carbides. *Wear.* 2002. Vol. 252. Iss. 5-6. P. 384—393. DOI: 10.1016/S0043-1648(01)00866-3.
6. *Kresse T., Meinhard D., Bernthaler T., Schneider G.* Hardness of WC—Co hard metals: Preparation, quantitative microstructure analysis, structure-property relationship and modelling. *Int. J. Refract. Met. Hard Mater.* 2018. Vol. 75. P. 287—293. DOI: 10.1016/j.ijrmhm.2018.05.003.
7. *Makhele-Lekala L., Luyckx S., Nabarro F.R.N.* Semi-empirical relationship between the hardness, grain size and mean free path of WC—Co. *Int. J. Refract. Met. Hard Mater.* 2001. Vol. 19. Iss. 4-6. P. 245—249. DOI: 10.1016/S0263-4368(01)00022-1.
8. *Golovchan V.T.* Some analytical consequences of experimental data on properties of WC—Co hardmetals. *Int. J. Refract. Met. Hard Mater.* 2008. Vol. 26. Iss. 4. P. 301—305. DOI: 10.1016/j.ijrmhm.2007.07.001.
9. *Roebuck B.* Terminology, testing, properties, imaging and models for fine grained hardmetals. *Int. J. Refract. Met. Hard Mater.* 1995. Vol. 13. Iss. 5. P. 265—279. DOI: 10.1016/0263-4368(95)92673-8.
10. *Tarrago J.M., Coureaux D., Torres Y., Jimenez-Pique E., Schneider L., Fair J., Llanes L.* Strength and reliability of

WC—Co cemented carbides: understanding microstructural effects on the basis of R-curve behavior and fractography. *Int. J. Refract. Met. Hard Mater.* 2018. Vol. 71. P. 221—226. DOI: 10.1016/J.IJRMHM.2017.11.031.

11. *Mingard K.P., Roebuck B., Bennett E.G., Gee M.G., Nordenstrom H., Sweetman G., Chan P.* Comparison of EBSD and conventional methods of grain size measurement of hardmetals. *Int. J. Refract. Met. Hard Mater.* 2009. Vol. 27. Iss. 2. P. 213—223. DOI: 10.1016/j.ijrmhm.2008.06.009.
12. *Roebuck B., Mingard K.P., Jones H., Bennett E.G.* Aspects of the metrology of contiguity measurements in WC based hard materials. *Int. J. Refract. Met. Hard Mater.* 2017. Vol. 62. P. 161—169. DOI: 10.1016/j.ijrmhm.2016.05.011.
13. *Tarragó J.M., Coureaux D., Torres Y., Wua F., Al-Dawery I., Llanes L.* Implementation of an effective time-saving two-stage methodology for microstructural characterization of cemented carbides. *Int. J. Refract. Met. Hard Mater.* 2016. Vol. 55. P. 80—86. DOI: 10.1016/j.ijrmhm.2015.10.006.
14. *Vornberger A., Potschke J., Gestrich T., Herrmann M., Michaelis A.* Influence of microstructure on hardness and thermal conductivity of hardmetals. *Int. J. Refract. Met. Hard Mater.* 2020. Vol. 88. Art. 105170. DOI: 10.1016/j.ijrmhm.2019.105170.
15. *Peng Y., Wang H., Zhao C., Hu H., Liu X., Song X.* Nanocrystalline WC—Co composite with ultrahigh hardness and toughness. *Composites Pt. B.* 2020. Vol. 197. Art. 108161. DOI: 10.1016/j.copositesb.2020.108161.
16. *Lee H.C., Gurland J.* Hardness and deformation of cemented tungsten carbides. *Mater. Sci. Eng.* 1978. Vol. 33. P. 125—133. DOI: 10.1016/0025-5416(78)90163-5.
17. *Nino A., Takahashi K., Sugiyama S., Taimatsu H.* Effects of carbon addition on microstructures and mechanical properties of binderless tungsten carbide. *Mater. Trans.* 2012. Vol. 53. Iss. 8. P. 1475—1480. DOI: 10.2320/matertrans.M2012148.
18. *Nino A., Izu Y., Sekine T., Sugiyama S., Taimatsu H.* Effects of TaC and TiC addition on microstructures and mechanical properties of binderless WC. *Int. J. Refract. Met. Hard Mater.* 2019. Vol. 82. P. 167—173. DOI: 10.1016/j.ijrmhm.2019.04.012.
19. *Konyashin I., Zaitsev A.A., Sidorenko D., Levashov E.A., Ries B., Konischev S.N., Sorokin M., Mazilkin A.A., Herrmann M., Kaiser A.* Wettability of tungsten carbide by liquid binders in WC—Co cemented carbides: Is it complete for all carbon contents? *Int. J. Refract. Met. Hard Mater.* 2017. Vol. 62. P. 134—148. DOI: 10.1016/J.IJRMHM.2016.06.006.
20. German Carbide. URL: https://german-carbide.com/en/products-2/ (accessed: 30.03.2022).
21. Boehlerit. URL: https://www.boehlerit.com/en/ (accessed: 30.03.2022).
22. Hyperion cemented carbide grades. URL: https://www.hyperionmt.com/products/Carbide-rods/product-series-grade/ (accessed: 17.12.2021).
23. Ultra Carbide Grade Chart. URL: https://ultracarbide.com/ (accessed: 17.12.2021).
24. Iscar. URL: https://www.iscar.com/ (accessed: 17.12.2021).
25. Gesac. URL: https://gesac.ru (accessed: 17.12.2021).
26. *Engqvist H., Uhrenius B.* Determination of the average grain size of cemented carbides. *Int. J. Refract. Met. Hard Mater.* 2003. Vol. 21. Iss. 1. P. 31—35. DOI: 10.1016/S0263-4368(03)00005-2.

UDC 621-033.6:669.018.9; 621-033.6:666.1/.7; 621-033.6:666.1
DOI dx.doi.org/10.17073/1997-308X-2022-3-45-54

Fabrication and oxidation resistance of the non-stoichiometric tantalum-hafnium carbonitride

© 2022 г. **V.S. Suvorova, A.A. Nepapushev, D.O. Moskovskikh, K.V. Kuskov**

National University of Science and Technology (NUST) «MISIS», Moscow, Russia

Received 14.04.2022, revised 21.04.2022, accepted for publication 29.04.2022

Abstract: This research was conducted to obtain non-stoichiometric tantalum-hafnium carbonitride powder of the *Fm*3*m* (225) structural type using a combination of mechanical activation (MA) and self-propagating high-temperature synthesis (SHS) methods. Mechanical activation for 60 min in a low-energy mode (347 rpm) forms Ta/Hf/C composite particles 1 to 20 μm in size with a layered structure and contributes to a uniform distribution of elements. SHS of a mechanically activated Ta + Hf + C mixture in a nitrogen atmosphere (0.8 MPa) leads to the formation of a single-phase tantalum-hafnium carbonitride powder with the $Ta_{0.25}Hf_{0.75}C_{0.5}N_{0.3}$ composition where particles feature by a «spongy» morphology with pores and caverns and consist of submicron grains. Spark plasma sintering (SPS) was used to obtain a bulk sample of tantalum-hafnium carbonitride with a grain size of 3 to 5 μm, relative density of 98.2 ± 0.3 %, hardness of 19.8 ± 0.2 GPa, and crack resistance of 5.4 ± 0.4 MPa·$m^{1/2}$. The kinetics of (Ta,Hf)CN oxidation at 1200 °C in air is described by a parabolic law suggesting the formation of an $Hf_6Ta_2O_{17}$ + *m*HfO_2 oxide layer with a low oxygen diffusion rate where the oxidation rate is 0.006 mg/(cm^2·s). A (Ta,Hf)CN oxidation mechanism is proposed, which states that Ta_2O_5 and HfO_2 are formed on the surface of grains at the first stage that react with each other at the second stage to form a $Hf_6Ta_2O_{17}$ homologous superstructure and monoclinic HfO_2. CO, CO_2, NO and NO_2 gaseous oxidation products are released with the formation of pores and cracks.

Keywords: carbonitride, mechanical activation, self-propagating high-temperature synthesis (SHS), ceramics, spark plasma sintering (SPS), oxidation resistance.

Suvorova V.S. – Postgraduate student, Department of powder metallurgy and functional coatings, Engineer of the scientific project of the Science and Research Center (SRC) «Functional nanoceramic», National University of Science and Technology (NUST) «MISIS» (119049, Russia, Moscow, Leninskiy pr., 4). E-mail: buynevich.vs@misis.ru.

Nepapushev A.A. – Cand. Sci. (Eng.), Senior researcher, SRC «Functional nanoceramic», NUST «MISIS». E-mail: anepapushev@gmail.com.

Moskovskikh D.O. – Cand. Sci. (Eng.), Director of SRC «Functional nanoceramic», NUST «MISIS». E-mail: mos@misis.ru.

Kuskov K.V. – Research scientis, SRC «Functional nanoceramic», NUST «MISIS». E-mail: kkuskov@misis.ru.

For citation: *Suvorova V.S., Nepapushev A.A., Moskovskikh D.O., Kuskov K.V.* Fabrication and oxidation resistance of the non-stoichiometric tantalum-hafnium carbonitride. *Izvestiya Vuzov. Poroshkovaya Metallurgiya i Funktsional'nye Pokrytiya (Powder Metallurgy and Functional Coatings).* 2022. Vol. 16. No. 3. P. 45–54 (In Russ.). DOI: dx.doi.org/10.17073/1997-308X-2022-3-45-54.

Получение нестехиометрического тантал-гафниевого карбонитрида и исследование его окислительной стойкости

В.С. Суворова, А.А. Непапушев, Д.О. Московских, К.В. Кусков

Национальный исследовательский технологический университет «МИСиС», г. Москва, Россия

Статья поступила в редакцию 14.04.2022 г., доработана 21.04.2022 г., подписана в печать 29.04.2022 г.

Аннотация: В данной работе комбинацией методов механического активирования (МА) и самораспространяющегося высокотемпературного синтеза (СВС) получен порошок нестехиометрического тантал-гафниевого карбонитри-

да структурного типа *Fm*3*m* (225). Механическое активирование в течение 60 мин в низкоэнергетическом режиме (347 об/мин) приводит к формированию композиционных частиц Ta/Hf/C слоистой структуры, размер которых варьируется от 1 до 20 мкм, и способствует равномерному распределению элементов. Продуктом СВС механоактивированной смеси Ta + Hf + C в среде азота (0,8 МПа) является однофазный порошок тантал-гафниевого карбонитрида состава $Ta_{0,25}Hf_{0,75}C_{0,5}N_{0,3}$, частицы которого характеризуются губчатой морфологией с порами и кавернами и состоят из субмикронных зерен. Посредством искрового плазменного спекания (ИПС) получен объемный образец тантал-гафниевого карбонитрида, размер зерен которого варьируется от 3 до 5 мкм, с относительной плотностью 98,2 ± 0,3 %, твердостью 19,8 ± 0,2 ГПа и трещиностойкостью 5,4 ± 0,4 МПа·м$^{1/2}$. Кинетика окисления (Ta,Hf)CN при температуре 1200 °C на воздухе описывается параболическим законом, что свидетельствует о формировании оксидного слоя $Hf_6Ta_2O_{17}$ + *m*HfO_2 с низкой скоростью диффузии кислорода, скорость окисления при этом составляет 0,006 мг/(см^2·с). Предложен механизм окисления (Ta,Hf)CN, заключающийся в том, что на первой стадии на поверхности зерен формируются Ta_2O_5 и HfO_2, которые на второй стадии вступают в реакцию друг с другом с образованием гомологичной сверхструктуры $Hf_6Ta_2O_{17}$ и моноклинного HfO_2. Высвобождение газообразных продуктов окисления CO, CO_2, NO и NO_2 сопровождается образованием пор и трещин.

Ключевые слова: карбонитрид, механическое активирование, самораспространяющийся высокотемпературный синтез (СВС), керамика, искровое плазменное спекание (ИПС), окислительная стойкость.

Суворова В.С. – аспирант кафедры порошковой металлургии и функциональных покрытий, инженер научного проекта НИЦ «Конструкционные керамические наноматериалы», НИТУ «МИСиС» (119049, г. Москва, Ленинский пр-т, 4). E-mail: buynevich.vs@misis.ru.

Непапушев А.А. – канд. техн. наук, ст. науч. сотрудник НИЦ «Конструкционные керамические наноматериалы», НИТУ «МИСиС». E-mail: anepapushev@gmail.com.

Московских Д.О. – канд. техн. наук, директор НИЦ «Конструкционные керамические наноматериалы», НИТУ «МИСиС». E-mail: mos@misis.ru.

Кусков К.В. – науч. сотрудник НИЦ «Конструкционные керамические наноматериалы», НИТУ «МИСиС». E-mail: kkuskov@misis.ru.

Для цитирования: *Суворова В.С., Непапушев А.А., Московских Д.О., Кусков К.В.* Получение нестехиометрического тантал-гафниевого карбонитрида и исследование его окислительной стойкости. *Известия вузов. Порошковая металлургия и функциональные покрытия*. 2022. Т. 16. No. 3. С. 45–54. DOI: dx.doi.org/10.17073/1997-308X-2022-3-45-54.

Introduction

Few of the most advanced materials can withstand intensive mechanical and thermal loads above 2000 °C. The only choice is group IVB and VB transition metal compounds: borides, carbides, and nitrides. Due to the presence of strong covalent and ionic bonds, these materials have high melting temperatures (>2,500 °C), excellent mechanical and thermophysical properties, and chemical and phase stability [1, 2]. Tantalum and hafnium carbides are of special interest among other refractory compounds. They have the highest melting points (3,880 and 3,890 °C, respectively), a higher hardness (~25 GPa), elastic modulus (~450 GPa), and strength (~250 MPa) while thermal conductivity ranges from 20 to 30 W/(m·K) [3—5].

A significant disadvantage of refractory compounds is their relatively low oxidation resistance. Most of them work well in protective atmospheres, while in the air they oxidize intensively at 400—800 °C, forming porous and cracking oxide films, which cannot protect the base material from further oxidation [6].

There are several approaches to increasing their heat resistance. For example, the addition of SiC to refractory ceramics initiates the formation of a dense $MeSiO_4$ oxide layer, thus preventing oxygen diffusion to the material [7, 8]. Another approach is to create more complex compounds from refractory transition metal carbides and nitrides. Such solid solutions tend to have enhanced physical, mechanical, and thermophysical properties, and higher oxidation resistance, since refractory oxide films with low oxygen diffusion rates are formed [9]. Savvatimskiy A. et al. [10] showed that the $Ta_{0.80}Hf_{0.20}C$ melting temperature is 4030 °C. It significantly exceeds the melting temperatures of tantalum and hafnium carbides, the current «record-breakers». Kurbatkina V. et al. [11] demonstrated

that double carbides (Ta, Hf)C and (Ta, Zr)C have a higher hardness and Young's modulus compared to binary compounds.

Among the complex compounds, transition metal carbonitrides are no less interesting in terms of high-temperature applications. Hong Q.J. et al. [12] performed a theoretical analysis and showed that the introduction of nitrogen atoms into the lattice of refractory (Ta, Hf)C increases not only the melting point but also the oxidation resistance. As they reported, for the Ta—Hf—C—N system the tantalum-hafnium carbonitride ($Hf_{0.75}Ta_{0.25}C_{0.5}N_{0.25}$) has the highest properties. We thus decided to manufacture this compound and analyze its properties.

However, the synthesis of non-stoichiometric compounds is challenging. Conventional technologies produce only MeC_xN_{1-x} stoichiometric phases, since it is not possible to adjust the nitrogen content in the final product. An alternative method for producing a wide range of multicomponent compounds is self-propagating high-temperature synthesis (SHS) [13], as developed by A.G. Merzhanov and I.P. Borovinskaya in 1972. This is a simple, single-stage, and highly efficient process.

This study aims to manufacture (Ta, Hf)CN dense ceramics by means of spark plasma sintering. The raw material is the powder produced by SHS of mechanically agitated activated Ta + Hf + C mixture in a nitrogen environment. Ceramics oxidation resistance was also studied.

Materials and methods

Hafnium powder HFM-1 (TU 48-4-176-85 (97) specification, particle size $d \leq 50$ μm, 98.8 % purity), tantalum powder TaP-1 (TU 1870-258-00196109-01 95.136-69 specification, particle size $d = 40 \div 60$ μm, 99.9 % purity) and carbon black P804T (TU 38-1154-88 specification, particle size $d \leq 0.2$ μm, 99.5 % purity) were used as precursors. The mechanical milling was performed in an argon environment using a 4.8 Grade argon (GOST 10157-79, 99.993 % purity). The SHS process involved filtration combustion in grade 1 nitrogen (GOST 9293-74, 99.999 % purity).

Before synthesis, the Ta + Hf + C powder mixture (24.3 Ta + 72.1 Hf + 3.6 C wt.%) was mechanically activated in an Activator-2S high-performance planetary ball mill (Activator, Russia). The powder mixture and steel balls (1 : 20 weight mass ratio) were loaded into steel jars filled with argon at 0.6 MPa. Mechanical activation lasted for 60 min at a 347 rpm speed of the jars.

A constant-pressure lab reactor was used for the SHS process. The activated Ta + Hf + C powder mixture was placed loosely on a removable reactor rack. The reactor chamber was evacuated with a fore vacuum pump. Then nitrogen was pumped through a dedicated pipe to a pressure of 0.8 MPa. A self-sustaining exothermic reaction was initiated by briefly applying a voltage to the tungsten coil connected to the power supply.

The SHS powder was consolidated with a Labox 650 spark plasma sintering machine (SinterLand, Japan) in an argon environment at 2000 °C, 50 MPa press pressure, and 20 min. holding time. The heating rate was 100 °C/min.

The microstructure and elemental composition were analyzed with a JSM-7600F scanning electron microscope (JEOL Ltd., Japan) equipped with an INCA SDD 61 X-MAX *X*-ray microanalysis system (Oxford Instruments, UK) in backscattered electron mode, 15 kV accelerating voltage and 3 nm resolution.

The phase composition of the powders after mechanical activation and SHS and of the sintered samples was studied using a Diffray-401 *X*-ray diffractometer (Research Instruments, Russia), CuK_α radiation, step scanning mode (scanning step: 0.1°) 20° to 100°angle range, 2 s exposure. The ICDD PDF databases were used to analyze the resulting spectra.

The nitrogen and carbon contents in the synthesized powders and sintered samples were determined by carrier gas hot extraction. A TC-600 (Leco, USA) instrument estimated the amount of nitrogen and oxygen in the compounds by IR adsorption (for oxygen) and thermal conductivity (for nitrogen) analysis during the reduction melting of the samples in a resistance furnace in a helium flow. A CS-600 (Leco) instrument was used to measure the carbon content. For this purpose, the samples were subjected to oxidative melting in an induction furnace and the amount of CO_2 released was measured by IR absorption.

The density of compacted ceramic materials was determined by hydrostatic weighing under GOST 20018-74 [14]. At least 10 measurements were taken in air and distilled water ($\rho_w = 0.9978$ g/cm^3). A layer of vaseline

(ρ_v = 0.870 g/cm^3) was applied to cover the open pores. We applied an ES 220A analytical balance (Precisa, Switzerland), ±0.0001 g accuracy.

A Micro-Hardness Tester (CSM Instruments, Switzerland) was used to measure Young's modulus (*E*) at a 100 mN applied load.

We used a Durascan 70 hardness testing machine (Struers ApS, Denmark) to estimate the hardness and crack resistance of the consolidated materials by the Vickers method, GOST 2999-75 [15]. A max load of 9.8 kg was applied for 20 s. After the load was removed, the diagonals of the imprint on the sample surface and the crack lengths were measured. At least 10 measurements were taken with each sample. The software evaluated the hardness automatically. We used the Anstis equation to assess the fracture toughness:

$$K_{1c} = 0{,}016\left(\frac{E}{HV}\right)^{1/2}\frac{P}{c^{3/2}}, \quad (1)$$

wherein *E* is Young's modulus, GPa; *HV* is the hardness, GPa; *P* is the applied load, N; *c* is the crack length from the center of the imprint to the crack end, m.

We used an SSHOL 1.1,6/12-M3 electric furnace (Tula-Therm, Russia) at 1200 °C for 180 min to study the chemical kinetics and oxidation of a box-shaped (Ta, Hf)CN shape. The samples were measured using a micrometer. Before the analysis, the samples were polished on a Tegramin grinding and polishing system (Struers, Denmark). The sample was placed on a platform in the furnace in an alundum crucible. The degree of oxidation was assessed after 5, 10. 15, 20, 30, 60, 120, and 180 min using the gravimetric method. We measured the weight gain using a GR-202 analytical balance (AND, Japan), 10^{-4} g accuracy. Before weighing, the samples and with crucibles were cooled to room temperature.

Results and discussion

Mechanical activation (MA) is an important step before SHS. It enhances reactivity and helps control the microstructure of the combustion products [16]. Fig. 1 shows that the MA of tantalum, hafnium, and carbon powders (Ta + Hf + C) for 60 min resulted in formation of composite Ta/Hf/C particles ranging from 1 to 20 μm. A detailed examination of their cross sections identified the layers (Fig. 1, *b* and *c*) corresponding to heavy (Ta and Hf: light areas) and light (C: dark areas) elements.

Fig. 2 shows the (Ta, Hf)CN microstructure after SHS of a mechanically activated Ta + Hf + C mixture in a nitrogen environment. The morphology of SHS powder particles (Fig. 2, *a*) is identical to that of the composite Ta/Hf/C particles after MA (see Fig. 1, *a*). Cross-sectional analysis of (Ta, Hf)CN particles discovered pores and caverns. A more detailed examination revealed melted grains from 1 to 3 μm (Fig. 2, *b*). This can be explained by hafnium and tantalum melting during combustion (adiabatic combustion temperature t_{ad} = 3073 °C) and the formation of (Ta, Hf)CN through the liquid phase. As Fig. 2, *c* shows, Ta, Hf, C, and N are evenly distributed after SHS.

Chemical analysis indicated that the SHS powder contains 3.7 wt.% C and 2.2 wt.% N, which corresponds to $Hf_{0.75}Ta_{0.25}C_{0.5}N_{0.25}$. It should be noted that the oxygen content does not exceed 0.8 wt. %.

Fig. 3 shows the sample XRD patterns after SHS and spark plasma sintering (SPS). The crystal structure of the sintered (Ta, Hf)CN substance is identical to that of the synthesized powder. Its space group is *Fm*3*m* (225). However, after sintering, the main phase peaks became more symmetrical, indicating a homogenization of the chemical composition across the sample during SPS. The (Ta, Hf)CN lattice parameter after SHS and SPS is 0.455 nm. This is between HfC (0.464 nm) and HfN (0.453 nm). The value we obtained is higher than that for TaC (0.446 nm) and TaN (0.434 nm). In both cases, the XRD patterns show HfO_2 peaks of the *P*42/*nmc* (14) space group.

Fig. 4 shows a typical microstructure of the sample after sintering. The grain size of the main (Ta, Hf)CN phase (light areas) varies from 3 to 5 μm, with small HfO_2 inclusions (dark gray areas) at their boundaries. The sintered (Ta, Hf)CN powder has a 98.2 ± 0.3 % relative density and high mechanical properties (hardness *H* = 19.8 ± 0.2 GPa, Young's modulus *E* = 570 ± ± 20 GPa, fracture toughness K_{1c} = 5.4 ± 0.4 MPa·m$^{1/2}$). This is comparable to the properties of similar materials [11, 17—19].

We studied the kinetics and oxidation mechanism of the $Hf_{0.75}Ta_{0.25}C_{0.5}N_{0.25}$ using a muffle electric furnace at 1200 °C for 180 min. Fig. 5 shows the kinetic curve of the sample mass change. The oxidation of tantalum-hafnium carbonitride follows a parabo-

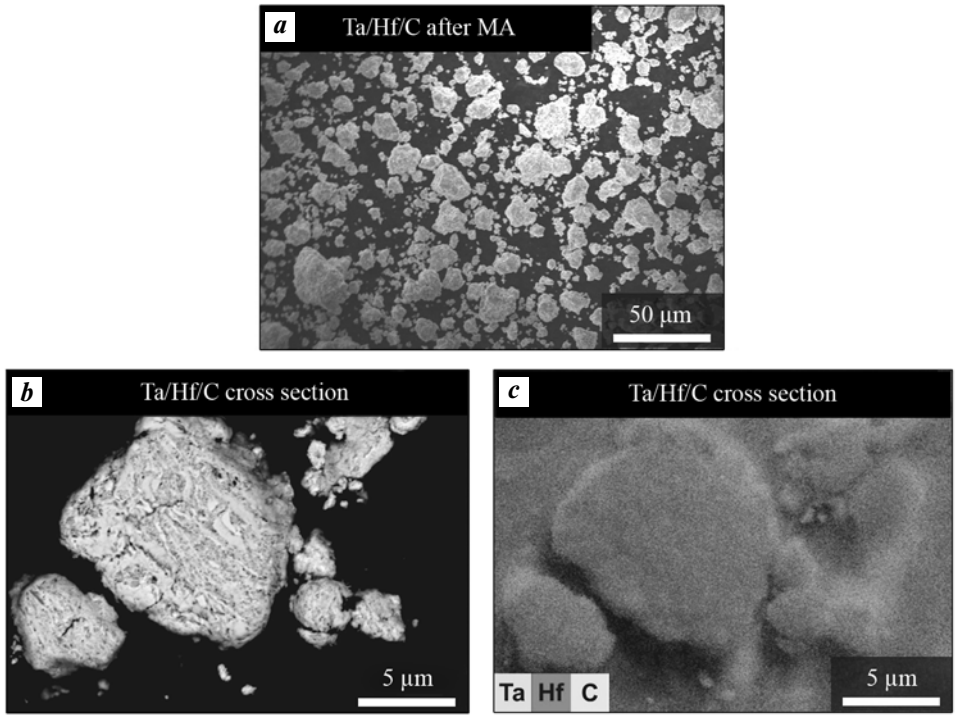

Fig. 1. Micrograph (***a***), cross section (***b***) of Ta/Hf/C composite particles and map of element distribution after mechanical activation (***c***)

Рис. 1. Микрофотография (***a***), поперечное сечение (***b***) композиционных частиц Ta/Hf/C и карта распределения элементов после механического активирования (***c***)

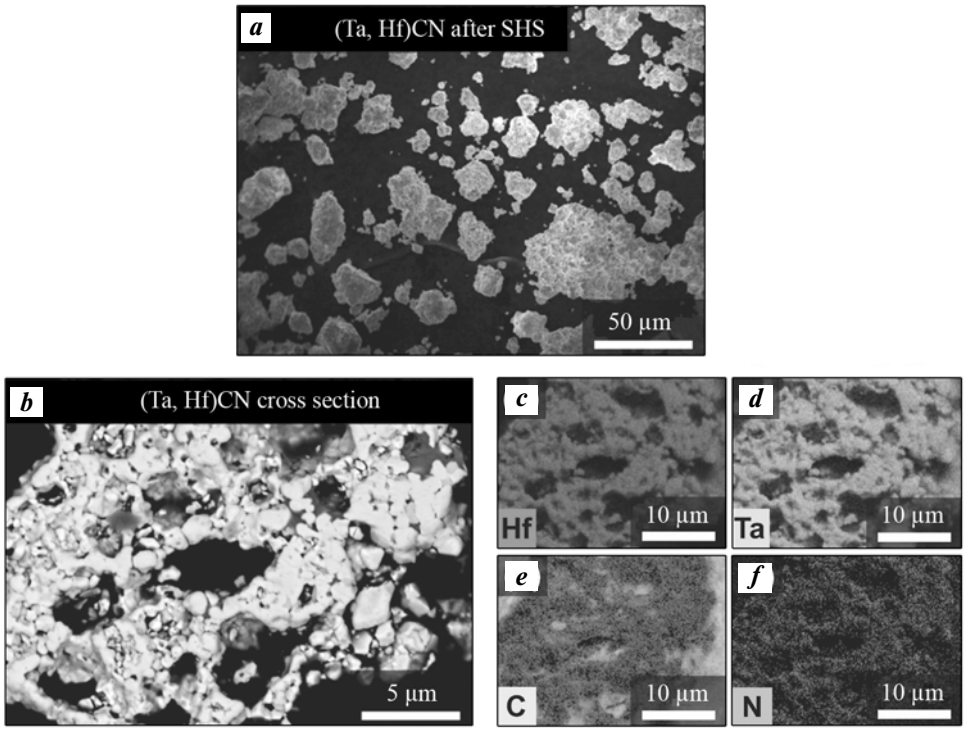

Fig. 2. Micrograph (***a***), cross section (***b***) of (Ta,Hf)CN particles and distribution of elements after SHS (***c***–***f***)

Рис. 2. Микрофотография (***a***), поперечное сечение (***b***) частиц (Ta,Hf)CN и распределение элементов после СВС (***c***–***f***)

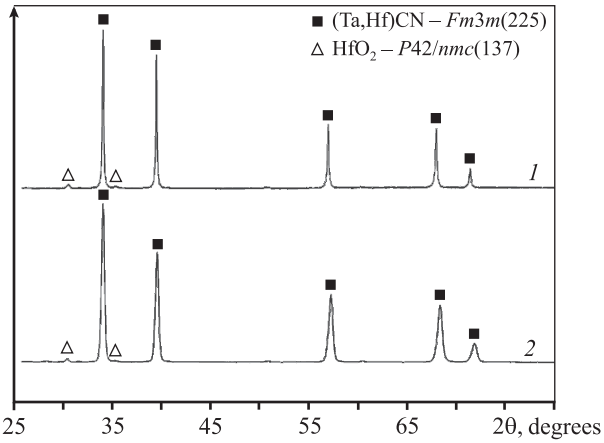

Fig. 3. XRD patterns of (Ta,Hf)CN samples after SPS (***1***) and SHS (***2***)

Рис. 3. Дифрактограммы образцов (Ta,Hf)CN после ИПС (***1***) и СВС (***2***)

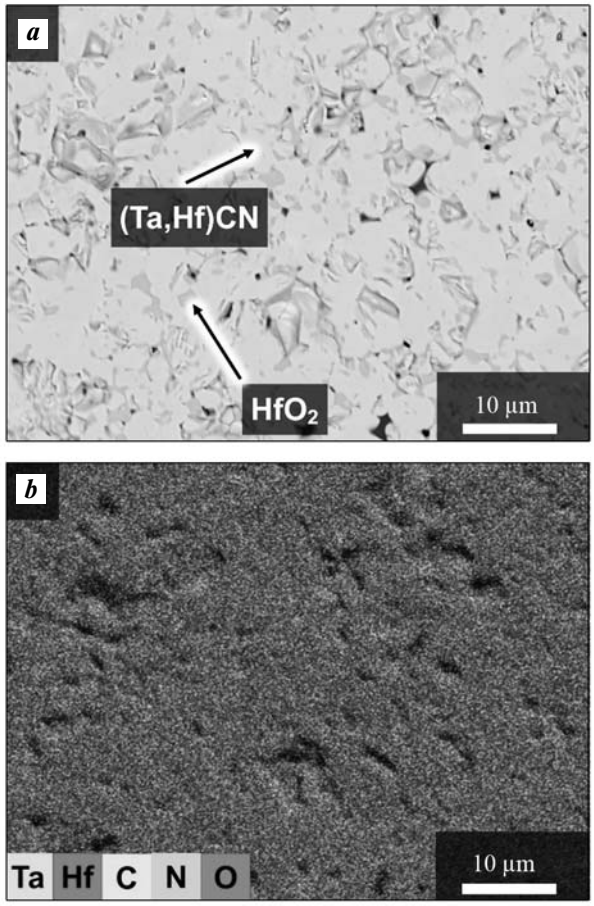

Fig. 4. Microstructure of sample (Ta,Hf)CN (***a***) and map of element distribution after SPS (***b***)

Рис. 4. Микроструктура образца (Ta,Hf)CN (***a***) и карта распределения элементов после ИПС (***b***)

lic law. Between 0 and 30 minutes, the max oxidation rate was 0.012 mg/(cm^2·s); as the oxide layer grew, it decreased to 0.004 mg/(cm^2·s). The average oxidation rate was ~0.006 mg/(cm^2·s) and the weight gain was 62 mg/cm^2.

As Fig. 6 shows, a dense oxide layer is formed on the surface of the $Hf_{0.75}Ta_{0.25}C_{0.5}N_{0.25}$ sample after oxidation. XRD indicated (Fig. 7) that it consists of two phases: monoclinic HfO_2, $P2_1/c(14)$ space group; and the $Hf_6Ta_2O_{17}$ orthorhombic superstructure (*Ima*2(46)). The intensity of the complex oxide peaks is much greater than that of hafnium oxide. It indicates the predominance of $Hf_6Ta_2O_{17}$ in the oxide layer.

Based on the results presented in this work and the literature [24], we may assume the following oxidation process (Fig. 8). Initially, Ta_2O_5 and HfO_2 are formed on the surface of (Ta, Hf)CN grains as result of the reaction

$$8Hf_{0,75}Ta_{0,25}C_{0,5}N_{0,25} + 14{,}5O_2 =$$

$$= Ta_2O_5 + 6HfO_2 + 4CO_2 + 2NO_2. \qquad (2)$$

The $Hf_{0.75}Ta_{0.25}C_{0.5}N_{0.25}$ compound has a high Hf content, so mainly HfO_2 is formed on the surface of the particles. Since the Gibbs energy for the Ta_2O_5 formation (ΔG = –72 kJ/mol [20]) is more negative when compared to that for HfO_2 (ΔG = –1088 kJ/mol [21]), Ta_2O_5 is most probably located at the surface of

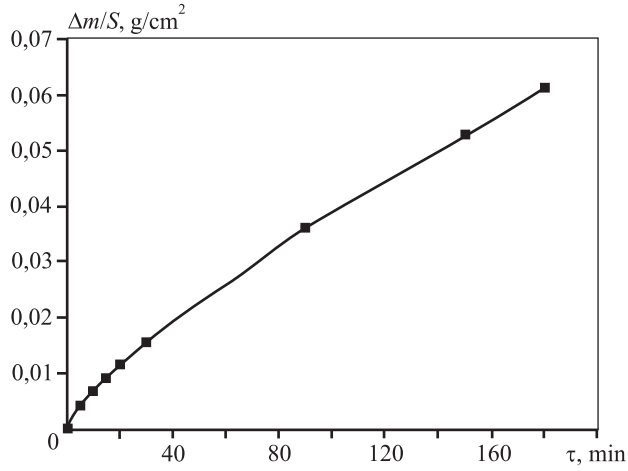

Fig. 5. Kinetic curve of (Ta,Hf)CN sintered sample oxidation

Рис. 5. Кинетическая кривая окисления спеченного образца (Ta,Hf)CN

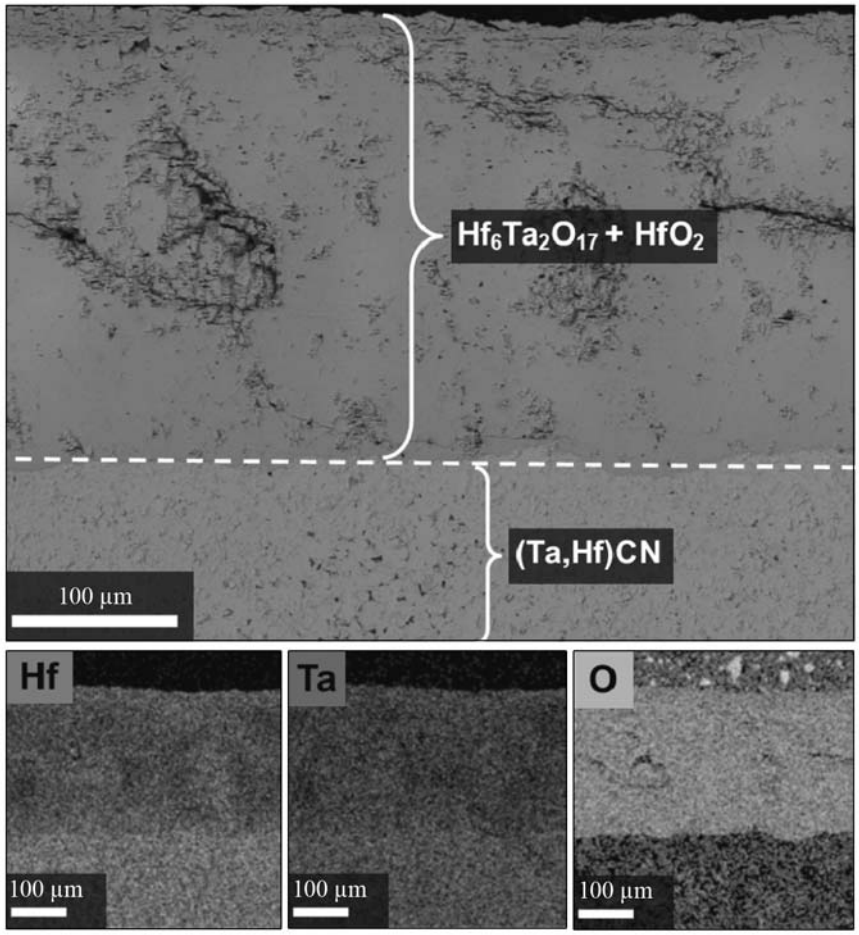

Fig. 6. Micrograph of (Ta,Hf)CN cross section after oxidation at t = 1200 °C and distribution of elements in oxide layer

Рис. 6. Микрофотография поперечного сечения образца (Ta,Hf)CN после окисления при t = 1200 °C и распределение элементов в оксидном слое

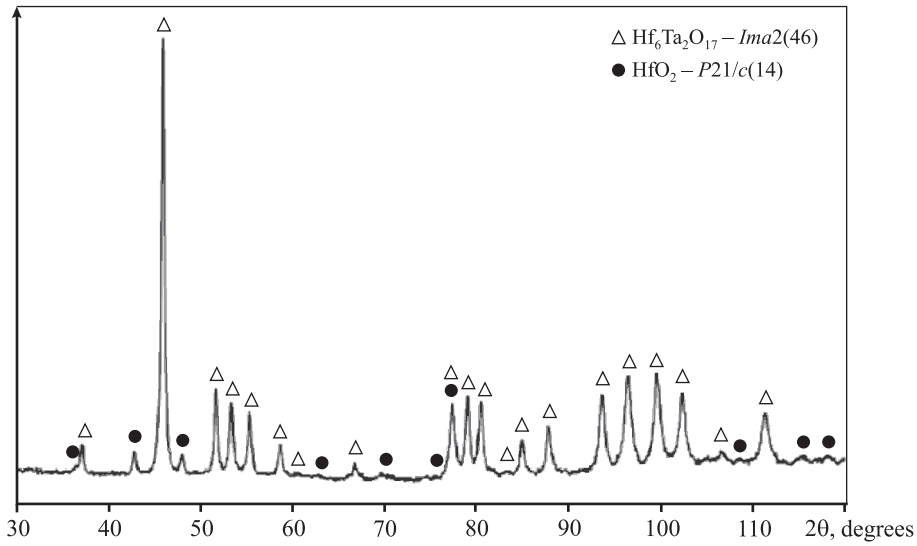

Fig. 7. XRD pattern of (Ta,Hf)CN oxide layer

Рис. 7. Дифрактограмма оксидного слоя (Ta,Hf)CN

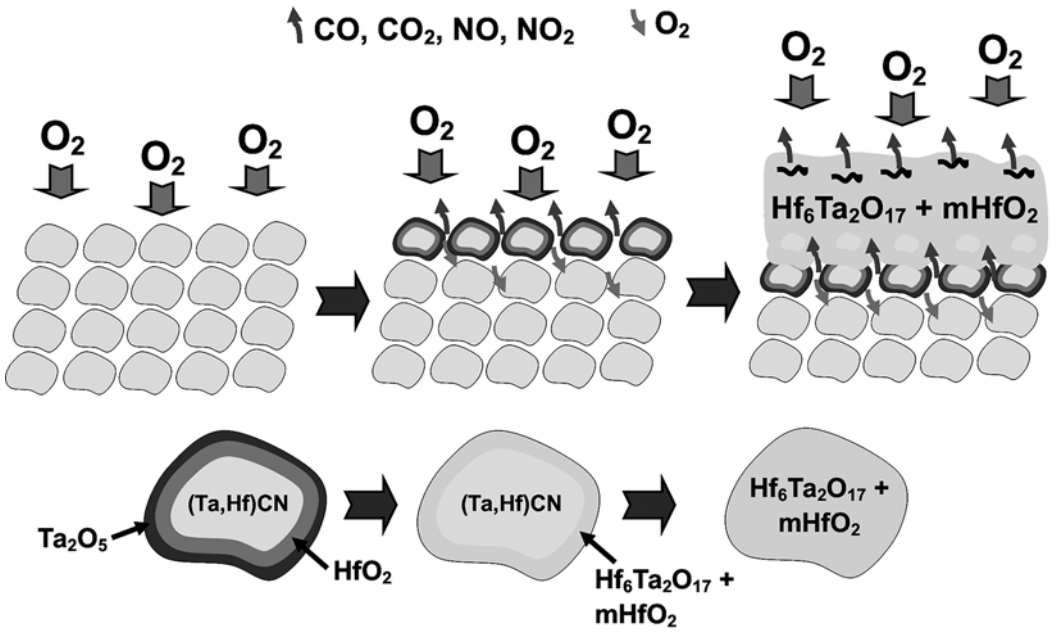

Fig. 8. (Ta,Hf)CN oxidation mechanism

Рис. 8. Механизм окисления (Ta,Hf)CN

HfO_2, as shown in Fig. 8. The phase diagram [22] indicates that HfO_2 and Ta_2O_5 oxides mutually react at t = 1200 °C to form $Hf_6Ta_2O_{17}$ and a monoclinic HfO_2 substance:

$$7HfO_2 + Ta_2O_5 = Hf_6Ta_2O_{17} + HfO_2. \quad (3)$$

Gaseous CO_2 and NO_2 are generated during the (Ta, Hf)CN oxidation (reaction (2)). The gases pass through the oxide layer, forming pores and cracks.

From studies [23, 24] we can conclude that $Hf_6Ta_2O_{17}$ as an oxide layer has a lower oxygen diffusion rate compared to HfO_2, high density, and adhesion to the substrate. It explains the relatively low oxidation rate of (Ta, Hf)CN.

Conclusion

An SHS process applied to a mechanically activated Ta + Hf + C mixture produces a $Hf_{0.75}Ta_{0.25}C_{0.5}N_{0.25}$ single-phase non-stoichiometric tantalum-hafnium carbonitride powder. Mechanical activation contributed to the uniform distribution of elements and the formation of composite Ta/Hf/C particles. SHS produces spongy particles consisting of submicron grains.

The SPS process at t = 2000 °C, 50 MPa and 20 min holding time produces bulk tantalum-hafnium carbonitride with 98.2 ± 0.3 % relative density, 19.8 ± 0.2 GPa hardness, 570 ± 20 GPa Young's modulus, and 5.4 ± ± 0.4 MPa·$m^{1/2}$ fracture toughness. The mechanical properties of the resulting ceramics are higher than those of binary compounds. They are comparable to double carbides.

The tantalum-hafnium carbonitride demonstrated high oxidation resistance (0.006 mg/(cm^2·s)) at t = 1,200 °C in the air. The oxidation kinetics follows the parabolic law. This can be explained by the formation of an oxide film with a low oxygen diffusion rate. The film consists of the $Hf_6Ta_2O_{17}$ homologous superstructure and the HfO_2 monoclinic substance.

Acknowledgments: *The research was funded by Russian Science Foundation Grant № 19-79-10280.*

Работа выполнена при финансовой поддержке гранта РНФ № 19-79-10280.

References

1. *Fahrenholtz W.G., Wuchina E.J., Lee W.E., Zhou Y.* Ultra-high temperature ceramics: materials for extreme environment applications. N.Y.: John Wiley & Sons, 2014.
2. *Vorotilo S., Sidnov K., Kurbatkina V.V., Loginov P.A., Patsera E.I. Sviridova T.A., Lobova T.A., Levashov E.A., Klechkovskayaet V.V.* Super-hardening and localized

plastic deformation behaviors in ZrB_2—TaB_2 ceramics. *J. Alloys Compd.* 2022. Vol. 901. P. 163368. DOI: 10.1016/j.jallcom.2021.163368.

3. *Ushakov S.V., Navrotsky A., Hong Q. J., van de Walle A.* Carbides and nitrides of zirconium and hafnium. *Materials.* 2019. Vol. 12. Iss. 17. P. 2728. DOI: 10.3390/ma12172728.
4. *Sheindlin M., Falyakhov T., Petukhov S., Valyano G., Vasin A.* Recent advances in the study of high-temperature behaviour of non-stoichiometric TaC_x, HfC_x and ZrC_x carbides in the domain of their congruent melting point. *Adv. Appl. Ceram.* 2018. Vol. 117. Iss. 1. P. s48—s55. DOI: 10.1080/17436753.2018.1510819.
5. *Aritonang S., Ezha Kurniasari W. S., Juhana R., Herawan T.* Analyzing tantalum carbide (TaC) and hafnium carbide (HfC) for spacecraft material. In: *Recent trends in manufacturing and materials towards industry 4.0.* Singapore, Springer, 2021. P. 925—933. DOI: 10.1007/978-981-15-9505-9_81.
6. *Shimada S.* Interfacial reaction on oxidation of carbides with formation of carbon. *Solid State Ionics.* 2001. Vol. 141. P. 99—104. DOI: 10.1016/S0167-2738(01)00727-5.
7. *Sevastyanov V.G., Simonenko E.P., Gordeev A.N., Simonenko N.P., Kolesnikov A.F., Papynov E.K., Shichalin O.O., Avramenko V.A., Kuznetsov N.T.* Behavior of a sample of the ceramic material HfB_2—SiC (45 vol.%) in the flow of dissociated air and the analysis of the emission spectrum of the boundary layer above its surface. *Russ. J. Inorg. Chem.* 2015. Vol. 60. Iss. 11. P. 1360—1373. DOI: 10.1134/S0036023615110133.
8. *Potanin A.Yu., Astapova A.N., Pogozhev Yu.S., Rupasov S.I., Shvyndina N.V., Klechkovskaya V.V., Levashov E.A., Timofeev I.A., Timofeev A.N.* Oxidation of HfB_2—SiC ceramics under static and dynamic conditions. *J. Eur. Ceram. Soc.* 2021. Vol. 41. Iss. 16. P. 34—47. DOI: 10.1016/j.jeurceramsoc.2021.09.018.
9. *Zhang C., Boesl B., Agarwal A.* Oxidation resistance of tantalum carbide-hafnium carbide solid solutions under the extreme conditions of a plasma jet. *Ceram. Int.* 2017. Vol. 43. Iss. 17. P. 14798—14806. DOI: 10.1016/j.ceramint.2017.07.227.
10. *Savvatimskiy A.I., Onufriev S.V., Muboyadzhyan S.A.* Thermophysical properties of the most refractory carbide $Ta_{0.8}Hf_{0.2}C$ under high temperatures (2000—5000 K). *J. Eur. Ceram. Soc.* 2019. Vol. 39. Iss. 4. P. 907—914. DOI: 10.1016/j.jeurceramsoc.2018.11.030.
11. *Kurbatkina V.V., Patsera E.I., Levashov E.A., Vorotilo S.* SHS processing and consolidation of Ta—Ti—C, Ta—Zr—C, and Ta—Hf—C carbides for ultra—high—temperatures application. *Adv. Eng. Mater.* 2018. Vol. 20. Iss. 8. P. 1701075. DOI: 10.1002/adem.201701075.
12. *Hong Q.J., Van De Walle A.* Prediction of the material with highest known melting point from ab initio molecular dynamics calculations. *Phys. Rev. B.* 2015. Vol. 92. Iss. 2. P. 020104. DOI: 10.1103/PhysRevB.92.020104.
13. *Сеплярский Б.С., Брауэр Г.Б., Тарасов А.Г.* Закономерности горения «безгазовой» системы Ti + 0,5C в спутном потоке азота. *Физика горения и взрыва.* 2011. No. 3. С. 52—59.

    Seplyarskii B.S., Brauer G.B., Tarasov A.G. Combustion of the gasless system Ti + 0.5C in a nitrogen coflow. *Fizika goreniya i vzryva.* 2011. Vol. 3. P. 52—59 (In Russ.).
14. ГОСТ 20018-74 (СТ СЭВ 1253-78, ИСО 3369-75) Сплавы твердые спеченные. Метод определения плотности (с изменениями № 1, 2, 3). М.: Изд-во стандартов, 1991.

    GOST 20018-74 (ST SEV 1253-78, ISO 3369-75) Sintered hard alloys. Density determination method. Moscow: Izdatel'stvo standartov, 1991 (In Russ.).
15. ГОСТ 2999—75. Металлы и сплавы. Метод измерения твердости по Виккерсу (с изм. 1, 2). Управление стандартизации и сертификации сырья и материалов. Изд-во стандартов, 1986.

    GOST 2999—75. Metals and alloys. Vickers hardness measurement method. reissue. Management of standardization and certification of raw materials and materials. Moscow: Izdatel'stvo standartov, 1986 (In Russ.).
16. *Mukasyan A.S., Rogachev A.S.* Combustion synthesis: mechanically induced nanostructured materials. *J. Mater. Sci.* 2017. Vol. 52. P. 11826—11833. DOI: 10.1007/s10853-017-1075-9.
17. *Ghaffari S.A., Faghihi-Sani M.A., Golestani-Fard F., Mandal H.* Spark plasma sintering of TaC—HfC UHTC via disilicides sintering aids. *J. Eur. Ceram. Soc.* 2013. Vol. 33. Iss. 8. P. 1479—1484. DOI: 10.1016/j.jeurceramsoc.2013.01.017.
18. *Cedillos-Barraza O., Grasso S., Al Nasiri N., Jayaseelan D.D., Reece M.J., Lee W.E.* Sintering behaviour, sol-

id solution formation and characterisation of TaC, HfC and TaC—HfC fabricated by spark plasma sintering. *J. Eur. Ceram. Soc*. 2016. Vol. 36. Iss. 7. P. 1539—1548. DOI: 10.1016/j.jeurceramsoc.2016.02.009.

19. *Zhang C., Gupta A., Seal S., Boesl B., Agarwal A*. Solid solution synthesis of tantalum carbide—hafnium carbide by spark plasma sintering. *J. Amer. Ceram. Soc*. 2017. Vol. 100. Iss. 5. P. 1853—1862. DOI: 10.1111/jace.14778.
20. *Ivanov M.V., Perevalov T.V., Aliev V.S., Gritsenko V.A., Kaichev V.V.* Electronic structure of δ-Ta_2O_5 with oxygen vacancy: ab initio calculations and comparison with experiment. *J. Appl. Phys*. 2011. Vol. 110. Iss. 2. P. 024115. DOI: 10.1063/1.3606416.
21. *Fang Q., Zhang J.-Y., Wang Z., Modreanu M., O'Sullivan B.J., Hurley P.K., Leedham T.L., Hywel D., Audier M.A., Jimenez C., Senateur J.-P. Ian W. Boyda*. Interface of ultrathin HfO_2 films deposited by UV-photo-CVD. *Thin Solid Films*. 2004. Vol. 453. P. 203—207. DOI: 10.1016/j.tsf.2003.11.186.
22. *McCormack S.J., Tseng K.P., Weber R.J., Kapush D., Ushakov S.V., Navrotsky A., Kriven W.M*. In-situ determination of the HfO_2—Ta_2O_5-temperature phase diagram up to 3000 °C. *J. Amer. Ceram. Soc*. 2019. Vol. 102. Iss. 11. P. 7028—7030. DOI: 10.1111/jace.16271.
23. *Yang Y., Perepezko J. H., Zhang C*. Oxidation synthesis of $Hf_6Ta_2O_{17}$ superstructures. *Mater. Chem. Phys*. 2017. Vol. 197. P. 154—162. DOI: 10.1016/j.matchemphys.2017.04.055.
24. *Zhang C., Boesl B., Agarwal A*. Oxidation resistance of tantalum carbide-hafnium carbide solid solutions under the extreme conditions of a plasma jet. *Ceram. Int*. 2017. Vol. 43. Iss. 17. P. 14798—14806. DOI: 10.1016/j.ceramint.2017.07.227.

UDC 666.3 + 544.01
DOI dx.doi.org/10.17073/1997-308X-2022-3-55-62

Refinement of the eutectic composition in the LaB_6–VB_2 system

© 2022 г. **E.S. Novoselov**[1], **V.I. Almjashev**[2], **D.D. Nesmelov**[1], **D.P. Danilovich**[1]

[1] Saint-Peterburg State Institute of Technology (SPSIT), Saint-Petersburg, Russia

[2] Alexandrov NITI, Leningrad Region, Sosnovy Bor, Russia

Received 29.04.2022, revised 14.07.2022, accepted for publication 18.07.2022

Abstract: The LaB_6–VB_2 alloy with the eutectic structure was obtained by cold crucible induction melting followed by crystallization. The mole ratio of components in the initial powder mixture was 35 : 65. The structure and composition of the LaB_6–VB_2 material were studied by *X*-ray diffraction, scanning electron microscopy, and *X*-ray microanalysis. The composition of the alloy is represented by two boride phases — cubic LaB_6 and hexagonal VB_2. Two-phase eutectic regions up to 500 μm in size represent a LaB_6 matrix filled with 0.8–2.0 μm thick VB_2 fibers (filamentary, rod crystals). VB_2 fibers are predominantly oriented along the direction of the temperature gradient that appeared when cooling the melt, i.e. from the outer surface of the sample to its center. The integrated phase area analysis was used to determine the eutectic composition: 42 ± 1 mol% LaB_6 and 58 ± 1 mol% VB_2.

Keywords: lanthanum hexaboride, vanadium diboride, eutectic, cold crucible method, anisotropy.

Novoselov E.S. – Engineer, Department of chemical technology of high-melting and silicate materials (CTHSM), Saint-Peterburg State Institute of Technology (SPSIT) (190013, Russia, Saint-Petersburg, Moskovskii pr., 26). E-mail: lehmann330@gmail.com.

Almjashev V.I. – Head of the Severe Accidents Research Department, Alexandrov NITI (188540, Russia, Leningrad Reg., Sosnovyj Bor, Koporskoe sh., 72). E-mail: vac@mail.ru.

Nesmelov D.D. – Associated professor, Department of CTHSM, SPSIT. E-mail: dnesmelov@yandex.ru.

Danilovich D.P. – Associated professor, Department of CTHSM, SPSIT. E-mail: dmitrydanilovich@gmail.com.

For citation: *Novoselov E.S., Almjashev V.I., Nesmelov D.D., Danilovich D.P.* Refinement of the eutectic composition in the LaB_6–VB_2 system. *Izvestiya Vuzov. Poroshkovaya Metallurgiya i Funktsional'nye Pokrytiya (Powder Metallurgy and Functional Coatings)*. 2022. Vol. 16. No. 3. P. 55–62 (In Russ.). DOI: dx.doi.org/10.17073/1997-308X-2022-3-55-62.

Уточнение эвтектического состава в системе LaB_6–VB_2

Е.С. Новоселов[1], **В.И. Альмяшев**[2], **Д.Д. Несмелов**[1], **Д.П. Данилович**[1]

[1] Санкт-Петербургский государственный технологический институт (технический университет) (СПбГТИ (ТУ)), г. Санкт-Петербург, Россия

[2] Научно-исследовательский технологический институт (НИТИ) им. А.П. Александрова, г. Сосновый Бор, Ленинградская обл., Россия

Статья поступила в редакцию 29.04.2022 г., доработана 14.07.2022 г., подписана в печать 18.07.2022 г.

Аннотация: Сплав с эвтектической структурой системы LaB_6–VB_2 был получен индукционной плавкой методом холодного тигля с последующей кристаллизацией. Мольное соотношение компонентов в исходной порошковой смеси составляло 35 : 65. Методами рентгеновской дифракции, сканирующей электронной микроскопии и микрорентгеноспектрального анализа исследованы структура и состав материала LaB_6–VB_2. Состав сплава представлен двумя фазами боридов – кубическим LaB_6 и гексагональным VB_2. Двухфазные эвтектические области размером до 500 мкм представляют собой

матрицу LaB_6, наполненную волокнами VB_2 (нитевидными, стержневыми кристаллами) толщиной 0,8–2,0 мкм, которые преимущественно ориентированы вдоль направления температурного градиента, возникшего при охлаждении расплава, т.е. от внешней поверхности образца к его центру. С помощью метода анализа интегральной площади фаз установлен состав эвтектики: 42 ± 1 мол. % LaB_6 и 58 ± 1 мол. % VB_2.

Ключевые слова: гексаборид лантана, диборид ванадия, эвтектика, метод холодного тигля, анизотропия.

Новоселов Е.С. – инженер кафедры химической технологии тугоплавких неметаллических и силикатных материалов (ХТТНСМ), СПбГТИ (ТУ) (190013, г. Санкт-Петербург, Московский пр-т, 26).
E-mail: lehmann330@gmail.com.

Альмяшев В.И. – начальник отдела исследований тяжелых аварий, НИТИ им. А.П. Александрова (188540, Ленинградская обл., г. Сосновый Бор, Копорское шоссе, 72).
E-mail: vac@mail.ru.

Несмелов Д.Д. – доцент кафедры ХТТНСМ, СПбГТИ (ТУ).
E-mail: dnesmelov@yandex.ru.

Данилович Д.П. – доцент кафедры ХТТНСМ, СПбГТИ (ТУ).
E-mail: dmitrydanilovich@gmail.com.

Для цитирования: *Новоселов Е.С., Альмяшев В.И., Несмелов Д.Д., Данилович Д.П.* Уточнение эвтектического состава в системе LaB_6–VB_2. *Известия вузов. Порошковая металлургия и функциональные покрытия.* 2022. Т. 16. No. 3. С. 55–62. DOI: dx.doi.org/10.17073/1997-308X-2022-3-55-62.

Introduction

Materials using quasi-binary systems containing rare-earth metal hexaborides (primarily LaB_6) and transition metal diborides (MB_2, where M can be Ti, Zr, Hf, Ta, Nb, V, Cr, W, and Mo) have been the focus of research for decades due to their outstanding thermal emission properties [1—4]. When compared to poly- or single-crystal LaB_6 commonly used for making thermal emission cathodes, materials based on LaB_6—MB_2 eutectic systems have a lower work function and higher emission current density at the same operating temperature. Studies [2, 5, 6] show that the cathode manufacturing process significantly affects its thermal emission properties: directionally crystallized cathodes made from LaB_6—VB_2 and LaB_6—ZrB_2 systems have higher emission currents than their sintered polycrystalline analogs. The directionally crystallized cathode materials manufactured by zone melting have a two-phase structure. The LaB_6 matrix phase is regularly «reinforced» by rod-like or plate crystals of the diboride phase.

Better thermal emission properties associated with the formation of such a structure are of great importance for thermocathode materials. There is also another effect applicable to a wider range of materials. It occurs in directionally crystallized materials made from LaB_6—MB_2 systems and results in a significant increase in their physical and mechanical properties compared to their monocrystalline and sintered analogs [7—13].

In order to create materials using LaB_6—MB_2 eutectic systems, reliable data on the phase equilibria in such systems, their composition, and eutectic temperature are required [14—23]. Experimental measurements of these properties in high-temperature oxygen-free systems are technically challenging, so the available literature is sparse. Furthermore, such data has to be verified, since it was obtained using outdated techniques. For example, [14, 15] report contradictory eutectic properties for LaB_6 and VB_2. A possible reason is a molar to a mass concentration conversion error.

This study aims to obtain a more precise eutectic composition of the LaB_6—VB_2 system experimentally. Another goal is to make eutectic compositions by induction melting without special directional crystallization equipment. It is of practical interest since industrial-grade induction melting is more affordable compared with zone melting. In contrast, induction melting does not guarantee identical temperature gradients across the material volume. Therefore, the assessment of the structure regularity (when a continuous eutectic structure or individual eutectic regions with different orientations are formed) is of particular interest.

Methods

We made lanthanum and vanadium borides by means of the borothermal reduction of oxides using commercially available La_2O_3 (99.99 % purity), V_2O_5 (99.0 %), and amorphous boron (99.0 %) powders. A vacuum resistance furnace at 1650 °C (LaB_6) and 1200 °C (VB_2) was used. The isothermal hold time was 1 h at 10^{-1} Pa residual gas pressure.

The average particle size of the LaB_6 and VB_2 powders measured by laser diffraction was 5 to 10 μm. The powders contained only the target phases (cubic LaB_6 and hexagonal VB_2) without the initial components or any other crystalline phases. Elemental analysis indicated the presence of oxygen adsorbed at the particle surface, amounting to 1.2 wt.%. We used a UnionProcess HD-1 attritor (Union Process, USA) with silicon carbide grinding bodies for mixing and grinding the powders to a 1.5 μm average particle size for 6 h in the BR-1 solvent (gasoline). About 0.7 wt.% SiC was added to the mixture due to the wear of the grinding bodies.

The concentration of the mixture components was selected to match the eutectic point, as reported in [14, 15]. Ordanyan S. [14] specifies the molar content of VB_2 in the eutectic as 69 mol.%, which corresponds to 44 wt.% mass concentration of VB_2. However, according to [14, 15] the mass content of VB_2 is 40 wt.%. This discrepancy may be a result of a concentration conversion error in [14], so we opted for a VB_2 40 wt.% (65 mol.%) experimental mixture.

After drying, the powder was compacted into cylinders 40 mm dia. and 40 mm high using a hydraulic press. Rasplav 2 and Rasplav 3 furnaces (made in Russia) were used for induction melting of the samples We applied the cold-crucible technology in an argon flow described in [22].

The resulting crystallized ingot was cut in two mutually perpendicular directions using a diamond cutting disc.

The microstructure of the polished sections was analyzed with a Tescan Vega 3SBH scanning electron microscope (SEM) (Czech Republic).

We used a Rigaku SmartLab 3 multipurpose diffractometer (Japan) in the $2\theta = 10°\div80°$ angular range (CuK_α radiation, Ni filter, 0.01° scan step) for *X*-ray phase analysis of the initial components, powders, and crystallized alloys. The phase composition and lattice cell properties were estimated with the SmartLab Studio 3 software and the ICDD PDF-2 diffraction database.

The concentration of components in the eutectic alloy was estimated by means of three alternative methods:

— SEM-EDX elemental composition analysis with an Aztec X-Act X-ray energy dispersive spectroscopy analyzer (Oxford Instruments, UK);

— FP XRD analysis with the SmartLab Studio 3 software;

— IAP was applied to the SEM images of the polished sections using the Thixomet Lite software package (Russia).

Results and discussion

Fig. 1 shows the results of the LaB_6—VB_2 crystallized alloy SEM analysis. The alloy consists mainly of extensive (up to 500 μm) two-phase eutectic regions where the hexagonal VB_2 fibers (filamentary, rod-like crystals extended along the C crystallographic axis) are located in the LaB_6 matrix (Fig. 1, *a*, *b*). The VB_2 fibers are predominantly oriented along the temperature gradient created during the melt cooling, i.e., from the outer surface of the sample to its central region. However, there are local deviations from the predominant direction (Fig. 1, *c*). The degree of structure regularity is lower than that of zone-melting materials [2—13] as was expected.

However, in comparison with the LaB_6—NbB_2—W_2B_5 alloy that we obtained earlier by electric arc melting [23], in the LaB_6—VB_2 made by the cold-crucible technology, the arrangement of the eutectic regions is more ordered. Depending on the melt local cooling rate, the diameter of the VB_2 fibers varies from 0.8 to 2.0 μm. Fibers over 2 μm tend to merge (Fig. 1, *d*). In some cases, probably where the specified concentration was disturbed due to imperfect mixing, large (up to 100 μm) single-phase VB_2 areas with prominent rounded contours were formed (Fig. 1, *e*). Besides the deviations in concentration, this could be caused by the presence of vanadium oxide impurities on the VB_2 surface preventing the contact interaction between La and V borides in the melt. Extended curved LaB_6 «films» (Fig. 1, *e*) up to 10 μm thick were also observed between some eutectic regions.

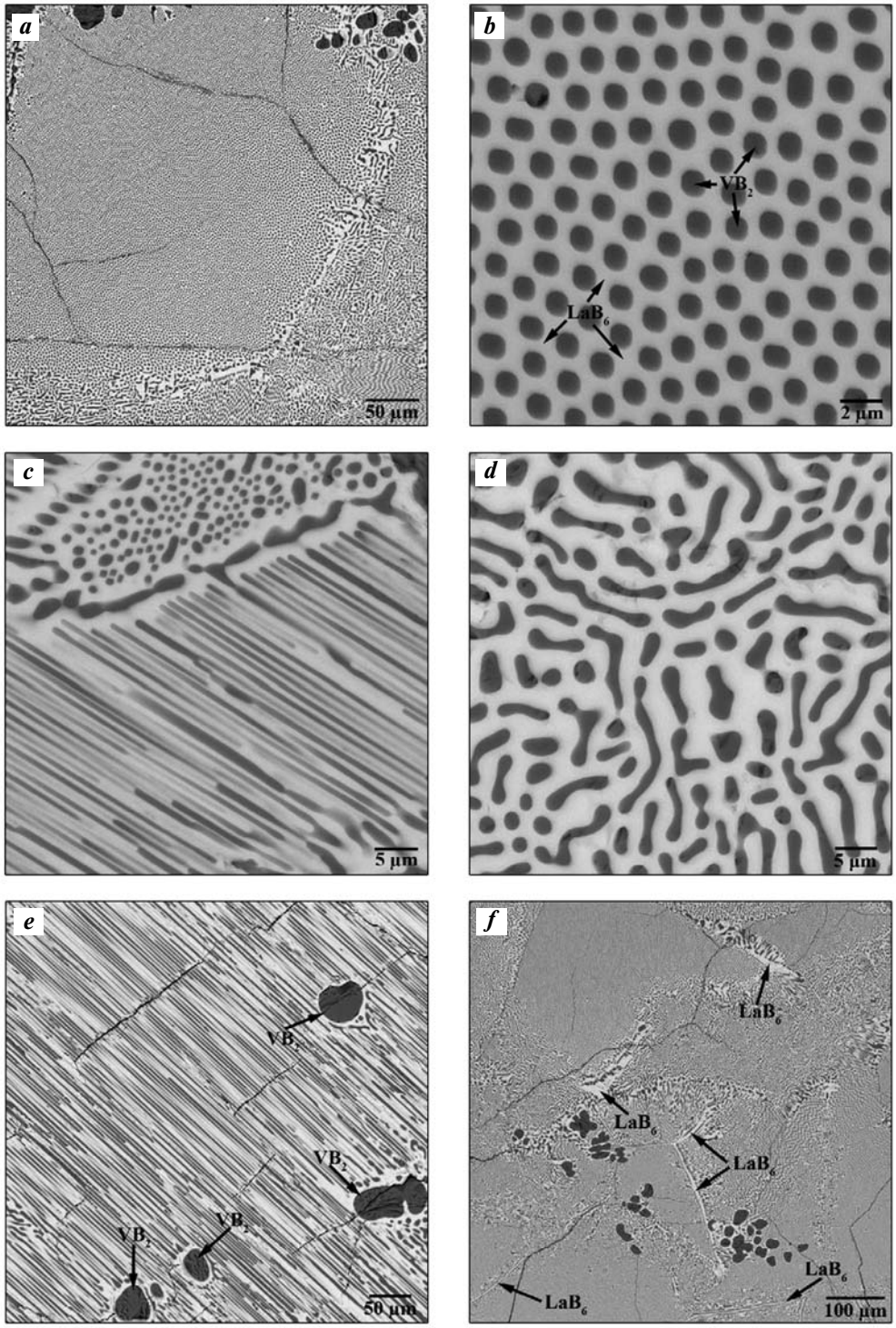

Fig. 1. LaB_6–VB_2 alloy structure (SEM)

a – general view of alloy structure; ***b*** – area of ordered quasibinary eutectic; ***c*** – area of quasibinary eutectic with different rod orientation; ***d*** – area of coarse conglomerate eutectic; ***e***, ***f*** – areas of quasibinary eutectic with large single-phase VB_2 and LaB_6 inclusions

Рис. 1. Структура сплава LaB_6–VB_2 (СЭМ)

a – общий вид структуры сплава; ***b*** – область упорядоченной квазибинарной эвтектики; ***c*** – область квазибинарной эвтектики с различной ориентацией стержней; ***d*** – область эвтектики грубого конгломерата; ***e***, ***f*** – области квазибинарной эвтектики с крупными однофазными включениями VB_2 и LaB_6

In addition to the eutectic areas, the alloy contains both VB_2 and LaB_6 crystallization areas. For this reason, we cannot identify whether the composition (eutectic, according to [14, 15]) is in the pre-eutectic or over-eutectic area of the LaB_6—VB_2 quasi-binary section.

X-ray phase analysis of the alloys confirmed their two-phase composition (Fig. 2). No crystalline phases except for hexagonal VB_2 and cubic LAB_6 were found. The XRD patterns of two mutually perpendicular sections in the crystallized alloys differ in the reflection intensity ratios for different families of lattice planes. It should be noted that the analyzed polished surfaces of *A* and *B* samples contain both transverse and longitudinal sections, and that the ratios of their areas were not equal. Furthermore, due to the above-noted direction of the alloy crystallization temperature gradients, the presence of eutectic regions oriented at arbitrary angles to the polished surface is inevitable.

The abnormally high intensity of (100) and (200) LaB_6 reflexes is strongly pronounced in the XRD pattern *B* in contrast to *A*, where there is a smaller excess over the peak (110) (see Fig. 2), and in which 100 % intensity is standard. For VB_2, we can note the anomalous intensity of the reflex (100) in pattern *B*. The deviations from the crystallographic standards can be explained by the anisotropic structure of the alloy and the preferential reflection from the corresponding lattice planes.

The LaB_6 and VB_2 phase lattice cell properties are close to their standard values (Table 1). Since there are no significant crystal lattice distortions, this confirms the opinion of S. Ordanyan [14, 15] that LaB_6 and VB_2 are insignificantly soluble in their solid state.

Table 2 lists the concentrations of eutectic alloy components estimated by EDX, IAP, and FP XRD. It also includes the data from [14, 15] for comparison.

The EDX method did not detect the oxygen impurity in the crystallized samples which we detected during the boride powder synthesis. This may be due to the fact that the oxygen was removed as volatile boron suboxide (B_2O_2) during the sample sintering and melting experiment. A silicon carbide impurity content reached 0.7 wt.% after co-milling of boride powders. It was found locally in the peripheral regions of the crystallized alloy. It can be attributed to the gravity separation of the melt since the phase densities are different.

Table 1. **Unit cell parameters of LaB_6 and VB_2 phases in the crystallized alloy**

Таблица 1. Параметры элементарной ячейки фаз LaB_6 и VB_2 в закристаллизованном сплаве

Phase	Experiment		Standard	
	a, Å	*c*, Å	*a*, Å	*c*, Å
LaB_6	4.1562 ± 0.0005	–	2.1569	–
VB_2	2.9974 ± 0.0005	3.0560 ± 0.0005	29976	3.0562

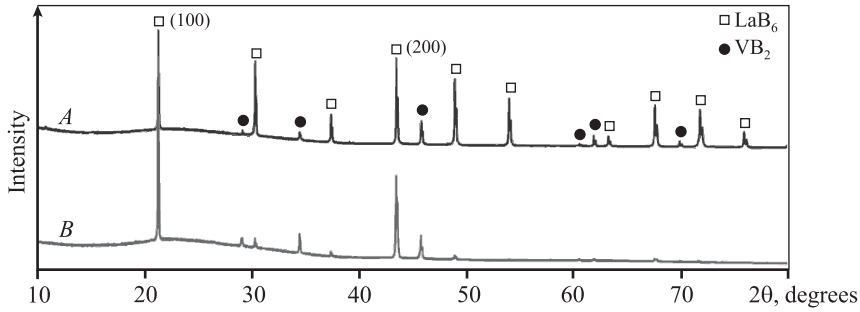

Fig. 2. XRD pattern of LaB_6–VB_2 alloy

A and *B* – polished sections with predominant content of transverse (*A*) and longitudinal (*B*) VB_2 fiber sections

Рис. 2. Дифрактограмма сплава LaB_6–VB_2

A и *B* – аншлифы с преимущественным содержанием поперечных (*A*) и продольных (*B*) сечений волокон VB_2

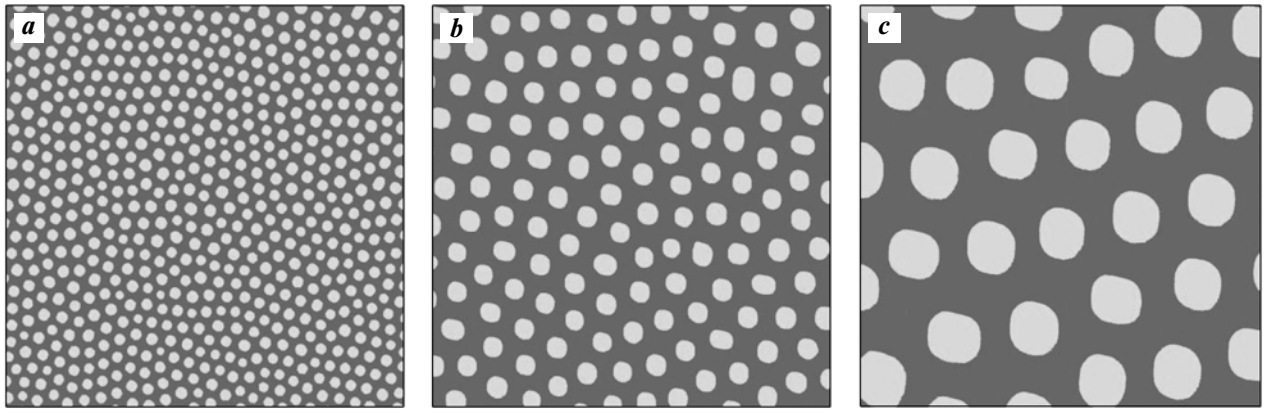

Fig. 3. Example of micrograph binarization for LaB_6–VB_2 alloy eutectic areas
a –×4500, ***b*** – ×12000, ***c*** – ×20000 magnification

Рис. 3. Пример бинаризации микрофотографий эвтектических областей сплава LaB_6–VB_2
a – увеличение 4500×, ***b*** – 12000×, ***c*** – 20000×

Table 2. **Contents of components (mol.%) in LaB_6–VB_2 eutectic alloy**

Таблица 2. Содержание компонентов (мол.%) в эвтектическом сплаве LaB_6–VB_2

Detection method	LaB_6	VB_2
IAP	42 ± 1	58 ± 1
EDX	38 ± 4	62 ± 4
FP XRD	35 ± 5	65 ± 5
From [14]	31	69
From [15]	35	65

X-ray analysis cannot selectively examine the sample surface. Thus the result characterizes the concentrations of components not only in the eutectic but also in large single-phase regions (see Fig. 1, *d*—*e*). This significantly reduces the accuracy of this method as applied to this problem. IAP and EDX methods can select a specific sample region, so they were used to directly analyze the eutectic regions. However, due to the large content of light boron atoms, the component concentration measurement error (MSE) for the EDX method is also high.

Twenty binarized micrographs of the eutectic regions with VB2 fiber cross sections from different sample sections were taken for multiple IAP measurements (Fig. 3). Statistical processing of the results indicated that the eutectic contains 42 mol.% of LaB_6 and 58 mol.% of VB_2 (1 % MSE).

Conclusion

As a result of the induction melting experiment and subsequent crystallization of the samples made from a mixture of LaB_6 and VB_2 boride powders, alloys with a clear eutectic structure were obtained. The two-phase eutectic regions up to 500 μm are an LaB_6 matrix filled with VB_2 fibers (filamentous, rod-shaped crystals) 0.8—2.0 μm thick. The VB_2 fibers are predominantly oriented along the melt cooling temperature gradient, i.e., from the outer surface to the center.

The alloys contain only two boride phases: cubic LaB_6; and hexagonal VB_2. *X*-ray methods detected no mutual solubility of the phases.

The comparison of the alloy component concentration measurements by different methods showed that IAP is best suited to measuring eutectic concentration components. The eutectic composition determined by IAP is as follows: 42 ± 1 mol.% of LaB6 and 58 ± ± 1 mol.% of VB2. The discrepancy with the published data is 11 mol.%. [14] and 7 mol.% [15].

Acknowledgments: *The research was funded by Russian Science Foundation Grant № 19-73-10180.*

Исследование выполнено при финансовой поддержке гранта РНФ № 19-73-10180.

References

1. *Paderno Y.B., Taran A.A., Voronovich D.A., Paderno V.N., Filipov V.B.* Thermionic properties of LaB_6—

$(Ti_{0,6}Zr_{0,4})B_2$ material. *Funct. Mater.* 2008. Vol. 15. No. 1. P. 63. http://dspace.nbuv.gov.ua/handle/123456789/137229.

2. *Taran A., Voronovich D., Oranskaya D. Filipov V., Podshyvalova O.* Thermionic emission of LaB_6—ZrB_2 quasi binary eutectic alloy with different ZrB_2 fibers orientation. *Funct. mater.* 2013. Vol. 20. No. 4. P. 485—488. DOI: 10.15407/fm20.04.485.
3. *Yang X., Wang P., Wang Z., Hu K., Cheng H., Li Z., Zhang J.* Microstructure, mechanical and thermionic emission properties of a directionally solidified LaB_6—VB_2 eutectic composite. *Mater. Design*. 2017. Vol. 133. P. 299—306. DOI: 10.1016/j.matdes.2017.07.069.
4. *Berger M.H., Back T.C., Soukiassian P., Martinotti D., Douillard L., Fairchild S.B., Boeckl J.J., Filipov V., Sayir A.* Local investigation of the emissive properties of LaB_6—ZrB_2 eutectics. *J. Mater. Sci.* 2017. Vol. 52. No. 10. P. 5537—5543. DOI: 10.1007/s10853-017-0816-0.
5. *Paderno Y.B., Taran A.A., Ostrovski E.K., Paderno V.N., Filippov V.B.* Manufacturing, structure and thermionic properties of lanthanum hexaboride based composite cathode materials. *Funct. mater.* 2001. Vol. 8. No. 4. P. 714—717.
6. *Taran A., Voronovich D., Plankovskyy S., Paderno V., Filippov V.* Review of LaB_6, Re—W dispenser and $BaHfO_3$—W cathode development. *IEEE Trans. Electr. Devic.* 2009. Vol. 56. No. 5. P. 760—765. DOI: 10.1109/TED.2009.2015615.
7. *Deng H., Dickey E.C., Paderno Y., Paderno V., Filippov V., Sayir A.* Crystallographic characterization and indentation mechanical properties of LaB_6—ZrB_2 directionally solidified eutectics. *J. Mater. Sci.* 2004. Vol. 39. No. 19. P. 5987—5994. DOI: 10.1023/B:JMSC.0000041695.40772.56.
8. *Bogomol I., Nishimura T., Vasylkiv O. Sakka Y., Loboda P.* High-temperature strength of directionally reinforced LaB_6—TiB_2 composite. *J. Alloys Compd.* 2010. Vol. 505. No. 1. P. 130—134. DOI: 10.1016/j.jallcom.2010.05.003.
9. *Volkova H., Filipov V., Podrezov Y.* The influence of Ti addition on fracture toughness and failure of directionally solidified LaB_6—ZrB_2 eutectic composite with monocrystalline matrix. *J. Eur. Ceram. Soc.* 2014. Vol. 34. No. 14. P. 3399—3405. DOI: 10.1016/j.jeurceramsoc.2014.03.018.
10. *Bogomol I., Nishimura T., Nesterenko Y., Vasylkiv O., Sakka Y., Loboda P.* The bending strength temperature dependence of the directionally solidified eutectic LaB_6—ZrB_2 composite. *J. Alloys Compd.* 2011. Vol. 509. No. 20. P. 6123—6129. DOI: 10.1016/j.jallcom.2011.02.176.
11. *Chen C.M., Zhang L.T., Zhou W.C.* Characterization of LaB_6—ZrB_2 eutectic composite grown by the floating zone method. *J. Cryst. Growth.* 1998. Vol. 191. No. 4. P. 873—878. DOI: 10.1016/S0022-0248(98)00358-3.
12. *Bogomol I., Loboda P.* Directionally solidified ceramic eutectics for high-temperature applications. In: *MAX Phases and ultra-high temperature ceramics for extreme environments*. 2013. P. 303. DOI: 10.4018/978-1-4666-4066-5.ch010.
13. *Soloviova T. O., Karasevska O. P., Loboda P. I.* Structure, residual stresses and mechanical properties of LaB_6—TiB_2 ceramic composites. *Ceram. Int.* 2019. Vol. 45. No. 7. P. 8677—8683. DOI:10.1016/j.ceramint.2019.01.189.
14. *Орданьян С.С.* О закономерностях взаимодействия в системах LaB_6—$Me^{IV–VI}B_2$. *Неорган. материалы*. 1988. Т. 24. No. 2. С. 235—238.
Ordan'yan S.S. About regulations of interaction in LaB_6—$Me^{IV–VI}B_2$ systems. *Neorgan. materialy.* 1988. Vol.24. No 2. P. 235—238 (In Russ.).
15. *Орданьян С.С.* Взаимодействие в системах LaB_6—$Me^{V}B_2$. *Неорган. материалы*. 1984. Т. 20. No. 11. С. 1821—1824.
Ordan'yan S.S. Interaction in LaB_6—$Me^{V}B_2$ systems. *Neorgan. materialy.* 1984. Vol. 20. No. 11. P. 1821—1824 (In Russ.).
16. *Орданьян С. С., Падерно Ю. Б, Хорошилова И. К., Николаева Е.Е., Максимова Е.В.* Взаимодействие в системе LaB_6—ZrB_2. *Порошк. металлургия*. 1983. No. 11(87). С. 87—90.
Ordan'yan S.S., Paderno Y.B., Khoroshilova I.K., Nikolaeva E.E., Maksimova E.V. Interaction in the LaB_6—ZrB_2 system. *Sov. Powder Metall. Met. Ceram.* 1983. Vol. 22. No. 11. P. 946—948. DOI: 10.1007/BF00805556.
17. *Орданьян С.С., Падерно Ю.Б., Хорошилова И.К., Николаева Е.Е.* Взаимодействие в системе LaB_6—HfB_2. *Порошк. металлургия.* 1984. No. 2 (254). С. 79—81.
Ordan'yan S. S., Paderno Y. B., Khoroshilova I. K., Nikolaeva E.E. Interaction in the LaB_6—HfB_2 system. *Sov. Powder Metall. Met. Ceram.* 1984. P. 23. No. 2. P. 157—159. DOI: 10.1007/BF00792275.
18. *Орданьян С.С., Падерно Ю.Б., Николаева Е.Е., Хорошилова И.К.* Взаимодействие в системе LaB_6—CrB_2. *Порошк. металлургия*. 1984. Т. 257. No. 5. С. 64—66.
Ordan'yan S.S., Paderno Y.B., Nikolaeva E.E., Khoroshilova I.K. Interaction in the LaB_6—CrB_2 system. *Powder*

Metall. Met. Ceram. 1984. Vol. 23. No. 5. P. 387—389. DOI: 10.1007/BF00796605.

19. *Орданьян С.С., Несмелов Д.Д., Вихман С.В.* Взаимодействие в системе LaB_6—W_2B_5. *Неорган. материалы.* 2009. Т. 45. No. 7. С. 1—4.
Ordan'yan S.S., Nesmelov D.D., Vikhman S.V. Phase relations in the LaB_6—W_2B_5 system. *Inorg. Mater.* 2009. Vol. 45. No. 7. P. 754—757. DOI:10.1134/S0020168509070097.
20. *Лобода П.И., Кисла Г.П., Богомол И.И., Сысоев М.А., Карасевская О.П.* Фазовые равновесия в системе LaB_6—MoB_2. *Неорган. материалы*. 2009. Т. 45. No. 3. С. 288—291.
Loboda P.I., Kisla G.P., Bogomol I.I., Sysoev M.A., Karasevskaya O.P. Phase relations in the LaB_6—MoB_2 system. *Inorg. Mater.* 2009. Vol. 45. No. 3. P. 246—249. DOI: 10.1134/S0020168509030042.
21. *Kysla G., Loboda P.* Ceramic materials of the quasi-binary LaB_6—MoB_2 system. *Process. Appl. Ceram*. 2007. Vol. 1. No. 1-2. P. 19—22. DOI: 10.2298/PAC0702019K.
22. *Бешта С.В., Крушинов Е.В., Альмяшев В.И., Витоль С.А., Мезенцева Л.П., Петров Ю.Б., Лопух Д.Б., Хабенский В.Б., Баррачин М., Хеллманн З., Гусаров В.В.* Фазовые соотношения в системе ZrO_2—FeO. *Журн. неорган. химии*. 2006. Т. 51. No. 2. С. 367—374.
Beshta S.V., Krushinov E.V., Al'myashev V.I., Vitol' S.A., Mezentseva L.P., Petrov Yu.B., Lopukh D.B., Khabenskii V.B., Barrachin M., Hellmann S., Gusarov V.V. Phase relations in the ZrO_2—FeO system. *Russ. J. Inorg. Chem*. 2006. Vol. 51. No. 2. P. 325—331. DOI: 10.1134/S0036023606020227.
23. *Несмелов Д.Д., Новоселов Е.С., Вихман С.В.* Кристаллизация эвтектических структур в системе LaB_6—W_2B_5—NbB_2. *Физика и химия стекла*. 2022. Vol. 48. No. 1. P. 34—43. DOI: 10.31857/S0132665122010097.
Nesmelov D.D., Novoselov E.S., Vikhman S.V. Crystallization of eutectic structures in the LaB_6—W_2B_5—NbB_2 system. *Glass Phys. Chem*. 2022. Vol. 1. No.1. P. 23—29. DOI: 10.1134/S1087659622010096.

UDC 621.9.048
DOI dx.doi.org/10.17073/1997-308X-2022-3-63-77

The effect of electrospark deposition using zirconium electrodes on structure and properties of nickel-containing alloy obtained selective laser melting

© 2022 г. **A.E. Kudryashov, Ph.V. Kiryukhantsev-Korneev, S.K. Mukanov, M.I. Petrzhik, E.A. Levashov**

National University of Science and Technology (NUST) «MISIS», Moscow, Russia

Received 14.03.2022, revised 09.06.2022, accepted for publication 15.06.2022

Abstract: Protective coatings were applied by electrospark deposition (ESD) using zirconium electrodes to improve the performance of the Ni-containing alloy obtained using the selective laser melting (SLM) technology. The kinetics of mass transfer was studied in 5 different frequency-energy processing modes. An analog-to-digital converter was used to determine the average number of pulse discharges, single-pulse energy, and the total energy of pulse discharges for 1 min of processing ($\sum E$) for all the modes used. In low-energy processing modes ($\sum E$ = 1459÷2915 J), a weak mass transfer was observed, and the cathode weight gain was recorded only in the first minutes. As the processing time increased, a decrease in the substrate weight was observed. The roughness of coatings (R_a) varied in the range of 3.9–7.2 μm. In high-energy modes ($\sum E$ = 5197÷17212 J), due to intense electrode heating, a steady cathode weight gain was observed, but the formed coatings featured by increased roughness: R_a = 7.4÷8.6 μm. The R_a parameter for the original SLM samples was 10.7 μm. The formed coatings featured by a thickness of 15–30 μm, high continuity (up to 100 %), hardness of 9.0–12.5 GPa, elastic modulus of 122–145 GPa, and friction coefficient of 0.36–0.49. The ESD processing promoted an increase in wear resistance of the SLM alloy by 7.5–20 times, and oxidation resistance by 10–20 % (t = 1150 °C, τ = 30 h). It was found that the coating obtained in the low-energy ESD mode with energy $\sum E$ = 2915 J featured the best performance (hardness, modulus of elasticity, roughness, wear resistance and oxidation resistance).

Keywords: electrospark deposition (ESD), selective laser melting (SLM), heat-resistant alloy, zirconium, hardness, oxidation resistance, wear resistance.

Kudryashov A.E. – Cand. Sci. (Eng.), Leading researcher of the Laboratory «In situ diagnostics of structural transformations», Scientific-Educational Center of SHS, MISIS–ISMAN, NUST «MISIS» (119049, Russia, Moscow, Leninskiy pr., 4).
E-mail: aekudr@yandex.ru.

Kiryukhantsev-Korneev Ph.V. – Cand. Sci. (Eng.), Associate prof., Department of powder metallurgy and functional coatings (PM&FC), NUST «MISIS»; Head of the Laboratory «In situ diagnostics of structural transformations», Scientific-Educational Center of SHS, MISIS–ISMAN.
E-mail: kiruhancev-korneev@yandex.ru.

Mukanov S.K. – Cand. Sci. (Eng.), Research assistant, Laboratory «In situ diagnostics of structural transformations», Scientific-Educational Center of SHS, MISIS–ISMAN. E-mail: sam-mukanov@mail.ru.

Petrzhik M.I. – Dr. Sci. (Eng.), Prof., Department of PM&FC, NUST «MISIS»; Leading researcher, Laboratory «In situ diagnostics of structural transformations», Scientific-Educational Center of SHS, MISIS–ISMAN.
E-mail: petrzhik@shs.misis.ru

Levashov E.A. – Dr. Sci. (Eng.), Prof., Acad. of Russian Academy of Natural Science; Head of the Department of PM&FC, NUST «MISIS»; Head of Scientific-Educational Center of SHS, MISIS–ISMAN.
E-mail: levashov@shs.misis.ru.

For citation: *Kudryashov A.E., Kiryukhantsev-Korneev Ph.V., Mukanov S.K., Petrzhik M.I., Levashov E.A*. The effect of electrospark deposition using zirconium electrodes on structure and properties of nickel-containing alloy obtained selective laser melting. *Izvestiya Vuzov. Poroshkovaya Metallurgiya i Funktsional'nye Pokrytiya (Powder Metallurgy and Functional Coatings)*. 2022. Vol. 16. No. 3. P. 63–77 (In Russ.).
DOI: dx.doi.org/10.17073/1997-308X-2022-3-63-77.

Влияние электроискровой обработки электродами из циркония на структуру и свойства никельсодержащего сплава, полученного селективным лазерным сплавлением

А.Е. Кудряшов, Ф.В. Кирюханцев-Корнеев, С.К. Муканов, М.И. Петржик, Е.А. Левашов

Национальный исследовательский технологический университет (НИТУ) «МИСиС», г. Москва, Россия

Статья поступила в редакцию 14.03.2022 г., доработана 09.06.2022 г., подписана в печать 15.06.2022 г.

Аннотация: Для повышения эксплуатационных свойств Ni-содержащего сплава, полученного по технологии селективного лазерного сплавления (СЛС), наносили защитные покрытия методом электроискрового легирования (ЭИЛ) с использованием электродов из циркония. Кинетику массопереноса изучали на 5 различных частотно-энергетических режимах обработки. С помощью аналого-цифрового преобразователя установлены среднее количество импульсных разрядов, энергия единичных импульсов и суммарная энергия импульсных разрядов за 1 мин обработки ($\sum E$) для всех применяемых режимов. В низкоэнергетических условиях обработки ($\sum E$ = 1459÷2915 Дж) наблюдался слабый массоперенос, привес массы катода фиксировался только в первые минуты. С увеличением времени обработки происходила убыль массы подложки. Шероховатость покрытий (R_a) варьировалась в диапазоне 3,9–7,2 мкм. На высокоэнергетических режимах ($\sum E$ = 5197÷17212 Дж) из-за интенсивного нагрева электродов наблюдался устойчивый привес массы катода, но сформированные покрытия имели повышенную шероховатость: R_a = 7,4÷8,6 мкм. Параметр R_a для исходных СЛС-образцов составлял 10,7 мкм. Сформированные покрытия характеризовались толщиной 15–30 мкм, высокой сплошностью (до 100 %), твердостью 9,0–12,5 ГПа, модулем упругости 122–145 ГПа, коэффициентом трения 0,36–0,49. Проведение ЭИЛ-обработки способствовало росту износостойкости СЛС-сплава в 7,5–20,0 раз, а жаростойкости на 10–20 % (t = 1150 °С, τ = 30 ч). Установлено, что наилучшими свойствами (твердость, модуль упругости, шероховатость износо- и жаростойкость) обладает покрытие, полученное на низкоэнергетическом режиме ЭИЛ с энергией $\sum E$ = 2915 Дж.

Ключевые слова: электроискровое легирование (ЭИЛ), селективное лазерное сплавление (СЛС), жаропрочный сплав, цирконий, твердость, жаростойкость, износостойкость.

Кудряшов А.Е. – канд. техн. наук, вед. науч. сотрудник лаборатории «In situ диагностика структурных превращений», НУЦ СВС, МИСиС–ИСМАН, НИТУ «МИСиС» (119049, г. Москва, Ленинский пр-т, 4, стр. 1).
E-mail: aekudr@yandex.ru.

Кирюханцев-Корнеев Ф.В. – канд. техн. наук, доцент кафедры порошковой металлургии и функциональных покрытий (ПМиФП), НИТУ «МИСиС»; зав. лабораторией «In situ диагностика структурных превращений», НУЦ СВС, МИСиС–ИСМАН.
E-mail: kiruhancev-korneev@yandex.ru.

Муканов С.К. – канд. техн. наук, мл. науч. сотрудник лаборатории «In situ диагностика структурных превращений», НУЦ СВС, МИСиС–ИСМАН. E-mail: sam-mukanov@mail.ru.

Петржик М.И. – докт. техн. наук, профессор кафедры ПМиФП, НИТУ «МИСиС»; вед. науч. сотрудник лаборатории «In situ диагностика структурных превращений», НУЦ СВС, МИСиС–ИСМАН.
E-mail: petrzhik@shs.misis.ru.

Левашов Е.А. – докт. техн. наук, акад. РАЕН, проф., зав. кафедрой ПМиФП, НИТУ «МИСиС»; директор НУЦ СВС, МИСиС–ИСМАН.
E-mail: levashov@shs.misis.ru.

Для цитирования: *Кудряшов А.Е., Кирюханцев-Корнеев Ф.В., Муканов С.К., Петржик М.И., Левашов Е.А.* Влияние электроискровой обработки электродами из циркония на структуру и свойства никельсодержащего сплава, полученного селективным лазерным сплавлением. *Известия вузов. Порошковая металлургия и функциональные покрытия*. 2022. Т. 16. No. 3. С. 63–77.
DOI: dx.doi.org/10.17073/1997-308X-2022-3-63-77.

Introduction

Advanced aerospace engineering requires new materials and technologies. New heat-resistant materials, also nickel-based, are currently under development [1, 2].

The most promising are additive technologies [3] such as selective laser melting (SLM). However, products manufactured by the SLM method are characterized by near-surface structural defects, among them cracks, pores, and non-molten particles are the most dangerous [4].

Applying a protective coating is the most efficient way to extend the service life of heat-resistant alloys [5—8]. Ion plasma deposition [9, 10], gas thermal sputtering [11—13], slip molding [14], and electrospark deposition (ESD) [15—20] are widely used for coating deposition on Ni-containing alloys.

The ESD advantages consist of good adhesion of the coating, relative simplicity of the process and equipment, low energy consumption, sustainability, high-profit margin, and many automation options. High-energy electrospark deposition successfully used to restore worn-out parts.

ESD on the ZhS6U nickel alloy with an electrode made of KhTN-61 alloy (Co—Cr—Nb) improves the oxidation resistance (up to 1000 °C), wear resistance, increases hardness, and reduces the friction coefficient [17]. Electrospark deposition of (Cr—Al—Si—B) electrodes obtained by Self propagated High temperature Synthesis (SHS) on the EP 718-ID (Inconel 718) heat-resistant nickel alloy can also increase the heat and wear resistance [18]. Kudryashov A.E. et al. [19, 20] report the increase of the EP 718-ID alloy oxidation resistance after deposition of SHS electrodes (Mo—Si—B and Zr—Si—B).

Tsyvirko E.I. et al. [21] note an improvement in the physical properties of critical aircraft castings made of nickel alloys when alloyed with 2—3 % Zr. Adding zirconium (0.05—0.25 %) to nickel alloys increases the microhardness of the metal matrix and improves the heat resistance of cast jet engine parts. Adding zirconium and hafnium to nickel alloys increases the oxide layer adhesion to the surface due to lower porosity at the oxide-alloy interface [22].

In view of the above, the investigation of the electrospark deposition of Ni-containing SLM alloy with zirconium electrodes is particular interest. It is expected that ESD will improve oxidation resistance and eliminate surface defects [16].

Multicomponent Zr-containing electrodes are extensively used. For example, CLAB 2 (ZrB_2—$ZrSi_2$—LaB_6) composite with the Ni—Cr—Al binder (30 mol.%) [23] and a $ZrSiO_4$ electrode [24] is used to increase the oxidation resistance of hard metal. In order to improve the wear resistance of the TC11 titanium alloy, the high-entropic CuNiSiTiZr [25] as well as the bulk metallic glass forming the $Zr_{65}Cu_{17,5}Al_{7,5}Ni_{10}$ electrodes [26, 27] were used. Vitreloy 1 ($Zr_{41.2}Ti_{13.8}Ni_{10}Cu_{12.5}Be_{22.5}$) was proposed for welds repairs in worn-out amorphous materials and coatings [28]. To protect the AISI 304 stainless steel against wear, corrosion and tribocorrosion ESD has done in a vacuum with a TaC—ZrC—Mo—Ni electrode [29]. Verkhoturov A.D. et al., Nikolenko S.V. et al. [30, 31] recommend using zirconium only as an electrode binder.

Despite the widespread use of multicomponent Zr-containing electrodes, the application of pure zirconium is limited. In order to improve the quality of Kh12MF steel grade die tooling, we propose the addition of ESD of zirconium first, and then an induction chemical and thermal treatment in a carbon-containing paste [32].

Nikolenko S.V. et al. [33] propose the use of zirconium as an anode material for the treatment of the VT20 titanium alloy, in order to improve its wear and oxidation resistance, or to extend the cutting tool life [34].

This study considers mass transfer, structure, composition, and properties of electrospark deposition of zirconium electrodes on a Ni-containing SLM alloy.

Materials and Methods

The Ni-containing SLM alloy served as a substrate (cathode). Its composition was (wt.%): Ni: 53.75, Al: 24.07, Cr: 13.73, Co: 7.66, Hf: 0.79 [35]. The sample size was 7 mm × 9 mm × 7 mm.

The electrode (anode) was made of zirconium iodide (TU 95 46-97 specifications) with the following composition (wt.%): Zr: base metal, Fe: 0.03, Cu: 0.003, Ni: 0.01, C: 0.008, Si: 0.008, N: 0.005, O: 0.05, Al: 0.005, Cr: 0.002, Hf: 0.01, B: 0.00005, Ti: 0.005. The sample size was 3 mm × 3 mm × 50 mm.

We used an Alier-Metal 303, Alier-Metal 30, and an

Table 1. **Parameters of ESD processing modes**

Таблица 1. Параметры режимов ЭИЛ-обработки

Mode	Alier-Metal machine	Amperage I, A	Pulse duration τ, μs	Pulse frequency f, Hz	N_{avg}	E_{avg}, 10^{-3} J	ΣE, J
1	303	120	20	3 000	66 895	43.57	2915
2	30	170	25	3 000	128 764	133.67	17212
3	30	170	25	1 500	49 829	104.29	5197
4	2002	340	6	15 000	262 803	5.55	1459
5	2002	340	8	10 000	257 270	10.27	2642

Note. The electrode vibration frequency was 600 Hz.

Alier-Metal 2002 (METAL — SCINTI SRL, Russia—Moldova) ESD machines using 5 different frequency and power settings (refer to Table 1).

The surface layer was deposited in an argon environment (99.995 %). After treatment, the electrode and substrate were held in an argon bath until complete cooling.

We used a fast analog to digital converter (ADC) E20-10 (L-Card, Russia) connected to the ESD machine, in order to measure the properties of the pulsed discharges. The raw data was logged by the LGraph 2 software multichannel logger. The recording time was 10 sec. We also used MATLAB configured to handle the ESD process to estimate the energy of a single pulse discharge (E), the number of pulses (N), and the total energy per 1 minute of treatment (ΣE).

We used a KERN 770 (Germany) analytical balance to evaluate the mass transfer kinetics (anode's specific erosion ΔA_i) and cathode specific weight gain (ΔK_i)). The accuracy was 10^{-5} g. We weighed the anode and cathode after each minute of ESD. The total cathode weight gain is [30]

$$\Sigma\Delta K_i = (\Delta K_1 + \Delta K_2 + ... + \Delta K_{10}) / \rho, \quad (1)$$

where ΔK_i is the cathode weight gain in i min of deposition (i = 1, 2...10, g); ρ is the electrode material density, g/cm^3.

The anode total erosion $\Sigma\Delta A_i$ was estimated similarly.

We used a CitoPress-1 mounting press (Struers, Denmark) to embed the samples into conductive resin and make sample sections. A RotoPol-21 polishing machine (Struers) was used to grind and polish the samples. Initially, the samples were polished with various sandpaper grits. We polished the samples with a SiO_2 oxide suspension, 0.05 μm abrasive particle size. The metallographic analysis of the sections was performed with a Neophot-32 optical microscope (Carl Zeiss, Germany). The magnifications for measuring the thickness and continuity of the coatings were 500$^\times$ and 200$^\times$, respectively.

XRD patterns of the electrospark deposition coatings were performed on a DRON 4 diffractometer using monochromatic CuK_α radiation in the step-scanning mode, $2\theta = 10^\circ \div 110^\circ$ angular range (the scanning step was 0.1°, the exposure was 3 to 6 s). The qualitative and quantitative phase analysis procedures are given in [36, 37].

We studied the sample microstructures by scanning electron microscopy (SEM) using an S-3400N microscope (Hitachi, Japan) using a NORAN 7 spectral imaging X-ray microanalysis system (Thermo Fisher Scientific Inc, USA). The sample surface topography and wear tracks were examined using a WYKO NT 1100 optical profiler (VEECO, USA).

The mechanical properties such as hardness (H) and modulus of elasticity (E) were determined by indentation of polished cross sections at the Functional Surfaces Testing Lab, National University of Science and Technology «MISIS», using a Nano-Hardness Tester (CSM Instruments, Switzerland) with a Berkovich diamond tip. We determined H and E according to GOST R 8.748-2011 (ISO 14577) [38]. The Poisson's ratio was assumed to be 0.3. The measurement conditions were as follows: 20 mN max load, 5 s hold time.

The study of tribological properties of samples was carried out on an friction machine Tribometer (CSM Instruments) according to the pin-on-plate scheme with

reciprocating motion. A ball with a diameter of 3 mm made of WC—Co alloy was used as a static partner. Test conditions: track length 4 mm, applied load 1 N, maximum velocity 5 cm/s.

The oxidation resistance of the coatings was evaluated by the sample weight gain after annealing in the air in a SNOL 7.2/1200 electric furnace at 1150 °C, with 30 h total dwell time.

Results and Discussion

Fig. 1 shows the total anode erosion ($\Sigma\Delta A_i$) and total cathode weight gain ($\Sigma\Delta K_i$) depending on ESD time. It was found that $\Sigma\Delta A_i$ increases with processing time for all process modes. The max value ($-73.17\cdot10^{-4}$ cm^3) is reached in High-Energy Mode 2.

The peculiarities of the dependences of the total cathode gain on the time is determined by the processing mode used.

For example, when low-energy modes were used (samples *1*, *4*, *5*), we observed initial cathode weight gain. The initial weight gain period varied from 1 min (mode *4*) to 3 and 4 min in modes *5* and *1*, respectively. As the processing time increases, the substrate loses weight. The min value $\sum\Delta K_i = -5.81\cdot10^{-4}$ cm^3 was found after a 10 min mode *4* deposition.

In high-energy modes *2* and *3*, there is a consistent cathode weight gain. Due to intense electrode heating, burns occur on the surfaces, leading to strong deterioration of the surface finish. Such surfaces would require extra grinding. To avoid burns, the processing time was reduced to 5 min. In modes *2* and *3* $\sum\Delta K_i$ was $59.03\cdot10^{-4}$ and $22.42\cdot10^{-4}$ cm^3, respectively.

For comparison, when using a ZrSiB electrode (composition, wt.%: ZrB_2: 66, $ZrSi_2$: 26, Si: 6, ZrO_2: 2) to treat the EP718 alloy in mode *1*, the following values were observed: $\sum\Delta K_i = 10.01\cdot10^{-4}$ cm^3, and $\sum\Delta A_i = -43.43\cdot10^{-4}$ cm^3 [20]. The mass transfer is intensified since the ESD erosion of refractory substances is an order of magnitude higher than that of metals due to their mostly brittle fracturing [30].

We analyzed the ADC logs which included the single pulse energy (average values over processing time (E_{avg})), the total energy of pulse discharges per 1 min ($\sum E$), and the average number of pulse discharges per 1 min in each mode (N_{avg})) (refer to Table 1).

It was found that in mode *2*, $\sum E$ is at its maximum: 17212 J. In mode *4* with its short, max frequency pulse discharges, the total energy is at its minimum: 1459 J.

Low-energy treatment leads to a low coating formation rate. In high-energy modes, the electrodes are

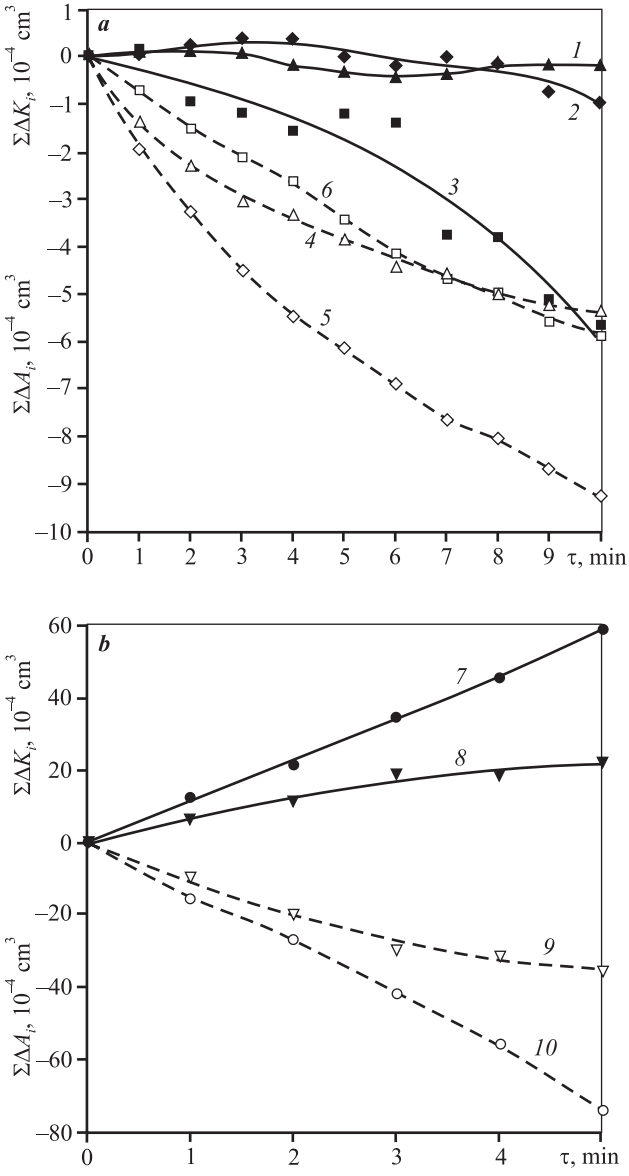

Fig. 1. Total anode erosion $\Sigma\Delta A_i$ (dashed lines, light symbols) and total cathode weight gain $\Sigma\Delta K_i$ (solid lines, dark symbols) depending on ESD time

Curves ***1***, ***4*** – Mode 5 (▲, △); ***2***, ***5*** – Mode 1 (◆, ◇); ***3***, ***6*** – Mode 4 (■, □); *7*, ***10*** – Mode 2 (●, ○); ***8***, ***9*** – Mode 3 (▼, ▽)

Рис. 1. Зависимость суммарной эрозии анода $\Sigma\Delta A_i$ (штриховые линии, светлые значки) и суммарного привеса катода $\Sigma\Delta K_i$ (сплошные линии, темные значки) от времени ЭИЛ

Кривые ***1***, ***4*** – 5-й режим (▲, △); ***2***, ***5*** – 1-й (◆, ◇); ***3***, ***6*** – 4-й (■, □); *7*, ***10*** – 2-й (●, ○); ***8***, ***9*** – 3-й (▼, ▽)

intensively heated. In this case the ESD performance is high, but the surface roughness of the coatings is unsatisfactory.

We found the optimal ESD processing time per 1 cm^2 for the coating application on SLM alloy samples. It is 4 min for the low-energy modes (*1*, *4*, *5*) and 1 min for the high-energy modes (*2*, *3*). This time is sufficient to build solid coatings with an acceptable surface finish. Refer to Table 2 for the R_a (arithmetic average roughness) surface roughness. It is clear that ESD reduces the SLM alloy surface roughness by 1.3—2.8 time. Coating *1* featured the min roughness.

Table 3 lists the phase composition of the coatings. It was found that the SLM alloy contains only the NiAl intermetallic. Coating *1* contains nickel aluminides (NiAl), lattice parameter a = 0.2886 and 0.2922 nm. Its increase may be caused by the introduction of Zr atoms into NiAl during ESD (composition: $Al_{11.45}Ni_{49.83}Zr_{38.72}$). This sample also contains the $ZrNi_2Al$ intermetallic and Zr(OH). Its formation appears to be caused by the interaction between zirconium and dissolved oxygen in the SLM samples. Coating *2* was manufactured with the highest ESD energy possible. It contains NiAl and ZrNi intermetallics, as well as the $Zr_3NiO(x)$ oxide. In addition to sample *1*, the $ZrNi_2Al$ was also found in coatings *3* and *4*. They contain the $ZrCr_2$ phase as well. The $ZrNi_2Al$ triple intermetallic compound is a Heusler phase while the $ZrCr_2$ double intermetallic compound is a Laves phase. The formation of both phases is caused by the interaction between zirconium (anode) and the substrate elements during ESD.

It should be noted that zirconium oxynitride Zr(O, N) with the lattice parameter a = 0.4585 nm corresponds to $Zr_{85.56}N_{3.94}O_{10.5}$ (wt.%). The double oxide $Zr_3NiO(x)$ can be expressed as $Zr_{80.86}Ni_{17.34}O_{1.8}$ (a = 0.329 nm, b = 10.94 nm, c = 8.91 nm).

$ZrCr_2$ melting point is known to be t = 1673 °C [40], and the ZrNi phase melting point is 1260 °C [41]. The formation of such refractory phases should improve the oxidation resistance of the coating.

Fig. 2 shows the SEM images of the ESD coatings *1* and *3*. It can be seen that the surface layer is continuous. It consists of the spread electrode material drops. In the case of high-energy mode *2*, the drop diameter is ~ 450 μm, for high-frequency mode *5*, it is about 170 μm.

Fig. 3, *a* shows an SEM image of coating *5* (polished section). It can be seen that ESD generates a defect-free coating. No cracks at the coating/substrate interface were found.

Electrospark deposition forms a highly continuous (up to 100 %) coating up to 30 μm thick (h) on the surface of an SLM alloy.

Our nano-indentation measurements estimated the mechanical properties of the coatings: E = 122÷145 GPa and H = 9.0÷12.5 GPa (refer to Table 2). The modulus of elasticity of the unhardened sample is higher than that of the electrospark coating and zirconium (96.0—99.0 GPa [42]). The reason is the interaction between Zr and the substrate elements during ESD.

ESD increases the surface hardness by 1.3—1.8 time. Fig. 3, *b* shows the hardness and modulus of elasticity vs. the cross-section width for coating *5*. It can be seen that as the distance to the surface increases, H decreases, and E increases.

When using a ZrSiB electrode to treat the EP718 alloy, the coating has higher hardness (18.8 GPa), modulus of elasticity (351.4 GPa), and roughness (R_a = 5.80 μm) [20]. The max coating hardness of 9.2 GPa was obtained

Table 2. **Properties of the substrate and ESD coatings**

Таблица 2. Свойства подложки и ЭИЛ-покрытий

Sample (mode)	h, μm	R_a, μm	E, GPa	H, GPa
Substrate	–	10.7	162	6.9
1	15	3.9	140	12.3
2	20	8.6	122	9.0
3	30	7.4	145	12.5
4	15	5.0	136	11.1
5	15	7.2	142	10.7

Table 3. **Phase composition of the substrate and ESD coatings**

Таблица 3. Фазовый состав подложки и ЭИЛ-покрытий

Sample (mode)	Phase	Lattice type	Space group	Vol. fraction, %	Mass fraction, %	Lattice constants, nm
Substrate	NiAl	*B*2	*cP*2/1	100	100	$a = 0.2880$
1	NiAl	*B*2	*cP*2/1	45	44	$a = 0.2886$
	NiAl(Zr)	*B*2	*cP*2/1	2	30	$a = 0.2922$
	$ZrNi_2Al$	*D*0.3	*cF*16/2	9	10	$a = 0.6034$
	Zr (O,N)	*B*1	*cF*8/2	14	16	$a = 0.4656$
2	NiAl	*B*2	*cP*2/1	17	15	$a = 0.2877$
	ZrNi	*E*9.3	*cF*96/1	36	37	$a = 1.1985$
	$Zr_3NiO(x)$	*E*1*a*	*oC*20/7	47	48	$a = 3.304$ $b = 11.128$ $c = 8.679$
3	NiAl	*B*2	*cP*2/1	68	64	$a = 0.2881$
	$ZrCr_2$	*C*14	*hP*12/1	13	15	$a = 0.5032$ $c = 0.8328$
	$ZrNi_2Al$	*D*0.3	*cF*16/2	10	11	$a = 0.6023$
	Zr (O,N)	*B*1	*cF*8/2	9	10	$a = 0.4637$
4	NiAl	*B*2	*cP*2/1	51	47	$a = 0.2879$
	$ZrCr_2$	*C*14	*hP*12/1	22	24	$a = 0.5046$ $c = 0.8206$
	$ZrNi_2Al$	*D*0.3	*cF*16/2	13	14	$a = 0.6045$
	Zr (O,N)	*B*1	*cF*8/2	14	15	$a = 0.4646$
5	NiAl	*B*2	*cP*2/1	37	33	$a = 0.2882$
	Zr (O,N)	*B*1	*cF*8/2	38	41	$a = 0.4650$
	$Zr_3NiO(x)$	*E*1*a*	*oC*20/7	25	26	$a = 3.321$ $b = 11.118$ $c = 8.679$

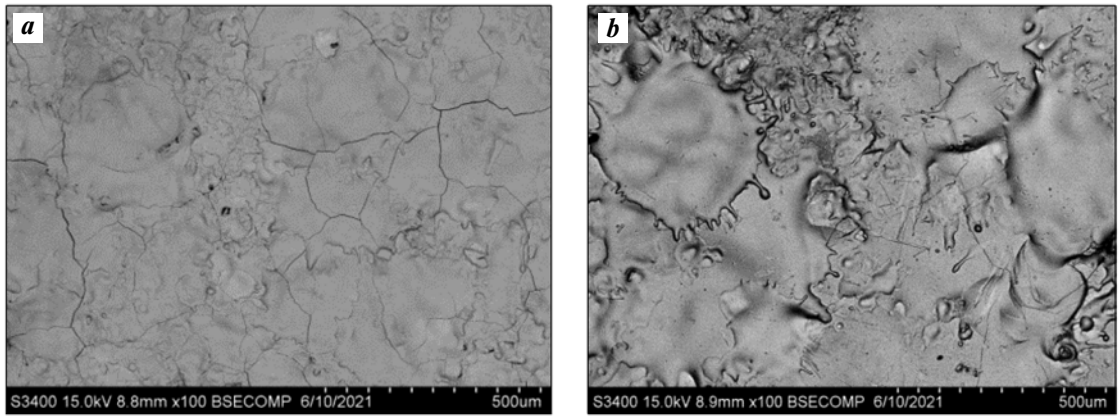

Fig. 2. SEM images of surfaces of ESD coating samples *1* (***a***) and *3* (***b***)

Рис. 2. РЭМ-изображения поверхности образцов ЭИЛ-покрытий *1* (***a***) и *3* (***b***)

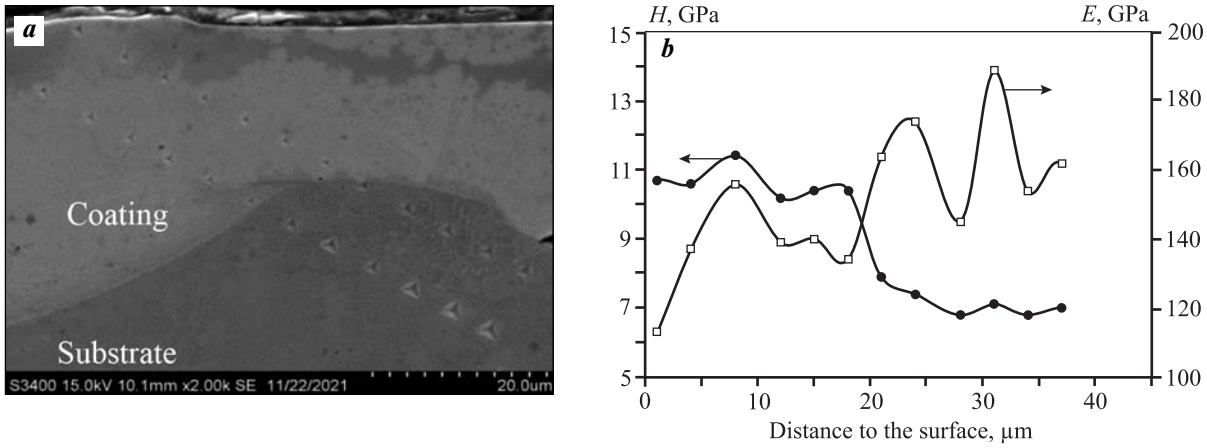

Fig. 3. SEM image of Coating *5* cross-section (***a***) and hardness (*H*) and elastic modulus (*E*) distribution over the coating thickness (***b***)

Рис. 3. РЭМ-изображение поперечного шлифа покрытия *5* (***a***) и распределение твердости (*H*) и модуля упругости (*E*) по его толщине (***b***)

after vacuum treatment of the EP 741 nickel alloy with a NiAl-based alloy electrode [43].

Table 4 lists the tribology test results (friction coefficient (K_{fr}) and reduced wear) for the substrate and ESD coatings. It was found that the unhardened sample has a minimum value of $K_{fr} = 0.34$. ESD increases the friction coefficient: for ESD coatings, $K_{fr} = 0.36 \div 0.49$.

The min friction coefficient of 0.36 was found in sample *4*. Coating *2* was applied in a high-energy mode. At the beginning of testing (up to 5500 cycles) the friction coefficient $K_{fr} \sim 0.33$ was low, and by the end (7000 cycles), it rose to 0.49. Apparently, during the test, the solid wear products on the track surface were able to enter the friction zone thus increasing the friction coefficient [44].

The friction coefficient of the coating formed by the KhTN-61 electrode on the EP718 heat-resistant nickel alloy ($E = 0.3$ J, $f = 1000$ Hz, $\tau = 50$ μs) is $K_{fr} = 0.18$. The value is so low because the surface layer was polished [17].

An unhardened sample of a Ni-containing alloy (Table 4) was found to have the max reduced wear (that is, min wear resistance). Electrospark deposition with a zirconium electrode reduces the reduced wear. Coating *1* showed the best results.

The tribology tests produced cracks on the track surface of the unhardened sample. A possible reason is the shear stresses under load. Samples with coatings *1*, *2*, *3*, and *5* featured partial wear. On these coatings Zirconium was found at the bottom of the tracks. Its content on the sample surface was noticeably higher.

No zirconium was found at the bottom of the wear track in coating *4*, manufactured in the high-frequency mode (15000 Hz), with the min $K_{fr} = 0.36$ and max specific wear rate of $44.4 \cdot 10^{-5}$ mm^3/(N·m). This indicates that the coating is completely worn out.

Fig. 4 shows the oxidation weight index ($\Delta m/S$) as a function of time for the ESD coatings and the unhardened substrate. It was found that oxidation follows the parabolic law, and the oxide layer growth is limited by the oxygen diffusion through it. The maximum coating oxidation rate is observed in the first minutes of the experiment. It reduces after the formation of an oxidized layer on the sample surface.

Fig. 4 shows that coating *3* ($\Delta m/S = 527.62$ g/m^2) and the unhardened sample ($\Delta m/S = 520.68$ g/m^2) have the lowest oxidation resistance, while sample1 showed the best results ($\Delta m/S = 434.90$ g/m^2).

The application of ESD coatings reduces the weight oxidation index by 10—20 %. The oxidation resistance seems to be caused both by the reduction of the SLM alloy surface defects and the formation of a more heat-resistant surface layer.

Table 5 lists the phase composition of the substrate and ESD coatings after long (30 h total time), high-temperature treatment. The following phases were found in the unhardened sample: NiAl (45 %), double oxide $(Al,Cr)_2O_3$ (46 %), traces of HfO_2 (4 %), and $NiCrO_3$ (5 %).

Table 4. **Tribology test results for the substrate and ESD coatings**

Таблица 4. Результаты трибологических испытаний подложки и ЭИЛ-покрытий

Sample (mode)	Reduced wear, 10^{-5} mm^3/(N·m)	K_{fr}			
		Initial	Max.	Avg.	Final
Substrate	142.0	0.02	0.37	0.30	0.34
1	7.0	0.22	0.49	0.44	0.44
2	12.5	0.26	0.50	0.30	0.49
3	18.4	0.65	0.44	0.38	0.41
4	44.4*	0.06	0.45	0.38	0.36
5	14.6	0.11	0.46	0.39	0.42

* The coating is completely gone.

All the coated samples contain NiAl, and the oxides of the substrate elements: $(Al,Cr)_2O_3$, Co_3O_4, $NiCrO_3$ (traces), and zirconium dioxide (ZrO_2), present as two modifications: monoclinic lattice (*C*43), 7 to 28 %, and HCC lattice (*C*1), not more than 2 %.

The presence of $(Al,Cr)_2O_3$ and ZrO_2 oxides in the coatings is desirable. A thin $(Al,Cr)_2O_3/ZrO_2$ coating made by arc ion sputtering on a nickel-based superalloy is known to have high oxidation resistance at t = = 1200 °C, and provides good thermal insulation. At the 1100 °C ambient temperature, the substrate temperature decreased by more than 40 °C [45].

Fig. 5 shows the substrate cross section after long annealing, and an element distribution chart (O, Al, Ni). It can be seen that high-temperature annealing forms a 30 μm thick nickel-free oxidized layer on the substrate surface.

Fig. 6 shows a thin section of coating *4* after annealing and an element distribution chart (O, Zr, Al, Ni) in the oxidized layer. It was found that the surface layer (region *1*) mostly contains zirconium and oxygen, the middle layer (region *2*) contains oxygen, substrate material (Al, Ni, Cr, Co), and electrode (Zr) elements, while the bottom layer (region *3*) contains O, Al, Cr, and small amounts (≤ 1 %) of Ni and Zr. The total thickness of the oxide layers does not exceed 9 μm.

Prolonged high-temperature annealing results in the diffusion of the surface layer elements. The top layer is Zr-containing. The bottom layer bordering the substrate contains aluminum and chromium oxides. The middle layer contains chromium, nickel, and hafnium oxides besides aluminum oxide. For all the coatings the total thickness of oxide layers does not exceed

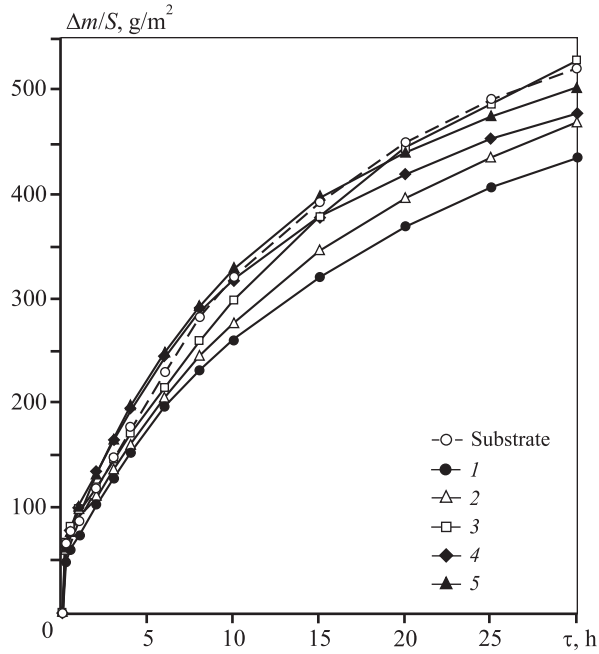

Sample (mode)	Regression equation	Approximation confidence coefficient
Substrate	$\Delta m/S = 97.397\tau^{0,5}$	0.9982
1	$\Delta m/S = 80.920\tau^{0,5}$	0.9992
2	$\Delta m/S = 86.761\tau^{0,5}$	0.9987
3	$\Delta m/S = 95.631\tau^{0,5}$	0.9979
4	$\Delta m/S = 93.648\tau^{0,5}$	0.9968
5	$\Delta m/S = 94.597\tau^{0,5}$	0.9934

Fig. 4. Oxidation weight indicator of the substrate (dashed line) and coatings (solid curves) as a function of time

Curve numbers correspond to the numbers of coating samples (modes)

Рис. 4. Зависимость весового показателя окисления подложки (штриховая линия) и покрытий (сплошные кривые) от времени

Цифры у кривых соответствуют номерам образцов покрытий (режимам)

Table 5. **Phase composition of the substrate and ESD coatings after annealing**

Таблица 5. Фазовый состав подложки и ЭИЛ-покрытий после отжига

Sample (mode)	Phase	Lattice type	Space group	Vol. fraction,%	Mass fraction,%	Lattice constants, nm Lattice angle β, deg
Substrate	NiAl	*B*2	*cP*2/1	39	45	*a* = 0.2873
	HfO_2	*C*43	*mP*12/3	2	4	–
	$(Al,Cr)_2O_3$	*D*5.1	*hR*10/1	54	46	*a* = 0.476 *c* = 1.3025
	$NiCrO_3$	*D*5.1	*hR*10/1	5	5	–
1	ZrO_2	*C*43	*mP*12/3	6	7	–
	Ni Al	*B*2	*cP*2/1	32	35	*a* = 0.2869
	$(Al,Cr)_2O_3$	*D*5.1	*hR*10/1	35	29	*a* = 0.4766 *c* = 1.3016
	$NiCrO_3$	*D*5.1	*hR*10/1	5	5	–
	ZrO_2	*C*1	*cF*12/1	2	2	*a* = 5.136
	Co_3O_4		*cF*56/3	20	22	*a* = 0.8120
2	ZrO_2	*C*43	*mP*12/3	26	28	*a* = 0.5150 *b* = 0.5199 *c* = 0.5327 β = 99.09°
	NiAl	*B*2	*cP*2/1	19	22	*a* = 0.2869
	$(Al,Cr)_2O_3$	*D*5.1	*hR*10/1	39	32	*a* = 0.4771 *c* = 1.3030
	$NiCrO_3$	*D*5.1	*hR*10/1	4	4	–
	ZrO_2	*C*1	*cF*12/1	1	1	*a* = 0.5127
	Co_3O_4		*cF*56/3	11	13	*a* = 0.8120
3	ZrO_2	*C*43	*mP*12/3	12	13	*a* = 0.5155 *b* = 0.5175 *c* = 0.5329 β = 99.10°
	NiAl	*B*2	*cP*2/1	23	26	*a* = 0.2870
	$(Al,Cr)_2O_3$	*D*5.1	*hR*10/1	44	37	*a* = 0.477 *c* = 1.3028
	$NiCrO_3$	*D*5.1	*hR*10/1	4	5	–
	Co_3O_4		*cF*56/3	17	19	*a* = 0.8125
4	ZrO_2	*C*43	*mP*12/3	14	15	*a* = 0.5146 *b* = 0.5188 *c* = 0.5322 β = 99.16°
	Ni Al	*B*2	*cP*2/1	26	28	*a* = 0.2870
	$(Al,Cr)_2O_3$	*D*5.1	*hR*10/1	38	32	*a* = 0.4770 *c* = 1.3023
	$NiCrO_3$	*D*5.1	*hR*10/1	5	5	–
	ZrO_2	*C*1	*cF*12/1	1/1	1	*a* = 0.5132
	Co_3O_4		*cF*56/3	16	19	*a* = 0.8114

Table 5. **Phase composition of the substrate and ESD coatings after annealing (the ending)**

Таблица 5. Фазовый состав подложки и ЭИЛ-покрытий после отжига (окончание)

Sample (mode)	Phase	Lattice type	Space group	Vol. fraction,%	Mass fraction,%	Lattice constants, nm Lattice angle β, deg
5	ZrO_2	*C*43	*mP*12/3	16	17	*a* = 0.5147 *b* = 0.5195 *c* = 0.5331 β = 99.19°
	Ni Al	*B*2	*cP*2/1	27/31	31	*a* = 0.2871
	$(Al,Cr)_2O_3$	*D*5.1	*hR*10/1	40	33	*a* = 0.4772 *c* = 1.3025
	$NiCrO_3$	*D*5.1	*hR*10/1	5	5	–
	ZrO_2	*C*1	*cF*12/1	1	1	*a* = 0.5148
	Co_3O_4		*cF*56/3	11	13	*a* = 0.8126

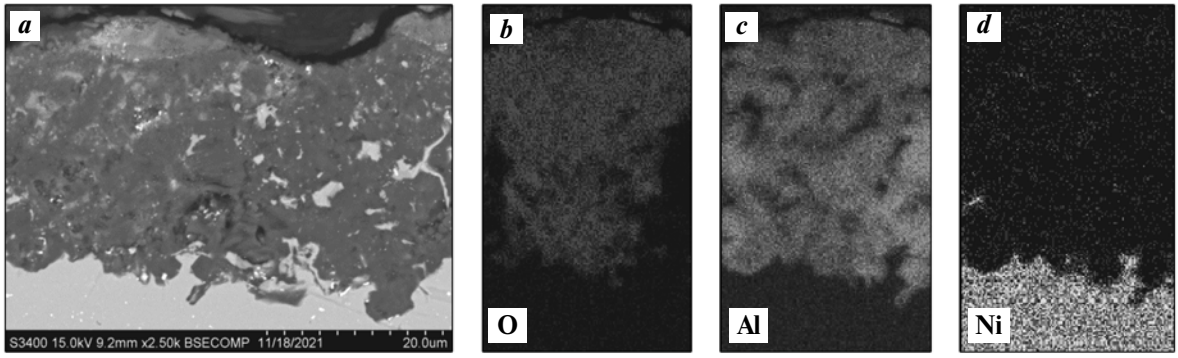

Fig. 5. SEM image of uncoated sample cross-section after annealing (***a***) and map of O (***b***), Al (***c***) and Ni (***d***) distribution in the oxidized layer

Рис. 5. РЭМ-изображение поперечного шлифа образца без покрытия после отжига (***a***) и карта распределения элементов в окисленном слое O (***b***), Al (***c***) и Ni (***d***)

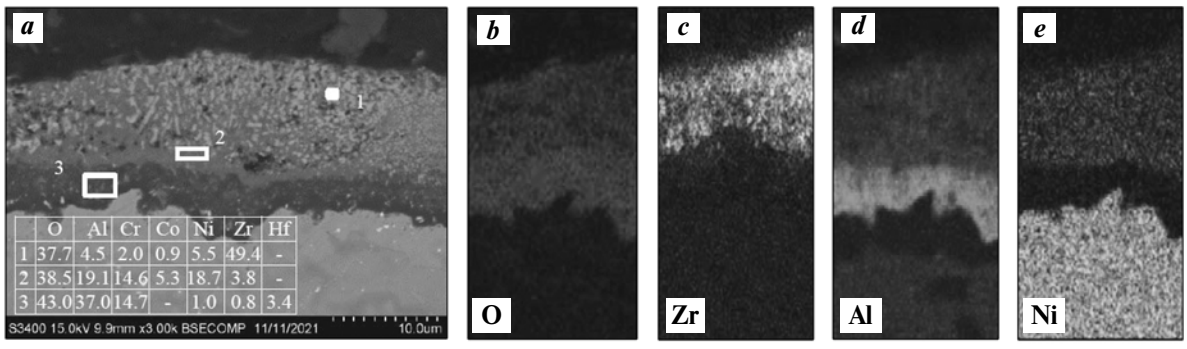

Fig. 6. SEM image of coating *4* cross-section after annealing with indicated EPMA areas (***a***) and map of O (***b***), Zr (***c***), Al (***d***), Ni (***e***) distribution in the oxidized layer

The insert indicates concentrations of elements (wt.%) in the indicated areas

Рис. 6. РЭМ-изображение поперечного шлифа покрытия *4* после отжига с указанием областей МРСА (***a***) и карта распределения элементов в окисленном слое O (***b***), Zr (***c***), Al (***d***), Ni (***e***)

На вставке приведены концентрации элементов (мас.%) в указанных областях

10 μm, which is three times less than for the uncoated sample.

Conclusions

1. We studied the formation of electrospark coatings on Ni-containing SLM alloys with zirconium electrodes. In high-energy modes ($\sum E$ = 5197÷17212 J), consistent cathode weight gain was observed. In low-energy modes ($\sum E$ = 1459÷2915 J) weight gain occurred during the first 1—4 minutes, while cathode weight decreased as the processing time increased.

2. We measured the ESD process variables in each mode: single pulse discharge energy, number of pulses, and total energy of pulsed discharges per 1 min. The coatings 15—30 μm thick with up to 100 % continuity reduce SLM sample surface roughness (R_a) by 1.3—2.8 time.

3. We found the formation of heat-resistant phases with $ZrNi_2Al$, ZrNi, $ZrCr_2$, and oxides ($Zr_3NiO(x)$, Zr(O,N)) in the ESD coatings as a result of interaction between zirconium and the dissolved oxygen present in the SLM samples.

4. The ESD coatings have 9.0—12.5 GPa hardness, and 122—145 GPa modulus of elasticity. Electrospark treatment improves the SLM alloy properties. The hardness is increased by 1.3—1.8 times, wear resistance, by 7.5—20 times, and oxidation resistance, by 10—20 %. In terms of its properties, the best coating was produced in low-energy mode with $\sum E$ = 2915 J.

Acknowledgments: *The research was funded by the Ministry of Science and Higher Education of the Russian Federation as part of the State assignment (Project 0718-2020-0034).*

Работа выполнена при финансовой поддержке Министерства науки и высшего образования РФ в рамках государственного задания (проект 0718-2020-0034).

References

1. *Каблов Е.Н.* Стратегические направления развития материалов и технологий их переработки на период до 2030 года. *Авиационные материалы и технологии.* 2012. No. S. С. 7—17.
   Kablov E.N. Strategical areas of developing materials and their processing technologies for the period up to 2030. *Aviatsionnye materialy i tekhnologii.* 2012. No. S. P. 7—17 (In Russ.).
2. *Логунов А.В., Берсенев А.Г., Логачёва А.И.* Проблемы и перспективы применения металлургии гранул для ракетно-космической техники. *Двигатель.* 2008. No. 2. С. 8—11.
   Logunov A.V., Bersenyev A.G., Logacheva A.I. Problems and prospects of application of metallurgy of pellets for rocket and space technology. *Dvigatel'.* 2008. No. 2. P. 8—11 (In Russ.).
3. *Kaplanskii Yu.Yu., Zaitsev A.A., Levashov E.A., Loginov P.A., Sentyurina Zh.A.* NiAl based alloy produced by HIP and SLM of pre-alloyed spherical powders. Evolution of the structure and mechanical behavior at high temperatures. *Mater. Sci. Eng. A.* 2018. Vol. 717. P. 48—59. DOI: 10.1016/j.msea.2018.01.057.
4. *Carter L.N., Martin Ch., Withers Ph. J., Attallah M.M.* The influence of the laser scan strategy on grain structure and cracking behaviour in SLM powder-bed fabricated nickel superalloy. *J. Alloys Compd.* 2014. Vol. 615. P. 338—347. DOI: 10.1016/j.jallcom.2014.06.172.
5. *Оспенникова О.Г.* Стратегия развития жаропрочных сплавов и сталей специального назначения, защитных и теплозащитных покрытий. *Авиационные материалы и технологии.* 2012. No. S. С. 19—36.
   Ospennikova O.G. Development strategics of high-temperature alloys and special steels, protective and thermoprotective coatings. *Aviatsionnye materialy i tekhnologii.* 2012. No. S. P. 19—36 (In Russ.).
6. *Поклад В.А., Шкретов Ю.П., Абраимов Н.В.* Покрытия для защиты от высокотемпературной газовой коррозии лопаток ротора турбины ГТД. *Двигатель.* 2010. No. 4 (70). С. 2—4.
   Poklad V.A., Shkretov Yu.P., Abraimov N.V. Coatings for protection against high-temperature gas corrosion of turbine turbine rotor blades. *Dvigatel'.* 2010. No. 4 (70). P. 2—4 (In Russ.).
7. *Хокинг М., Васантасри В., Сидки П.* Металлические и керамические покрытия: Получение, свойства и применение. М.: Мир, 2000.
   Khocking M., Vasantasri V., Sidki P. Metallic and ceramic coatings: Production, properties and applications. Moscow: Mir, 2000 (In Russ.).
8. *Подчерняева И.А., Панасюк А. Д., Тепленко М. А., Подольский В.И.* Защитные покрытия на жаропрочных никелевых сплавах (обзор). *Порошковая металлургия.* 2000. No. 9/10. С. 12—27.
   Podchernyaeva I.A., Panasyuk A.D., Teplenko M.A., Podol'skii V.I. Protective coatings on heat-resistant nickel al-

loys (Review). *Powder Metal. Met. Ceram*. 2000. Vol. 39. No. 9-10. P. 434—444.

9. *Матвеев П.В., Будиновский С.А., Мубояджян С.А., Косьмин А.А.* Защитные жаростойкие покрытия для сплавов на основе интерметаллидов никеля. *Авиационные материалы и технологии*. 2013. No. 2 (27). С. 12—15.
   Matveev P.V., Budinovsky S.A., Muboyajyan S.A., Kosmin A.A. Protective heat-resistant coatings for nickel intermetallic alloys. *Aviatsionnye materialy i tekhnologii*. 2013. No. 2 (27). P. 12—15 (In Russ.).
10. *Чубаров Д.А., Будиновский С.А., Смирнов А.А.* Магнетронный способ нанесения керамических слоев теплозащитных покрытий. *Авиационные материалы и технологии*. 2016. No. 4 (45). С. 23—30.
    Chubarov D.A., Budinovsky S.A., Smirnov A.A. Magnetron method of applying ceramic layers of heat-protective coatings. *Aviatsionnye materialy i tekhnologii*. 2016. No. 4 (45). P. 23—30 (In Russ.).
11. *Будиновский С.А., Чубаров Д.А., Матвеев П.В.* Современные способы нанесения теплозащитных покрытий на лопатки газотурбинных двигателей (обзор). *Авиационные материалы и технологии*. 2014. No. S5. С. 38—44.
    Budinovsky S.A., Chubarov D.A., Matveev P.V. Modern methods of applying heat-protective coatings to the blades of gas turbine engines (review). *Aviatsionnye materialy i tekhnologii*. 2014. No. S5. P. 38—44 (In Russ.).
12. *Абраимов Н.В., Елисеев Ю.С., Крымов В.В.* Авиационное материаловедение и технология обработки металлов Учеб. пособие для авиац. вузов. М.: Высш. шк., 1998.
    Abraimov N.V., Eliseev Yu.S., Krymov V.V. Aviation materials science and metal processing technology: Textbook. Moscow: Vysshaya shkola, 1998.
13. *Балдаев Л.Х., Балдаев С.Л., Мазилин И.В., Ахметгареева А.М.* Применение термобарьерных покрытий для лопаток современных газотурбинных установок на примере ГТД-110М. *Надежность и безопасность энергетики*. 2016. No. 2 (33). С. 70—72.
    Baldaev L.H., Baldaev S.L., Mazilin I.V., Akhmetgareeva A.M. Application of thermal barrier coatings for the blades of modern gas turbine units on the example of GTD-110M. *Nadezhnost' i bezopasnost' energetiki*. 2016. No. 2 (33). P. 70—72 (In Russ.).
14. *Денисова В.С., Соловьёва Г. А., Орлова Л.А.* Синтез ресурсных жаростойких эмалевых покрытий на основе стекол барийалюмосиликатной системы для никелевых сплавов. *Успехи в химии и химической технологии*. 2014. Т. 28. No. 8 (157). С. 39—42.
    Denisova V.S., Solovieva G.A., Orlova L.A. Synthesis of resource heat-resistant enamel coatings based on glasses of the barium aluminum silicate system for nickel alloys. *Uspekhi v khimii i khimicheskoy tekhnologii*. 2014. Vol. 28. No. 8 (157). P. 39—42 (In Russ.).
15. *Wang Mao-cai, Wang Wei-fu, Xie Yu-jiang, Zhang Jie.* Electro-spark epitaxial deposition of NiCoCrAlYTa alloy on directionally solidified nickel-based superalloy. *Trans. Nonferrous Met. Soc. China*. 2010. Vol. 20. Issue 5. P. 795—802.
16. *Enrique P. D., Marzbanrad E., Mahmoodkhani Y., Jiao Z., Toyserkani E., Zhou N.* Surface modification of binder-jet additive manufactured Inconel 625 via electrospark deposition. *Surf. Coat. Technol*. 2019. Vol. 362. P. 141—149.
17. *Левашов Е.А. Кудряшов А.Е., Замулаева Е.И., Погожев Ю.С., Санин В.Н., Андреев Д.Е., Юхвид В.И.* Особенности формирования, структура, состав и свойства электроискровых покрытий на никелевом сплаве ЖС6У при использовании сплава ХТН-61 СВС-Ц. *Известия вузов. Порошковая металлургия и функциональные покрытия*. 2009. No. 2. С. 33—38.
    Levashov E.A., Kudryashov A.E., Zamulaeva E.I., Pogozhev Y.S., Andreev D.E., Yukhvid V.I., Sanin V.N. Features of formation and the structure, composition, and properties of electrospark coatings on the ZhS6U nickel alloy with the use of the KhTN-61 SHS-Ts alloy. *Russ. J. Non-ferr. Met*. 2009. Vol. 50. No. 5. P. 534—539.
18. *Kudryashov A.E., Potanin A.Y., Lebedev D.N., Sukhorukova I.V., Shtansky D.V., Levashov E.A.* Structure and properties of Cr—Al—Si—B coatings produced by pulsed electrospark deposition on a nickel alloy. *Surf. Coat. Technol.* 2016. Vol. 285. P. 278—288.
19. *Kudryashov A.E., Lebedev D.N., Potanin A.Y., Levashov E.A.* Structure and properties of coatings produced by pulsed electrospark deposition on nickel alloy using Mo—Si—B electrodes. *Surf. Coat. Technol.* 2018. Vol. 335. P. 104—117.
20. *Kudryashov A.E., Kiryukhantsev-Korneev Ph.V., Petrzhik M.I., Levashov E.A.* Application of Zr—Si—B electrodes for electrospark alloying of Inconel 718 in vacuum, argon and air environment. *CIS Iron Steel Rev.* 2019. Vol. 18. P. 46—51.
21. *Цивирко Э.И., Лысенко Н.А., Клочихин В.Г., Жеманюк П.Д.* Легирование и модифицирование

никелевых сплавов цирконием. *Нові матеріали і технології в металургії та машинобудуванні*. 2007. No. 2. С. 22—29.

Tsyvirko E.I., Lysenko N.A., Klochikhin V.G., Zhemanyuk P.D. Alloying and modification of zirconium nickel alloys. *Novyye materialy i tekhnologii v metallurgii i mashinostroyenii*. 2007. No. 2. P. 22—29 (In Russ.).

22. *Базылева О.А., Аргинбаева Э.Г., Луцкая С.А.* Методы повышения коррозионной стойкости жаропрочных никелевых сплавов (обзор). *Труды ВИАМ*. 2018. No. 4 (64). С. 3—8.

Bazyleva O.A., Arginbaeva E.G., Lutskaya S.A. Ways of increasing corrosion resistance of superalloys (Review). *Trudy VIAM*. 2018. No. 4 (64). P. 3—8 (In Russ.).

23. *Верхотуров А.Д., Гордиенко П.С., Коневцов Л.А., Панин Е.С., Потапова Н.М.* Температурное окисление вольфрамокобальтовых твердых сплавов. *Перспективные материалы*. 2008. No. 2. С. 68—75.

Verkhoturov A.D., Gordiyenko P.S., Konevtsov L.A., Panin E.S., Potapova N.M. Temperature oxidation of tungsten-cobalt hard alloys. *Perspektivnye materialy*. 2008. No. 2. P. 68—75 (In Russ.).

24. *Вострикова Я.А., Верхотуров А.Д., Бурков А.А., Рыбалкин А.А., Коновалова Н.С.* Повышение жаростойкости и износостойкости вольфрамсодержащих твердых сплавов методом ЭИЛ. *Ученые записки Комсомольского-на-Амуре гос. техн. ун-та*. 2017. Т. 1. No. 2 (30). С. 90—99.

Vostrikov Ya.A., Verkhoturov A.D., Burkov A.A., Rybalkin A.A., Konovalova N.S. Increasing the heat resistance and wear resistance of hard tungsten alloys by spark alloying. *Uchenye zapiski Komsomol'skogo-na-Amure gosudarstvennogo tehnicheskogo universiteta*. 2017. Vol. 1. No. 2 (30). P. 90—99 (In Russ.).

25. *Wang X.-R., Wang Z.-Q., He P., Lin T.-S., Shi Y.* Microstructure and wear properties of CuNiSiTiZr high-entropy alloy coatings on TC11 titanium alloy produced by electrospark — computer numerical control deposition process. *Surf. Coat. Technol*. 2015. Vol. 283. P. 156—161. DOI: 10.1016/j.surfcoat.2015.10.013.

26. *Hong X., Tan Y., Zhou C., Xu T., Zhang Z.* Microstructure and tribological properties of Zr-based amorphous-nanocrystalline coatings deposited on the surface oftitanium alloys by Electrospark Deposition. *Appl. Surf. Sci.* 2015. Vol. 356. P. 1244—1251. DOI: 10.1016/j.apsusc.2015.08.233.

27. *Hong X., Tan Y., Wang X., Xu T., Gao L.* Microstructure and wear resistant performance of TiN/Zr-base amorphous-nanocrystalline composite coatings on titanium alloy by electrospark deposition. *Surf. Coat. Technol*. 2016. Vol. 305. P. 67—75. DOI: 10.1016/j.surfcoat.2016.07.077.

28. *Cadney S., Brochu M.* Formation of amorphous $Zr_{41,2}Ti_{13,8}Ni_{10}Cu_{12,5}Be_{22,5}$ coatings via the Electro-Spark Deposition process. *Intermetallics*. 2008. Vol. 16. P. 518—523. DOI: 10.1016/j.intermet.2007.12.013.

29. *Kuptsov K.A., Antonyuk M.N., Bondarev A.V., Sheveyko A.N., Shtansky D.V.* Electrospark deposition of wear and corrosion resistant Ta(Zr)C—(Fe,Mo,Ni) coatings to protect stainless steel from tribocorrosion in seawater. *Wear*. 2021. Vol. 486—487. Art. 204094. DOI: 10.1016/j.wear.2021.204094.

30. *Верхотуров А.Д., Подчерняева И.А., Прядко Л.Ф. Егоров Ф.Ф.* Электродные материалы для электроискрового легирования. М.: Наука, 1988.

Verkhoturov A.D., Podchernyayeva I.A., Pryadko L.F., Eegorov F.F. Electrode materials for electrospark alloying. Moscow: Nauka, 1988 (In Russ.).

31. *Николенко С.В., Верхотуров А.Д.* Новые электродные материалы для электроискрового легирования. Владивосток: Дальнаука, 2005.

Nikolenko S.V., Verkhoturov A.D. New electrode materials for electrospark alloying. Vladivostok: Dalnauka, 2005 (In Russ.).

32. *Федосеев М.Е., Кошуро В.А., Аман А., Фомин А.А.* Структура и твердость стали Х12МФ после электроискрового легирования цирконием и цементации в графитовой пасте. *Вестник Саратовского гос. техн. ун-та*. 2020. No. 2 (85). С. 85—90.

Fedoseev M.E., Koshuro V.A., Aman A., Fomin A.A. Structure and hardness of steel Kh12MF after electric spark alloying with zirconium and cementation in graphite paste. *Vestnik Saratovskogo gosudarstvennogo tekhnicheskogo universiteta*. 2020. No. 2 (85). P. 85—90 (In Russ.).

33. *Николенко С.В., Верхотуров А.Д., Коваленко С.В.* Поверхностная обработка титанового сплава ВТ-20 электроискровым легированием. *Перспективные материалы*. 2002. No. 3. С. 13—19.

Nikolenko S.V., Verkhoturov A.D., Kovalenko S.V. Surface treatment of titanium alloy VT-20 by electrospark alloying. *Perspektivnyye materialy*. 2002. No. 3. P. 13—19 (In Russ.).

34. *Николенко С.В., Ри Х.* Электродные материалы для электроискрового легирования с минеральными и

самофлюсующимися добавками. Хабаровск: ТОГУ, 2015.

Nikolenko S.V., Ri Kh. Electrode materials for electrospark alloying with mineral and self-fluxing additives. Khabarovsk: TOGU, 2015 (In Russ.).

35. *Zaitsev A.A., Sentyurina Zh.A, Levashov E.A., Pogozhev Y.S., Sanin V.N., Loginov P.A., Petrzhik, M.I.* Structure and properties of NiAl—Cr (Co, Hf) alloys prepared by centrifugal SHS casting. Pt. 1. Room temperature investigations. *Mater. Sci. Eng. A*. 2017. Vol. 690. P. 463—472.
36. *Горелик С.С., Скаков Ю.А., Расторгуев Л.Н.* Рентгенографический и электронно-оптический анализ. М.: МИСиС, 1994.

Gorelik S.S., Skakov Yu.A., Rastorguev L.N. Radiographic and electron-optical analysis. Moscow: MISIS, 1994 (In Russ.).
37. *Шелехов Е.В., Свиридова Т.А.* Программы для рентгеновского анализа поликристаллов. МиТОМ. 2000. No. 8. С. 16—19.

Shelekhov E.V., Sviridova T.A. Programs for *X*-ray analysis of polycrystals. *Metal Science Heat Treatment*. 2000. Vol. 42. P. 309—313.
38. *Levashov E.A., Shtansky D.V., Kiryukhantsev-Korneev Ph.V., Petrzhik M.I., Tyurina M.Ya., Sheveyko A.N.* Multifunctional nanostructured coatings: Formation, structure, and the uniformity of measuring their mechanical and tribological properties. *Russ. Metallurgy (Metally)*. Vol. 2010. No. 10. P. 917—935.
39. *Войтович Р.Ф., Пугач Э.А.* Окисление тугоплавких соединений: Справочник. Под ред. Г.В. Самсонова. Киев: Наук. Думка. 1968.

Voitovich R.F., Pugach E.A. Oxidation of refractory compounds: Handbook (Ed. G.V. Samsonov). Kiev: Naukova Dumka. 1968 (In Russ.).
40. Диаграммы состояния двойных металлических систем: Справочник. Под общ. ред. Н.П. Лякишева. Т. 2. М.: Машиностроение, 1997.

Diagrams of the state of double metal systems: Guide (Ed. N.P. Lyakishev). Vol. 2. Moscow: Mashinostroyenie, 1997 (In Russ.).
41. Диаграммы состояния двойных металлических систем: Справочник. Под общ. ред. Н.П. Лякишева. Т. 3. Кн. 1. М.: Машиностроение, 2001.

Diagrams of the state of double metal systems: Guide (Ed. N.P. Lyakishev). Vol. 3. Book 1. Moscow: Mashinostroyenie, 2001 (In Russ.).
42. *Дриц М.Е., Будберг П.Б.* Свойства элементов: Справочник. М.: Металлургия, 1985.

Drits M.E., Budberg P.B. Properties of elements': Guide. Moscow: Metallurgiya, 1985 (In Russ.).
43. *Sheveyko A.N., Kuptsov K.A., Kiryukhantsev-Korneev Ph.V., Kaplansky Yu.Yu., Orekhov A.S., Levashov E.A.* Protective coatings for LPBF Ni-based superalloys using a combination of electrospark deposition and pulsed arc evaporation methods. *Appl. Surf. Sci.* 2022. Vol. 581. Art. 152357. DOI: 10.1016/j.apsusc.2021.152357.
44. *Kiryukhantsev-Korneev Ph.V., Sheveyko A.N., Shvindina N.V., Levashov E.A., Shtansky D.V.* Comparative study of Ti—C—Ni—Al, Ti—C—Ni—Fe, and Ti—C—Ni—Al/Ti—C—Ni—Fe coatings produced by magnetron sputtering, electro-spark deposition, and a combined two-step process. *Ceram. Inter.* 2018. Vol. 44. Iss. 7. P. 7637—7646. https://www.sciencedirect.com/science/article/pii/S0272884218302025.
45. *Xian L., Zhao H., Xian G., Fan H., Xiong J.* Oxidation resistance and thermal insulation performance of thin nano-multilayered $(Al,Cr)_2O_3/ZrO_2$ coating prepared by arc ion plating technique. *Mater. Lett.* 2020. Vol. 281. Art. 128649. DOI: 10.1016/j.matlet.2020.128649.

UDC 621.762
DOI dx.doi.org/10.17073/1997-308X-2022-3-78-87

About the experience of using hardmetals in the production of roller cone bits at Volgaburmash JSC

© 2022 г. **A.A. Zhadyaev**[1,2], **D.A. Zakharov**[2]

[1] Samara State Technical University, Samara, Russia

[2] JSC «Volgaburmash», Samara, Russia

Received 29.03.2022, revised 20.04.2022, accepted for publication 25.04.2022

Abstract: Since 2017, Volgaburmash JSC (Samara, Russia) tested purchased 90%WC–10%Co carbide powder mixtures and finished carbide drill bits from various manufacturers. The work was carried out in order to check the possibility of using purchased products as raw materials at the plant to reduce the production cycle for the manufacture of carbide inserts for roller cone bits. This intercommodity substitution (outsourcing) is carried out with the aim of potential cone bit cost reduction and production process acceleration so that the plant can operate in the heavily competitive environment of foreign and domestic markets. The article focuses on the analysis and detailed comparison of the micro- and macrostructure, physical, mechanical, chemical and processing properties of purchased hard-alloy mixtures and sintered inserts of various manufacturers including Volgaburmash JSC. All properties of materials under study were determined in accordance with the VBM JSC company standard STP 582-17. Much attention is paid to comparing crack resistance or Palmqvist fracture toughness values of the alloy and analysis of microstructure images and fracture propagation pattern after using scanning electron microscopy tests. In addition, consideration is given to such important hard alloy properties as hardness and transverse bending strength. Based on the results of the conducted research, conclusions are presented on the expediency of using purchased hard-alloy materials at the Volgaburmash JSC metallurgical shop in comparison with internally manufactured materials.

Keywords: roller cone bits, tungsten-cobalt granular mixtures, hard alloys, bit inserts, structure, mechanical properties, outsourcing.

Zhadyaev A.A. – Postgraduate student of the Department of metallurgy, powder metallurgy, nanomaterials, Samara State Technical University (443100, Russia, Samara, Molodogvardeyskaya str., 244);
Leading process engineer of JSC «Volgaburmash» (443004, Russia, Samara, Groznenskaya str., 1).
E-mail: alexander-zhadyaev@yandex.ru.

Zakharov D.A. – Cand. Sci. (Eng.), Head of the shop of JSC «Volgaburmash».
E-mail: zaharov.dmi@yandex.ru.

For citation: *Zhadyaev A.A., Zakharov D.A.* About the experience of using hardmetals in the production of roller cone bits at Volgaburmash JSC. *Izvestiya Vuzov. Poroshkovaya Metallurgiya i Funktsional'nye Pokrytiya (Powder Metallurgy and Functional Coatings)*. 2022. Vol. 16. No. 3. P. 78–87 (In Russ.).
DOI: dx.doi.org/10.17073/1997-308X-2022-3-78-87.

Об опыте применения твердых сплавов в производстве буровых шарошечных долот в АО «Волгабурмаш»

А.А. Жадяев[1,2], **Д.А. Захаров**[2]

[1] Самарский государственный технический университет (СамГТУ), г. Самара, Россия

[2] АО «Волгабурмаш», г. Самара, Россия

Статья поступила в редакцию 29.03.2022 г., доработана 20.04.2022 г., подписана в печать 25.04.2022 г.

Аннотация: С 2017 г. на предприятии АО «Волгабурмаш» (г. Самара, Россия) проводились мероприятия по испытанию покупных твердосплавных порошковых смесей состава 90%WC–10%Co и готовых твердосплавных зубков различных

производителей. Работа велась с целью оценки возможности применения покупных изделий в качестве исходных материалов на предприятии для сокращения производственного цикла изготовления твердосплавного вооружения буровых шарошечных долот. Данные работы по товарозамещению (аутсорсингу) проводятся с целью возможного снижения себестоимости шарошечного долота и ускорения процесса его изготовления для функционирования предприятия в условиях острой рыночной конкуренции на внешнем и внутреннем рынках. Статья посвящена анализу и подробному сравнению микро- и макроструктуры, физических, механических, химических и технологических свойств покупных твердосплавных смесей и спеченных зубков различных производителей, в том числе и АО «Волгабурмаш». Определение всех характеристик исследуемых материалов проводилось в соответствии со стандартом предприятия СТП 582-17. Большое внимание уделено сравнению значений трещиностойкости сплавов, или вязкости разрушения по Палмквисту, и анализу снимков микроструктуры и характера распространения трещины после испытаний с использованием сканирующей электронной микроскопии. Также рассмотрены такие важные характеристики сплава, как твердость и предел прочности при поперечном изгибе. На основе результатов проведенных исследований представлены выводы о целесообразности использования в металлургическом цехе АО «Волгабурмаш» покупных твердых сплавов в сравнении с материалами собственного производства.

Ключевые слова: буровые шарошечные долота, вольфрамокобальтовые гранулированные смеси, твердые сплавы, зубки долот, структура, механические свойства, аутсорсинг.

Жадяев А.А. – аспирант кафедры «Металловедение, порошковая металлургия, наноматериалы», СамГТУ (443100, г. Самара, ул. Молодогвардейская, 244); вед. инженер-технолог АО «Волгабурмаш» (443004, г. Самара, ул. Грозненская, 1). E-mail: alexander-zhadyaev@yandex.ru.

Захаров Д.А. – канд. техн. наук, начальник цеха, АО «Волгабурмаш». E-mail: zaharov.dmi@yandex.ru.

Для цитирования: *Жадяев А.А., Захаров Д.А.* Об опыте применения твердых сплавов в производстве буровых шарошечных долот в АО «Волгабурмаш». *Известия вузов. Порошковая металлургия и функциональные покрытия.* 2022. Т. 16. No. 3. С. 78–87. DOI: dx.doi.org/10.17073/1997-308X-2022-3-78-87.

Introduction

Tungsten-cobalt (WC—Co) cemented carbides or sintered hardmetals are extensively used in industry for their high hardness, strength, cracking, and wear resistance [1—4]. The most common applications are cutting tools and dies. Heat-resistant drill bits operating in aggressive environments in the Far North and the Arctic are also made of such materials [5]. Drill rig bit failures due to the rapid wear of the hardmetal inserts are quite common. If the bit is operated within the specified limits, but its hardmetal inserts still fail prematurely, a possible reason is improper hardmetal or defects in its structure [6].

Volgaburmash (Samara) is one of the largest Russian drill bit manufacturers. The company operates a hardmetal metallurgical facility. Their global and domestic rock drilling tools markets are highly competitive. Consumers expect high tool quality and affordable prices.

One strategy aimed at reducing the cost of a roller cone bit and accelerating its manufacturing is the use of commercially available components to simplify the number of manufacturing operations [4, 7]. Sintered hardmetal manufacturing is very complex. It involves a large number (>20) of labor-intensive operations and expensive equipment [8—10].

In this study, we considered the following products and components from various manufacturers.

• Commercially available mixed cobalt/tungsten powders. Products from such powders are made by semi-automatic compression shaping and subsequent vacuum sintering. No in-house powder production is required.

• Sintered hardmetal inserts. The bits are custom-made to customer-provided shapes and dimensions. Using such raw materials significantly accelerates hardmetal product manufacturing and only machining is required. No powder making, compression shaping and vacuum sintering are necessary.

This study is a detailed investigation and comparison of the composition, microstructure, physical, mechanical properties, and manufacturability of commercially available WC—Co hardmetal powders and sintered bit inserts from various manufacturers including Volgaburmash. The applicability of the powders was assessed.

Materials

The following substances were studied.

1. Granulated tungsten-cobalt powders (Table. 1), containing 90 wt.% WC and 10 ± 0.2 wt.%: Co; WC grain size up to 3 μm; paraffin-based binder. Hardmetal powder granules are spherical. They are used for compression shaping of hardmetal drill bit components (inserts, mud gun nozzles, thrust bearings, etc.) The powders were analyzed for compliance with the STP 582-17 company standard, Volgaburmash.

2. Sintered hardmetal inserts from various manufacturers compliant with STP 582-17 (Table 2).

Table 1. **Granular carbide mixtures**

Таблица 1. Гранулированные твердосплавные смеси

Sample No.	Manufacturer
1.1	Volgaburmash, Russia
1.2	Supplier 1, Germany
1.3	Supplier 2, China
1.4	Supplier 3, Russia
1.5	Supplier 4, Russia

Table 2. **Sintered carbide inserts**

Таблица 2. Спеченные твердосплавные зубки

Sample No.	Co, wt.%	Manufacturer
2.1	6	Volgaburmash, Russia
2.2	10	
2.3	15	
2.4	6	Supplier 1, Russia
2.5	10	
2.6	13	
2.7	10 (functional gradient alloy)	Supplier 2, Germany
2.8	10	Supplier 3, China
2.9	6	Supplier 4, Sweden
2.10	10	Supplier 5, Germany

Methods

We used a Jeol JSM 6390A scanning electron microscope (SEM) (JEOL Ltd., Japan) to examine the morphology and estimate the particle sizes and grain-size distribution of the hardmetal powders.

We performed liquid-phase sintering in a vacuum at 1400 ± 30 °C, in order to produce the final structure of the hardmetal samples to be studied [11—13]. We estimated the total (C_{tot}) and free (C_{free}) carbon in the tungsten hardmetals using the gravimetric method according to GOST 25999-83 (ISO 3907:2009) [14]. (The total carbon content in WC—10%Co alloys should be 5.48—5.56 wt.%. It is not rated.)

The density was determined by the hydrostatic method (three samples selected from the batch) according to GOST 20018-74. Coercivity was measured according to ISO 3326:2013 (it decreases as the cobalt content increases, see [15]). The Rockwell hardness of the sintered hardmetal was determined according to GOST 25172-82 (ISO 3878-83) at a 600 N load [16]. The transverse rupture strength was measured according to GOST 20019-74 (ISO 3327:2009). The residual hardmetal porosity was measured using the references from GOST 9391-80 (ISO 4505-1978).

The hardmetal microstructure was investigated using the metallographic method according to ISO 4499:2020 with an Axiotech 100HD-3D optical microscope (Carl Zeiss, Germany), up to 1600×. The samples were pre-treated with Murakami surface etching solution [17]. For all hardmetal grades, no free carbon or η-phase (double tungsten carbide and lacelike or lakelike cobalt inclusions) is allowed. The microstructure deviations were evaluated pursuant to the STP 582-17 company standard.

We paid considerable attention to studying crack resistance as the material's ability to resist crack propagation and, consequently, failure. In the case of WC—Co hardmetals used in drill bit inserts, the fracture toughness is the best metric of crack resistance. This is a structure-sensitive property. Its evaluation helps assess the sensitivity of the material's crack propagation resistance [18, 19]. We applied the Palmqvist toughness test according to ISO 28079:2009, in order to estimate the crack resistance (W_k, $MN \cdot m^{-3/2}$) of the sintered hardmetal.

A Jeol JSM 6390A scanning electron microscope [13,

19] was used for a more detailed study of the sample surface and crack propagation. Our earlier works [20, 21] present the crack resistance analysis for hardmetals and the actual crack resistance values.

The hardness, crack resistance, and microstructure of the samples were studied at 2 mm below the insert surface. It is the average hardmetal wear (for the insert business end) when the insert becomes unusable.

Results and Discussion

The SEM images (Fig. 1) we obtained show the morphology and particle sizes of the granulated hardmetal powders. It can be seen that powders *1.1* and *1.2* have a distinct spherical shape of 50—200 μm granules and are homogeneous. The powder *1.3*, *1.4*, and *1.5* granules were partially destroyed and contaminated with a finer fraction. The reason is the powder grinding through circulation in which the top layers with a higher density destroy the bottom layers. In the case of powder *1.5*, the particle size is not uniform. In order to avoid this, additional operations such as classification and drumming (to make the granules spherical) are required. This could slow down and complicate the powder manufacturing process and increase the costs as there would be some powder loss. Therefore, should Volgaburmash completely cease in-house powder production and switch to third-party supplies, the recovery of powder loss would be impossible, leading to an increase in costs.

Table 3 lists the chemical composition and some manufacturing properties of the granulated hardmetal powders. With regard to the manufacturing properties, samples *1.2*, *1.3*, and *1.4* showed apparent density and fluidity deviations. Subsequently, these led to issues with compression shaping using semi-automatic presses. The reason is the heterogeneity of the powder granules. The paraffin content in powder *1.4* exceeds the threshold. It may cause unpredictable shrinkage during sintering and affect the carbon content.

Fig. 2 shows the structures of the hardmetals sintered from granulated powders *1.1—1.5* (refer to Table 1). The microstructure of the hardmetals generally meets the requirements of the STP 582-17 company standard. However, photo *1.3* shows a segregation area 27 μm in size and two compounding spots (combined area up to 10 μm). Hardmetal *1.5* also features a cluster of crystals

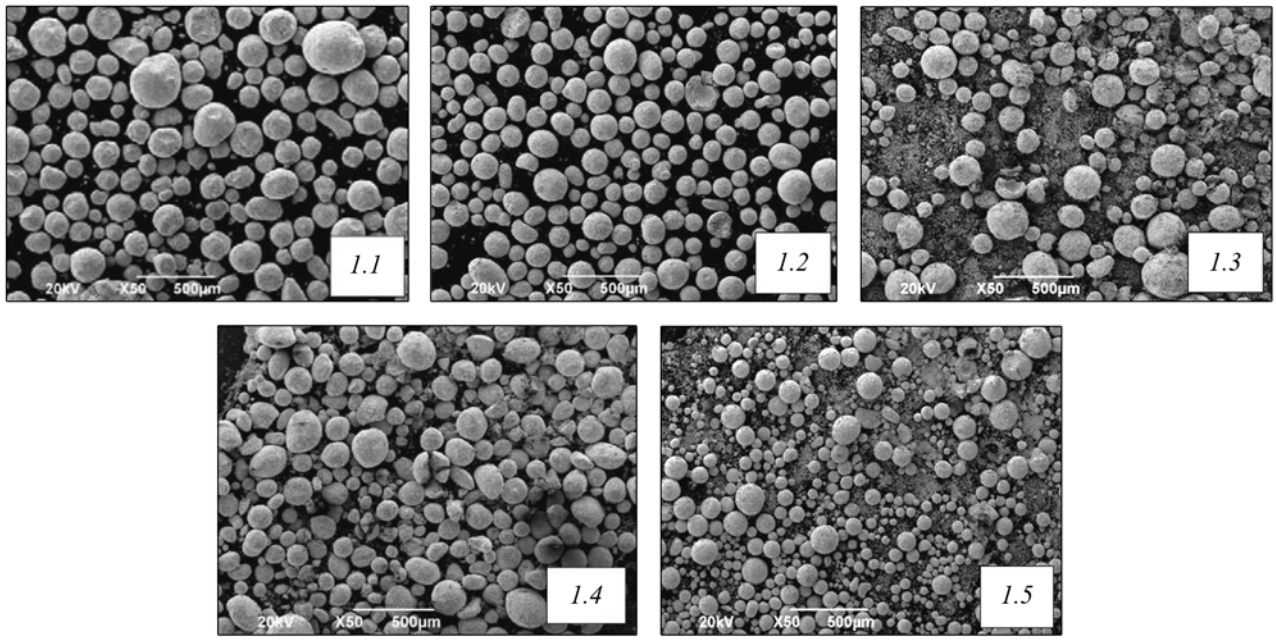

Fig. 1. Micrographs of samples of granulated carbide mixtures *1.1–1.5* (see Table 1)
×50 magnification

Рис. 1. Микрофотографии образцов гранулированных твердосплавных смесей *1.1–1.5* (см. табл. 1)
Увеличение 50×

175 μm in size and a 13 μm compounding area. Note that these deviations are within the tolerances specified in the Volgaburmash company standard.

Table 4 lists the physical and mechanical properties of sintered samples *1.1—1.5*: density (ρ), hardness (*HRA*), coercivity (H_c), transverse rupture strength (σ_{rs}), average grain size (davg), fracture toughness (W_k) and crack length (l).

Next, we compared the structure and properties of the hardmetal inserts produced by different manufacturers (refer to Table 2). Table 5 lists the values for samples containing 10 wt.% Co (refer to Table 2), while Fig. 3 shows their structures.

Sample *2.7* is produced using the manufacturer's proprietary technology. It is a functionally gradient material which indicates different Co content across the

Table 3. **Composition and properties of hard alloy mixtures studied**

Таблица 3. Состав и свойства исследуемых твердосплавных смесей

Sample No.	Content, wt.%				Apparent density, g/cm^3	Fluidity, sec.
	C_{tot}	C_{fixed}	Co	Paraffin		
Rated values	5.48–5.56	≤0.05	10 ± 0.5	2 ± 0.25	3.45 ± 3.65	≤30
1.1	5.56	0.02	9.9	2.25	3.57	28
1.2	5.56	0.03	9.9	1.92	4.07	34.5
1.3	5.59	0.04	10.3	2.06	3.22	35
1.4	5.61	0.02	10.0	2.33	3.49	32
1.5	5.68	0.04	9.9	2.03	3.59	30

Note. The values in bold deviate from the rated ranges.

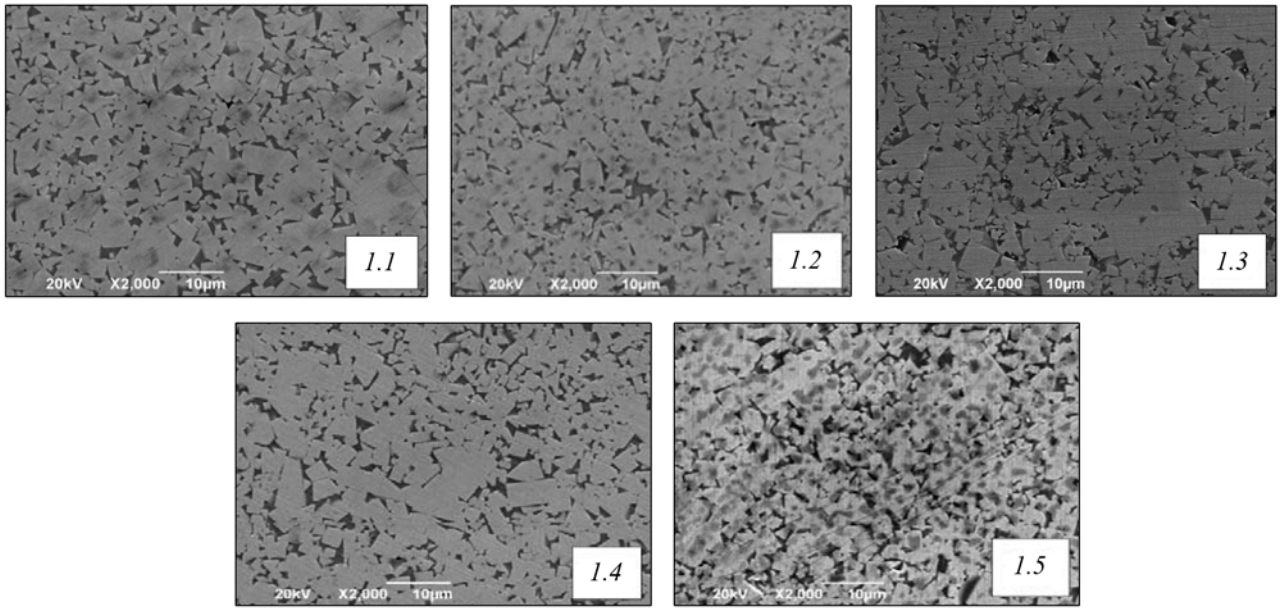

Fig. 2. Structure photographs of alloys sintered from mixtures *1.1–1.5*
×2000 magnification

Рис. 2. Фотографии структуры сплавов, спеченных из смесей *1.1–1.5*
Увеличение – 2000×

Table 4. **Physical and mechanical properties of sintered carbide samples**

Таблица 4. Физико-механические свойства спеченных твердосплавных образцов

Sample No.	ρ, g/cm^3	*HRA*	H_c, Oe	σ_{rs}, N/mm^2	d_{avg}, μm	W_k, MN·m$^{-3/2}$	*l*, μm
Rated values	14.5 ± 0.1	88.2 ± 0.3	75–95	≥2450	2.5–3.0	Actual*	Actual*
1.1	14.53	88.3	83	2960	2.6	17.6	86
1.2	14.51	88.4	87	3150	2.5	17.5	89
1.3	14.47	88.3	97	2670	2.6	15.9	107
1.4	14.51	88.3	79	2900	2.6	16.8	97
1.5	14.53	88.3	83	2960	2.6	17.3	82

* The actual value is for reference only. It is not rated.

Table 5. **Physical and mechanical properties of inserts with 10 wt.% Co content**

Таблица 5. Физические и механические свойства зубков, содержащих 10 мас.% Co

Sample No.	ρ, g/cm^3	*HRA*	H_c, Oe	σ_{rs}, N/mm^2	d_{avg}, μm	W_k, MN·m$^{-3/2}$	l, μm
Rated values	14.53 ± 0.1	88.2 ± 0.3	75–95	≥2450	2.5–3.0	Actual	Actual
2.2	14.53	88.3	83	2960	2.6	17.1	82
2.5	14.53	88.3	84	2900	2.5	17.2	81
2.7	14.55	88.8	90	2950	2.7	16.2	90
2.8	14.56	88.4	91	2910	2.4	17.0	69
2.10	14.53	88.0	87	2850	2.5	16.8	87

Note. The values in bold deviate from the required ranges.

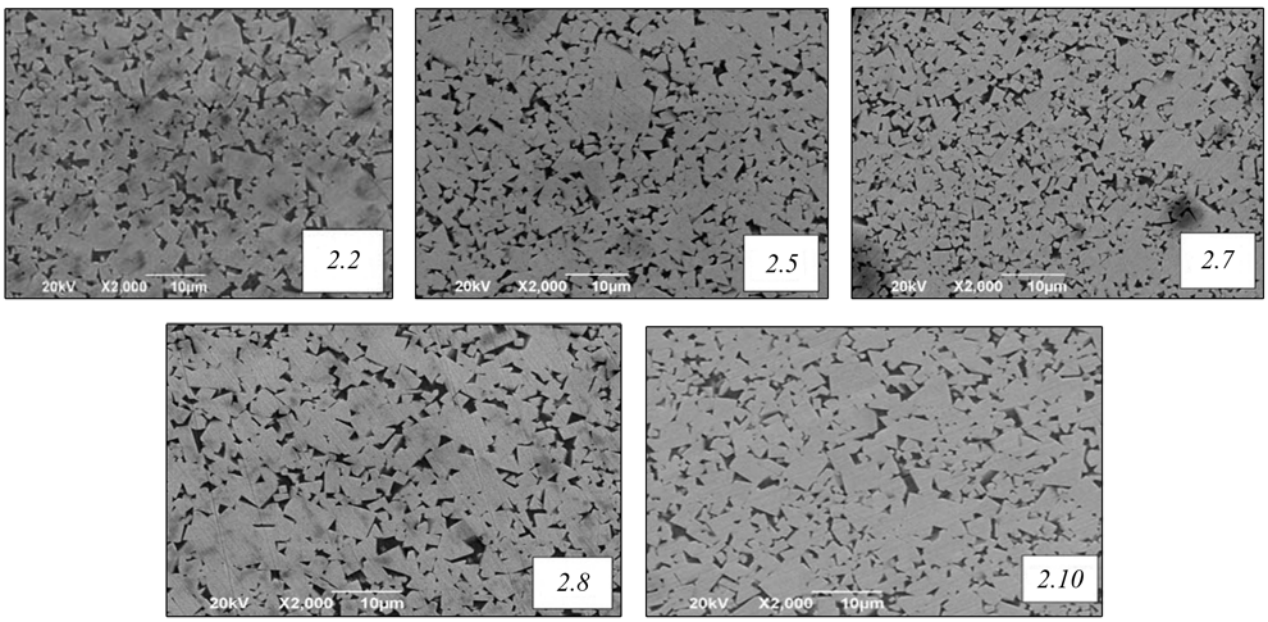

Fig. 3. Structure photographs of inserts with 10 wt.% Co content
×2000 magnification

Рис. 3. Фотографии структуры зубков, содержащих 10 мас. % Co
Увеличение 2000×

Table 6. **Physical and mechanical properties of inserts with 13 and 15 wt.% Co content**
Таблица 6. Физические и механические свойства зубков, содержащих 13 и 15 мас.% Co

Sample No.	ρ, g/cm^3	*HRA*	H_c, Oe	σ_{rs}, N/mm^2	d_{avg}, μm	W_k, MN·m$^{-3/2}$	*l*, μm
Rated values	14.0 ± 0.1	86.5 ± 0.5	70–90	≥2700	2.5–3.5	Actual	Actual
2.3	13.99	87.1	79	3130	2.4	20.3	60
2.6	14.25	86.6	75	2750	2.8	20.5	56

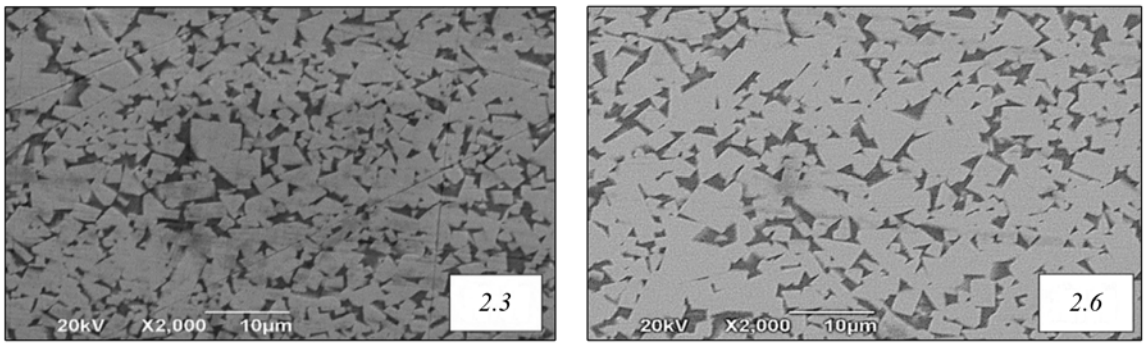

Fig. 4. Structure photographs of inserts with 15 and 13 wt.% Co content
×2000 magnification

Рис. 4. Фотографии структуры зубков, содержащих 15 и 13 мас.% Co
Увеличение 2000×

product. This affects the physical and mechanical properties of the insert.

The analysis showed that the structure is compliant with the company standard. Insert *2.8* has a 57 μm segregation. Samples *2.5* and *2.10* have two compounding sites 11 and 7 μm in size, respectively. Sample *2.2* has a cluster of crystals with a 124 μm total area. Note that all of the above is compliant with the STP company standard.

Table 6 lists the physical and mechanical properties of the hardmetal inserts containing 13 and 15 wt.% Co. Fig. 4 shows the photos of their microstructures. Insert *2.6* has two WC segregation defects with a total area of 51 μm, which is compliant with the company standard.

Table 7 lists the physical and mechanical properties of the hardmetal inserts containing 6 wt.% of Co. Fig. 5 shows their microstructures. Sample *2.1* features two areas of WC crystal aggregation, 103 μm total size. Insert *2.9* has one compounding area 8 μm in size, and three segregation areas 72 μm in size. Such deviations are also compliant with the company standard.

Detailed analysis of the crack showed that the samples mostly have intergranular fractures (at the WC grain boundaries). The cracks propagate along the cobalt binder [22]. Transcrystalline splits in the 10 wt.% Co hardmetal are rare. They usually occur in more ductile alloys with higher cobalt content. In the case of 13 and 15 wt.% Co hardmetals, fractures occur along the WC grains, as can be seen in Fig. 6 (sample *2.3*).

Conclusions

In this study, we compared the structure and properties of the granulated hardmetal powder (refer to Table 1) and sintered hardmetal inserts produced by various manufacturers (refer to Table 2) taking into account the costs and lead time. We arrived at the following conclusions about their possible applications for making hardmetal drill bit inserts by Volgaburmash.

1. Commercially available hardmetal powders *1.2* and *1.5* better match the requirements of the Volgaburmash STP 582-17 standard, but are more expensive, while the average delivery time is about 2 months.

Table 7. **Physical and mechanical properties of inserts with 6 wt.% Co content**
Таблица 7. Физические и механические свойства зубков, содержащих 6 мас.% Co

Sample No.	ρ, g/cm^3	*HRA*	H_c, Oe	σ_{rs}, N/mm^2	d_{avg}, μm	W_k, MN·m$^{-3/2}$	*l*, μm
Rated values	14.95 ± 0.1	90.1 ± 0.5	110–145	≥2300	2.0–2.5	Actual	Actual
2.1	14.91	90.3	132	2420	2.2	13.1	99
2.4	14.86	90.5	107	2670	2.5	13.0	96
2.9	14.98	90.4	130	2750	2.7	12.6	103

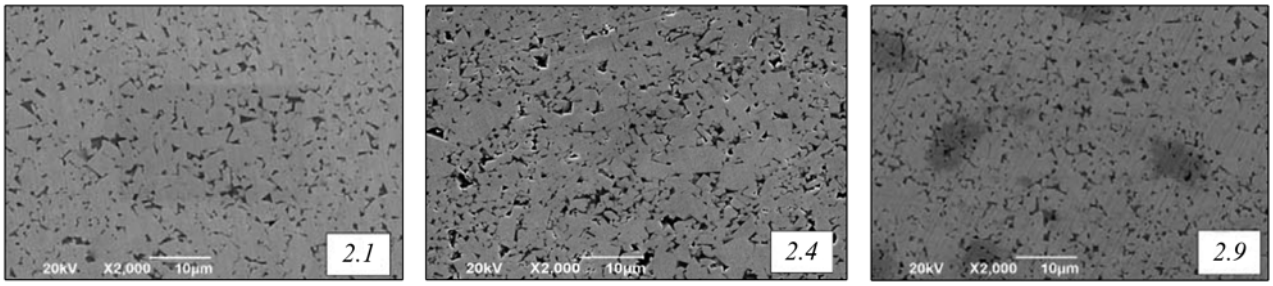

Fig. 5. Structure photographs of inserts with 6 wt.% Co content
× 2000 magnification

Рис. 5. Фотографии структуры зубков, содержащих 6 мас.% Co
Увеличение 2000×

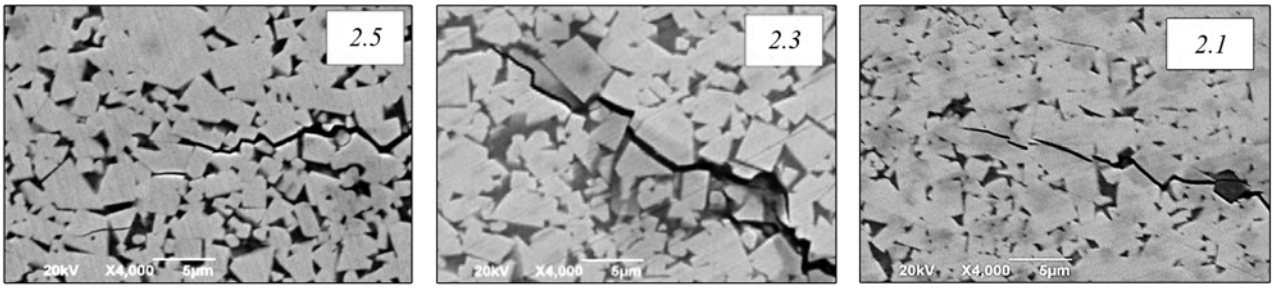

Fig. 6. Fracture propagation in inserts with 10, 15 and 6 wt.% Co content
× 4000 magnification

Рис. 6. Распространение трещины в зубках, содержащих 10, 15 и 6 мас.% Co
Увеличение 4000×

2. The granules of the hardmetal powders *1.3* and *1.4* are partially destroyed by circulation and contaminated with fine fractions. It requires extra effort to refine these powders. They can be used as the primary raw material for hardmetal products provided that the following conditions are met:

— powder refinement operations are introduced;

— refinement leads to powder losses up to 10 wt.%;

— refinement also produces an unusable fine powder fraction;

— the cost of products made from these powders will be higher than from the in-house powder;

— the average delivery time for these powders is 1–2 months;

— if a batch fails the incoming inspection, the entire batch will have to be reprocessed.

3. The physical and mechanical properties of all the samples meet the requirements of the Volgaburmash STP 582-17 company standard. Their characteristics are nearly identical. Still, the crack resistance of sintered

sample 1.3 is lower (W_k = 15.9 MN·m$^{-3/2}$) compared to others (average W_k = 17.4 MN·m$^{-3/2}$) due to the small grain size and higher free carbon content.

4. The physical and mechanical properties of all the hardmetal inserts meet the company standard and can be used for making drill bits.

5. Insert *2.9* containing 6 wt.% Co, has a homogeneous structure and high physical and mechanical properties superior to other samples due to the manufacturing process used.

6. Among the inserts containing 10 wt.% Co, sample *2.7* is functionally gradient with the cobalt content changing from the surface to the core. The hardness of the working end examined (up to 2 mm under the surface) is 89 HRA, which exceeds the required value. This is the reason for the low crack resistance W_k = = 16.1 MN·m$^{-3/2}$. Volgaburmash does not use inserts made of this hardmetal because of their shorter service life compared to the inserts manufactured in-house.

7. Samples *2.4*, *2.5*, and *2.6* meet the requirements in terms of their physical and mechanical properties. They have a homogeneous structure without any critical defects. At present (Q1 2022), inserts produced by this manufacturer are supplied to Volgaburmash. At the customer's request, these inserts are installed on the drill bits (partially or completely).

8. Insert *2.8* has medium hardness (88.4 HRA) and crack resistance (17 MN·m$^{-3/2}$) values, and its structure is homogeneous. Since the service life of these inserts is shorter compared with that of the inserts manufactured by Volgaburmash, further purchases are not recommended.

9. Sample *2.10* meets the STP582-17 company standard in terms of physical and mechanical properties, and structure. The manufacturer supplies two types of such inserts to Volgaburmash at the customer's request.

The disadvantages of the third-party hardmetal inserts are:

— higher bit manufacturing costs;

— the average delivery time for inserts is about 2 months;

— to make a new insert type, the design documentation should be amended, and a new die should be made at extra cost;

— to avoid problems with the press-fit installation of the inserts into the drill body, the lead-in chamfer on the cylindrical part (near the bottom) should be polished to increase the chamfer height. It makes the manufacturing process more complicated;

— it is not possible to deliver more inserts quickly to the customer.

For all these reasons, in-house production of hardmetal inserts is preferable.

References

1. *Okada K., Osada A.* Microstructural study on the grain growth inhibition of VC-doped WC—Co cemented carbides. *Int. J. Refract. Met. Hard Mater.* 2017. No. 62. P. 149—154.
2. *Fang Z.Z., Eso O.O.* Liquid phase sintering of functionally graded WC—Co composites. *Scr. Mater.* 2005. No. 52. P. 785—791.
3. *Furushima R., Katou K., Shimojima K., Hosokawa H., Matsumoto A.* Control of WC grain sizes and mechanical properties in WC—FeAl composite fabricated from vacuum sintering technique. *Int. J. Refract Met. Hard Mater.* 2015. No. 50. P. 16—22. DOI: 10.1016/j.ijrmhm.2014.11.007.
4. *Chang S.H., Chang M.H., Huang K.T.* Study on the sintered characteristics and properties of nanostructured WC—15 wt.% (Fe—Ni—Co) and WC—15 wt.% Co hard metal alloys. *J. Alloys. Compd.* 2015. No. 649. P. 89—95.
5. *Панов В.С., Коняшин И.Ю., Левашов Е.А., Зайцев А.А.* Твердые сплавы: Учебник. 3-е изд., доп. и перераб. М.: Изд. дом НИТУ «МИСиС», 2019.
   Panov V.S., Konyashin I.Yu., Levashov E.A., Zaitsev A.A. Hard alloys: Textbook. Moscow: MISIS, 2019 (In Russ.).
6. *Zhadyaev A., Zakharov D., Amosov A., Novikov V.* Comparative analysis of physical and mechanical properties of hard alloy products depending on the synthesis mode. *AIP Conf. Proc.* 2021. Vol. 2402. P. 020056. DOI: 10.1063/5.0071653.
7. *Guo Z.X., Xiong J., Yang M., Xiong S.J., Chen J.Z., Bi S.Q.* Characterization and properties of MTCVD Ti(C,N) coated cemented carbide substrates with Fe/Ni binder. *Int. J. Refract. Met. Hard Mater.* 2010. No. 28. P. 238—242.
8. *Norgren S., García J., Blomqvist A., Yin L.* Trends in the P/M hard metal industry. *Int. J. Refract. Met. Hard Mater.* 2015. No. 48. P. 31—45.
9. *Daniele Mari, Luis Miguel, Christoph Nebel.* Encyclopedia comprehensive hard materials. Amsterdam: Elsevier, 2015. Vol. 1. P. 29—90.

10. *García J., Strelsky W., Lackner M.* (Eds.). Ch. 9: Process development and scale up of cemented carbide production in scale-up in metallurgy. *Verlag Process. Eng.* 2010. P. 235—265
11. *Ortner H., Kolaska H., Ettmayer P.* The history of the technological progress of hardmetals. *Int. J. Refract. Met. Hard Mater.* 2014. No. 44. P. 148—159.
12. *Zak Fang Z., Wang X., Ryu T., Hwang K.S., Song H.Y.* Synthesis, sintering, and mechanical properties of nanocrystalline cemented tungsten carbide: A review. *Int. J. Refract. Met. Hard Mater.* 2009. No. 27. P. 288—299. DOI: 10.1016/j.ijrmhm.2008.07.011.
13. *González Oliver C.J.R., Álvarez E.A., García J.L.* Kinetics of densification and grain growth in ultrafine WC—Co composites. *Int. J. Refract. Met. Hard Mater.* 2016. No. 59. P. 121—131.
14. *Bolton D., Keely R.J.* Effects of nonstoichiometric carbon contents on the fracture toughness of WC—Co hardmetal alloys. *Int. J. Refract. Met. Hard Mater.* 1982. No. 1 (3). P. 103—111.
15. *Stjernberg K.G.* Some relations between the structure and mechanical properties of WC—TiC—Co alloys. *Powder Metall.* 1970. No. 13 (25). P. 1—12.
16. *Jonsson H.* Studies of the binder phase in WC—Co cemented carbides heat-treated at 950 °C. *Planseeberichte für Pulvermetallurgie.* 1975. Vol. 23 P. 37—55.
17. *Hosokawa H., Shimojima K., Mabuchi M., Kawakami M., Sano S., Terada O.* Effects of the WC grain size on the surface roughness of WC—10%Co cemented carbide micro-die machined by FIB. *Mater. Trans.* 2002. No. 43 (12). P. 3273—3275.
18. *Кушаренко В.М., Репях В.С., Чирков Е.Ю., Кушаренко Е.В.* Дефекты и повреждения деталей и конструкций. Оренбург: ОГУ, 2011.

Kusharenko V.M., Repyakh V.S., Chirkov E.Yu., Kushnarenko E.V. Defects and damage to parts and structures: monograph. Orenburg: OGU, 2011 (In Russ.).

19. *Shing T.L., Luyckx S., Northorp I.T., Wolff I.* The effect of ruthenium additions on the hardness, toughness and grain size of WC—Co. *Int. J. Refract. Met. Hard Mater.* 2001. No. 19 (1). P. 41—44.
20. *Захаров Д.А., Жадяев А.А.* Пути повышения качества твердосплавного вооружения буровых долот. *Металлургия машиностроения*. 2020. No. 5. С. 32—36.

Zakharov D.A., Zhadyaev A.A. Ways to improve the quality of hard-alloy weapons of drilling bits. *Metallurgiya mashinostroeniya*. 2020. No. 5. P. 32—36 (In Russ.).

21. *Жадяев А.А.* Исследование трещиностойкости вольфрамокобальтовых сплавов ВК10С производства АО «Волгабурмаш» и VK10 производства Китай. В сб. *За нами будущее: Взгляд молодых ученых на инновационное развитие общества: Тр. Всероссийской молодежной научной конференции* (05 июня 2020 г.). Курск: Юго-Зап. гос. ун-т, 2020. С. 238—242.

Zhadyaev A.A. Investigation of crack resistance of tungsten-cobalt alloys VK10S produced by «Volgaburmash» JSC and VK10 produced in China. In: *Za nami budushchee: Vzglyad molodykh uchenykh na innovatsionnoe razvitie obshchestva: Trudy Vserossiiskoi molodezhnoi nauchnoi konferentsii* (June 05, 2020). Kursk: Yugo-Zapadnyi Gos. Universitet, 2020. P. 238—242.

22. *Shing T.L., Luyckx S., Northorp I.T., Wolff I.* The effect of ruthenium additions on the hardness, toughness and grain size of WC—Co. *Int. J. Refract. Met. Hard Mater.* 2001. No. 19 (1). P. 41—44.